LUND UNIVERSITY

Charge and proton dynamics in molecules and free clusters from atomic to nanometer scale

Oostenrijk, Bart

2018

Charge and proton dynamics in molecules and free clusters
from atomic to nanometer scale

by Bart Oostenrijk

LUND
UNIVERSITY

DOCTORAL THESIS

by due permission of the Faculty of Science, Lund University, Sweden.
To be defended at the Rydberg Lecture Hall at the Department of Physics,
14 September 2018 at 09:15.

Faculty opponent:
Prof. Nora Berrah
University of Connecticut

Organization
LUND UNIVERSITY

Department of Physics
Box 118
SE–221 00 LUND
Sweden

Author(s)
Bart Oostenrijk

Document name
DOCTORAL DISSERTATION

Date of disputation
2018-9-14

Sponsoring organization

Title and subtitle
Charge and proton dynamics in molecules and free clusters: from atomic to nanometer scale

Abstract
The origin of properties in complex systems can often be traced to mechanisms involving charge and energy transfer in only a few embedded molecules. The detailed study of the time evolution of these mechanisms in their original environment is a challenging task.

In this thesis we develop experimental tools and methods to enable the study of charge and energy transfer. A new ion and electron momentum imaging spectrometer, along with advanced data treatment methods has been succesfully designed, built and tested. The developed spectrometer is optimized for the measurement of the ion and electron momentum correlation that result from the fragmentation of complex systems, from molecules to molecular clusters. We have conducted photodissociation studies on such complex systems, using the newly developed experimental tools. The use of modern X-ray sources allows to localize the initial energy and charge to sites and/or elements in the system, from where the transfer is initiated.

The energy and charge transfer is investigated in molecules by the local (multi-)photon absorption at a controlled site. Among other studies, we investigate the origin of the site-dependence of the fragmentation, be it the population of electronic excited states, conformational isomerization, fast hydrogen evaporation and migration, or secondary breakup. The influence of these processes on the fragmentation are investigated in two ways: through the C1s ionization of chemically distinct carbon sites (ethyl trifluoroacetate), and through the C1s excitation of a model system for conjugated (π) hydrocarbons (1,3 *trans* butadiene).

The migration of charge and transfer of energy in embedded molecular systems is studied by the use of molecular clusters as model systems. The photo-induced energy and charge transport can be facilitated by intermolecular electronic decay, hydrogen migration, proton transfer, the Grotthus mechanism and nuclear rearrangement. The role of these processes in the stabilization and fragmentation of clusters is investigated in clusters of molecules containing N−H and O−H groups that form hydrogen bonds. Among other findings, we conclude that water is an effective stabilizer in multiply-charged hydrated ammonia clusters, which can play an important role in the nucleation process and photochemistry in atmospheric nanoparticles.

Key words
Charge transfer, Electron-Ion coincidence spectroscopy, Molecular photodissociation, site-selective dissociation, Cluster fission, Coulomb explosion, proton hopping

Classification system and/or index terms (if any)

Supplementary bibliographical information

Language
English

ISSN and key title

ISBN
978-91-7753-740-3(print)
978-91-7753-741-0(pdf)

Recipient's notes

Number of pages
234

Price
-

Security classification
-

Signature  Date July 31, 2018

Charge and proton dynamics in molecules and free clusters from atomic to nanometer scale

DOCTORAL THESIS

2018

Bart Oostenrijk
Division of Synchrotron Radiation Research
Department of Physics
Lund University

Front cover illustration:
A disintegrating mosaic of molecules

Lund, July 2018

ISBN: 978-91-7753-740-3 (print)
ISBN: 978-91-7753-741-0 (PDF)

Printed in Sweden by Media-Tryck, Lund University

Abstract

The origin of properties in complex systems can often be traced to mechanisms involving charge and energy transfer in only a few embedded molecules. The detailed study of the time evolution of these mechanisms in their original environment is a challenging task.

In this thesis we develop experimental tools and methods to enable the study of charge and energy transfer. A new ion and electron momentum imaging spectrometer, along with advanced data treatment methods has been succesfully designed, built and tested. The developed spectrometer is optimized for the measurement of the ion and electron momentum correlation that results from the fragmentation of complex systems, from molecules to molecular clusters. We have conducted photodissociation studies on such complex systems, using the newly developed experimental tools. The use of modern X-ray sources allows to localize the initial energy and charge to sites and/or elements in the system, from where the transfer is initiated.

The energy and charge transfer is investigated in molecules by the local (multi-)photon absorption at a controlled site. Among other studies, we investigate the origin of the site-dependence of the fragmentation, be it the population of electronic excited states, conformational isomerization, fast hydrogen evaporation and migration, or secondary breakup. The influence of these processes on the fragmentation are investigated in two ways: through the C1s ionization of chemically distinct carbon sites (ethyl trifluoroacetate), and through the C1s excitation of a model system for conjugated (π) hydrocarbons (1,3 *trans* butadiene).

The migration of charge and transfer of energy in embedded molecular systems is studied by the use of molecular clusters as model systems. The photoinduced energy and charge transport can be facilitated by intermolecular electronic decay, hydrogen migration, proton transfer, the Grotthus mechanism and nuclear rearrangement. The role of these processes in the stabilization and fragmentation of clusters is investigated in clusters of molecules containing N−H and O−H groups that form hydrogen bonds. Among other findings, we conclude that water is an effective stabilizer in multiply-charged hydrated ammonia clusters, which can play an important role in the nucleation process and photochemistry in atmospheric nanoparticles.

Popular science summary

In everyday life, we are all the time affected by processes happening on the molecular level. For instance, the weather forecast relies on models that predict the formation of clouds, a process that starts from two or more molecules sticking together in the atmosphere. Many of these processes only occur on the condition that a few atoms or molecules are held together in a certain way; much in the same way as two wheels and a frame need to be connected in the right places to make a working bicycle. To understand the processes occurring in complex molecules or collections of them, we thus need to study it when it is still intact, rather than in its separate parts.

As of now, we do not have scientific tools to follow the motion of each individual molecule and their electrons in their regular bulk environment. We can, however, extract a molecule together with its immediate neighbors, so that the result of a chemical reaction can be studied as a linked system. This collection of molecules bundled up together is called a molecular cluster. Clusters are often said to bridge the gap between a single molecule (or atom) and the macroscopic bulk liquid or solid.

In this thesis, we aim to make it possible to study complex molecules and clusters, representing simplified versions of everyday life systems. All our experiments start by shining light on clusters. The absorption of light can cause one or more electrons to leave the molecule or cluster. An electron carries a negative charge, and thus leaves the molecule or cluster positively charged, i.e. it has been ionized. Like charges repel, so if the molecular or cluster ion is doubly, or even triply charged, it can break into several pieces that are all singly charged. In molecules, we can remove electrons from a certain place in the molecule, and study the influence of different ionization locations on the types of pieces that are produced from it. In clusters, photoionization creates charges very close to each other, and we can observe which products are formed as a consequence of the charge spreading.

This thesis contributes to the development of research tools by the design of a new measurement instrument (spectrometer) and the development of methods to analyze the data from such instrument. The designed spectrometer can measure both electrons and ions, and specializes in measuring their velocities and the ion's mass.

We have studied a few molecules, for example ethyl trifluoroacetate and butadiene. Ethyl trifluoroacetate is a molecule with a very large difference in the energy required to ionize electrons from different carbon atoms in the molecule. In contrast, butadiene is a molecule with almost no difference in the needed energy to remove an electron from whatever carbon atom. We

show that the ionization of different atoms causes the molecule to break into different pieces and that the bonds around the ionization place are more likely broken in both molecules.

In addition, we have studied molecular clusters that contain ammonia and water molecules. The combination of water and ammonia is important in cloud formation in the atmosphere. We show that the molecular clusters can break up in smaller cluster fragments, or can remain intact, depending on how big they are. Ammonia and water are important in explaining the different aspects of the cluster's behavior: ammonia always carries the charges, and water seems essential in keeping the cluster intact.

Our future research will focus on molecules and clusters that become more and more similar to the ones found in the real world, for example combinations of three or more types of molecules that are thought to be important in the formation of clouds.

Populärvetenskaplig sammanfattning

Många processer i naturen går inte att förklara utan att gå ner på den molekylära skalan och studera enstaka laddningar som elektroner. Till exempel är laddningars rörelse i molekyler en viktig aspekt i fenomen som blixtar och norrsken. Ofta kan dessa processer bara uppstår när sammansättningen av atomer eller molekyler är på ett specifikt sätt; på samma vis som två hjul och en ram behöver sitta ihop korrekt för att vara en funktionsduglig cykel. För att förstå processerna som uppstår i en eller flera komplexa molekyler båda vi alltså studerar det sammansatta systemet, snarare än dess indivuduella komponenter.

Just nu finns det inte så många vetenskapliga metoder som kan följa rörelsen av individuella molekyler i deras naturliga miljö. Vi kan istället studera molekylen och dess direkta omgivning för sig, så att resultatet av en kemisk reaktion där efterliknar den naturliga miljön men är enklare att utreda. En liten samling molekyler som är bundna till varandra kallas ett molekylärt kluster. Man kan se kluster-tillståndet som en brygga mellan den enskilda molekylen (eller atomen) och det makroskopiska objektet.

Forskningen som presenteras i den här avhandlingen handlar om att göra det möjligt att studera komplexa molekyler och kluster, som representerar förenklade versioner av system som man hittar i naturen. Vi studerar laddningars rörelse på en mikroskopisk skala, i en molekyl eller i kluster av molekyler. I våra experiment använder vi röntgenstrålar, vilket är ljus med hög energi, för att separera två eller flera elektroner från en molekyl. Då skapas två eller flera närliggande positiva laddningar i molekylen, som då kallas en molekylär jon. Eftersom lika laddningar utövar en repulsiv kraft på varandra så skjuts laddningarna ifrån varandra, vilket ofta leder till att hela molekylen sönderfaller. Vi vill studera hur sönderfallet av molekyler påverkas av i vilken atom som de positiva laddningar skapas; Om det alltid sker där eller om molekylen har tid att omdistribuera laddningarna och sönderfalla på samma sätt oberoende av initialpositionen.

Vi har vidareutvecklat metoder för att studera egenskaperna hos dessa elektroner och joner. Ett nytt instrument har byggts, som kan mäta elektroners hastiget samt joners vikt och hastighet. Vi har även utvecklat metoder för dataanalys. I vår mätmetod kan vi välja från vilken atom i molekylen vi tar bort elektroner, och observera hur detta påverkar sönderfallet. Två olika typer av molekyler har studerats; ethyl trifluoroacetat och butadien. Sönderfallet sker på olika sätt i de två molekylerna; I ethyl trifluoracetat är sönderfallet nästan detsamma oavsett från vilken atom elektroner försvinner, även om den kemiska sammansättningen i molekylen varierar. Sönderfallet

sker också i flera steg. Däremot har vi observerat att i butadien, vars kemiska sammansättning inte varierar så mycket, spelar det stor roll från vilken atom elektronen kommer. Vi ser också att molekylen omfördelar sina atomer i hög grad innan sönderfallen.

Vi har också studerat molekylära kluster av ammoniak och vatten som är en viktig blandning i atmosfären. I ett experiment tar vi bort två eller flera elektroner från ett kluster, och skapar laddningar på en eller fler närliggande molekyler. Då kan vi till exempel se att laddningen ibland hoppar från en molekyl till en annan och att det alltid är till en ammoniakmolekyl. Ibland observerar vi att klustrena klarar av att hålla två laddningar utan att sönderfalla, om de är tillräckligt stora. Vi observerar att en ökad andel vatten kan hjälpa till att hålla ett mindre kluster intakt, därför kan vi dra slutsatsen att vatten är viktigt för att hålla ihop dessa kluster.

Vår framtida forskning kommer att fokusera på kluster som innehåller fler typer av molekyler och efterliknar nanopartiklar som finns i atmosfären. Vi hoppas kunna särskilja de olika molekylernas roll i sönderfallen.

Samenvatting in Jip-en-Janneketaal

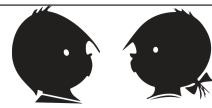

Om de onderliggende werking van veel alledaagse dingen uit te kunnen leggen, moeten we ze bekijken op erg kleine schaal. Bijvoorbeeld, om deze tekst te kunnen lezen, sturen vele zenuwcellen signalen over en weer in je hersenen, waar vele moleculen[1] samenwerken om de informatie te kunnen verwerken. Of bijvoorbeeld in de atmosfeer, waar moleculen zich met elkaar verbinden en tot waterdruppeltjes groeien, die uiteindelijk wolken vormen. Het is moeilijk om zulke processen in werking te bestuderen: ze zijn te klein om met een gewone microskoop te zien.

Er zijn daarom manieren bedacht om steeds kleinere deeltjes te kunnen bestuderen: de eigenschappen van moleculen en atomen kunnen vandaag de dag met grote nauwkeurigheid gemeten worden. Het is echter niet mogelijk om het gedrag van een ingewikkeld molecuul, of een aantal nabije moleculen (kluster), te voorspellen door alle atomen individueel te bestuderen: het geheel kan zich heel anders gedragen dan je van ieder onderdeel apart kon voorspellen. Er zijn een hoop processen in complexe moleculen of klusters waar we wel meer over zouden willen weten, maar waar we nog niet de meetmethoden voor hebben.

Onze aanpak is de volgende: we gebruiken de methoden die gebruikt worden om atomen en simpele moleculen te bestuderen, en breiden die uit, zodat ze beter geschikt worden om toegepast te worden in het onderzoeken van complexe moleculen en kluster. De experimenten beschreven in dit proefschrift beginnen altijd hetzelfde: een deeltje (molecuul of kluster) absorbeert licht dat veel energie bevat. Dit leidt er vaak toe dat het deeltje een elektron uitzendt. Dit gebrek aan één of meerdere elektrons geeft het deeltje een lading. In dit proefschift onderzoeken we hoe de energie en lading in het deeltje beweegt, en hoe het in veel gevallen leidt tot het breken van het deeltje.

De deeltjes die we hier bestuderen zijn moleculen en klusters. We bestuderen onder andere de moleculen ethyl trifluoroacetaat en butadieen. Deze moleculen zijn vooral verschillend in hun chemische eigenschappen: ethyl trifluoroacetaat bestaat uit een keten van koolstof en zuurstof atomen, met aan één kant veel atomen die elektronen veel sterker aantrekt dan aan de andere kant. Butadieen bestaat uit een koolstofketen, met identieke uiteinden. De meetmethoden stellen ons in staat om te kiezen welke koolstof atoom het lichtdeeltje zal absorberen, en vervolgens te bekijken wat het gevolg is voor de beweging van energie en lading. We laten zien hoe de beide moleculen in

[1] Een molecuul is een samenstelling van twee of meer atomen die met elkaar verbonden zijn met behulp van elektronen.

stukken breken: trifluoroacetaat breekt in stapjes, en de (waterstof) atomen in butadieen bewegen erg veel voordat het molecuul breekt. We laten ook zien dat de verschillende eigenschappen van de uiteinden van de koolstofketen voor een klein verschil in de stroming van energie en lading zorgt.

We hebben ook klusters bestudeerd die zijn opgebouwd uit een combinatie van ammoniak en water moleculen, belangrijk in het vormen van wolken in de atmosfeer. We laten zien dat ammoniak altijd de lading draagt, en dat het graag andere ammoniak moleculen om de lading verzamelt. Water is belangrijk in het heel houden van de kluster; meer water moleculen in de kluster zorgt ervoor dat de kluster minder moleculen nodig heeft om intact te blijven en dus eerder stabiliseert.

In de toekomst zullen we op zoek gaan naar manieren om nog complexere of grotere deeltjes te bekijken, die bijvoorbeeld belangrijk zijn in biologische cellen, met de meetmethoden die we hier hebben ontwikkeld.

List of papers

This thesis is based on the following publications and manuscripts, which will be referred to by their Roman numerals.

Paper I:
Chemical Understanding of the Limited Site-Specificity in Molecular Inner-Shell Photofragmentation

L. Inhester, B. Oostenrijk, M. Patanen, E. Kokkonen, S.H. Southworth, C. Bostedt, O. Travnikova, T. Marchenko, S. Son, R. Santra, M. Simon, L. Young and S.L. Sorensen
Physical Chemistry Letters, **9**, 1156 (2018) DOI: 10.1021/acs.jpclett.7b03235

I took part in the experiments, performed the experimental data analysis by writing the data treatment software, and I took part in writing the paper.

Paper II:
Site-selective dissociation upon core-electronic excitation in butadiene

S. Oghbaiee, M. Gisselbrecht, N. Walsh, B. Oostenrijk, J. Laksman, E.P. Månsson, A. Sankari, J.H.D Eland and S.L. Sorensen
Submitted

I took part in preparing and performing the experiments.

Paper III:
Ultrafast dynamics of methyl iodide studied with XUV Free Electron Laser

Y.C. Cheng, B. Oostenrijk, J. Lahl, S. Maclot, S. Augustin, G. Schmid, K. Schnorr, S. Meister, D. Rompotis, B. Manschwetus, C. Bomme, B. Erk, D. Rolles, R. Boll, P. Olshin, A. Rudenko, M. Meyer, P. Johnsson, R. Moshammer and M. Gisselbrecht
In manuscript

I took part in preparing and performing the experiments, and writing the paper.

Paper IV:
Photofragmentation of gas-phase acetic acid and acetamide clusters in the vacuum ultraviolet region

M. Berholts, H. Myllynen, K. Kooser, E. Itälä, S. Granroth, H. Levola, J. Laksman, S. Oghbaiee, B. Oostenrijk, E. Nõmmiste and E. Kukk
Journal of Chemical Physics, **147**, 194302 (2017) https://doi.org/10.1063/1.4999686

I took part in preparing and performing experiments.

Paper V:
The role of charge and proton transfer in fragmentation of hydrogen-bonded nanosystems: the breakup of ammonia clusters upon single photon multi-ionization

B. Oostenrijk, N. Walsh, J. Laksman, E.P. Månsson, C. Grunewald, S.L. Sorensen and M. Gisselbrecht
Physical Chemistry Chemical Physics, **20**, 932 (2018) DOI: 10.1039/c7cp06688k

I wrote software for the data analysis, and was the main responsible for writing the paper.

Paper VI:
Stability and breakup of charged nano-hydrated ammonia clusters - a step towards a microscopic understanding of the nucleation process?

B. Oostenrijk, N. Walsh, A. Sankari, E.P. Månsson, S. Maclot, S.L. Sorensen and M. Gisselbrecht
In manuscript

I wrote software for the data analysis, and was the main responsible for writing the paper.

Paper VII:
A Versatile Velocity Map Ion-Electron Covariance Imaging Spectrometer for High-Intensity XUV Experiments

L. Rading, J. Lahl, S. Maclot, F. Campi, H. Coudert-Alteirac, B. Oostenrijk, J. Peschel, H. Wikmark, P. Rudawski, M. Gisselbrecht and P. Johnsson
Applied Sciences, **8**, 998 (2018) DOI:10.3390/app8060998

I took part in preparing and performing the experiments.

Acknowledgements

Many people have contributed to the making of this thesis, and here I would like to thank all of them, and apologize in advance for leaving out anyone.

First of all, a big thank you to Mathieu Gisselbrecht, my main supervisor, collaborator, lunch buddy and inspirator. Your informal and positive attitude has stimulated me to develop in many ways, and has been very important in the transition of me from engineer to scientific engineer. I am also happy to do something in return by correcting the occasional 'Franglais'. It has been very pleasant working together, and discussing anything from mankind and its fundamental flaws to the best lawn mowers on the current market.

Thanks also to my co-supervisor, Stacey Sorensen, for the scientific discussions, the setting up of collaborations with people from around the world, but also for the ice skating and lundaloppet. It was fun to talk about anything from crazy outdoor stories (e.g. featuring hungry bears) to Bukowski and Vonnegut. Despite your busy schedule, you always found time to talk and discuss, and help me in moving forward.

Many thanks to my colleagues in the research group, Noelle Walsh in particular for helping me out in the lab during the long days before and during beamtime. Things would have not worked out without your support, and you are still of great help through your work at MAX-IV now. Thanks also to Erik Månsson, Anna Sankari, Shabnam Oghbaie, Mohamd Hudieb, Benjamin Bolling and Rebecka Lindblad; it was nice and fun working together.

I have had the privilige to get to know and collaborate with many people. Thanks to the collaborators from Turku University, who made me aware of the power of electron-ion coincidence measurements, and show me how MAX-lab's coffee room TV can show more fun things than just the beam current. It was also a great pleasure to collaborate with the Heidelberg people: Severin, Georg and Sven with their 'soepele banden', the people at the FLASH beamline in Hamburg, and Lund's atomic physics division; Per, Linnea, Jan, Hampus and Sylvain. In particular, Yu-Chen for working together in the lab and on the manuscript, and the interesting conversations about the PhD (after-)life. I thank everyone committed to the joint effort in the study of the 'ESCA' molecule. At SOLEIL, it was great to meet and work with so many nice people: Minna and Esko; Linda, Stephen and Christoph; Oksana, Tatiana and Marc. It was very nice and educational to work with "the theoreticians" in Hamburg; Ludger, Sang-Kil and Robin, whose help completed the project to a nice scientific work.

There are many people at MAX-IV that have helped me many times: Maxim Tchaplyguine, Gunnar Öhrwall and Mikko-Heikki Mikkelä. In par-

ticular, Antti Kivimäki for the thorough revision ("granskning") of the thesis. I would also want to thank the often underappreciated enablers: The technicians at Fysikum (Håkan) and Max Lab (Lars Christiansson, Magnus Berglund, Anders Månsson, Mikke Johansson, Nils Sundqvist and Robert Andersson), who told me to "take all you can carry" when I was again out hunting for nuts and bolts during beamtime.

On that same note, the enablers behind many open access projects such as Wikipedia, Ubuntu, Inkscape, LateX, FreeCAD, GIMP, Thunderbird, Python, POVray, etc, all deserve to be thanked for the fantastic digital tools they provide to the public, often on a voluntary basis, which make the work a lot easier and faster.

Thanks to everyone at the division, during the boardgame afternoons, Kick offs, badminton, kubb, BBQ, julbord and the countless opportunities to eat cake. Sanna and David, thank you in particular for first of all trying to understand, and then correcting my swedish writing, and most importantly for keeping me updated with the latest vocabulary additions (such as 'fulf').

I guess physicists are not known for their organizational and administrative skills, which explains why we have such qualified economists at the division: Anne and Patrik, thanks for helping me in the administrative tasks in all the electronic systems I still don't really understand (but I will remember 111211).

I would also like to thank everyone involved in making the Bike Kitchen Lund real. There are probably too many to not forget someone, but here is a try: Vera, Rosa, Erik, Phil, Gerard, Lars, Graham, Marius, René, Thomas, Simon, Stephanie, Jonathan, Gunnar, Lucy, Kilian, Marie-Laure, Andreas, Dmytro, Verena, Gavin, William, Sandro, Paul, David, Nils, Clemens, Valentin, Sarah, Joost, Marija, Sophie, Cem, Alex, Arnaud, and all the others. I am very proud to be part of the community, and hope it will keep on going for many years to come!

Mama, dankjewel dat je er altijd voor mij bent, ondanks dat ik de laatste jaren maar weinig tijd had om naar huis te komen. Robert en Paul worden hartelijk gefeliciteerd met de titel "broeders zonder grenzen", een indrukwekkende prestatie zonder medische achtergrond. Linda, je bent mijn allerliefste zus, ik ben ontzettend trots op wat jij in de afgelopen jaren hebt bereikt, veel indrukwekkender dan een pietluttig boekje. Kas, we hebben veel tijd in te halen, maar er ligt een mooie toekomst vol fiets(bouw)avonturen voor ons! And Ina, I am very happy we can help each other to get through the last miles together. You help me look at things from a different perspective, and you have been a great support and inspirator to me!

Contents

Chapter 1

Introduction

Our understanding of fundamental and (ultra-)fast energy and charge transfer processes occurring at the molecular level has developed considerably during the past decades. The study of matter with light allows us to monitor chemical reactions in real-time (e.g [1]) with resolution down to a few femtoseconds (10^{-15} s). Similarly, the ultrafast dynamics induced by photoexcitation or photoionization of a specific atom in a molecule or solid (e.g [2]) can be studied. In comparison, the investigation of elementary processes in macroscopic systems remains very challenging. Recently, many experimental techniques have developed, that each provide another perspective on either the electronic or structural properties, often using pump-probe methods [3–6]. The spectroscopic techniques span almost over the entire electromagnetic spectrum, from the low-energy photons, such as time-resolved terahertz spectroscopy [7] and infrared vibrational spectroscopy [8], to the visible spectrum such as in femtosecond stimulated Raman spectroscopy [9] and 2D coherent spectroscopy [10, 11], and at high photon energies such as in (resonant) X-ray absorption/emission spectroscopy ([12–15]). A crucial step towards an in-depth understanding of processes in natural and synthetic systems on the macroscopic scale, such as complex aqueous biological systems, and atmospheric aerosols, is to study the active molecules *in-situ* with the same level of detail as the isolated molecules. Our approach is to study the final ionic products using advanced charged particle 3D momentum imaging spectrometers, that can provide detailed information on energy transfer at the atomic level (e.g. [16]). Using this type of spectrometer, the use of (soft) X-rays are most suitable due to their ability to focus to small length and times cales. In this thesis, we study the energy and charge transfer on the molecular and

nanometer scale in increasingly complex systems. Below, we will give a few examples of atmospheric, biological and material systems where nanoscopic energy and charge transfer processes are at the origin of important properties.

Atmospheric aerosols Condensation and cloud formation is an important process in the earth's water cycle. The calculation of atmospheric condensation rates forms the largest single uncertainty in the current climate models [18], due to the many factors that influence it. Recently, molecules ionized by cosmic background radiation, have shown to influence the nucleation rate [19–22]. The charge stabilizes large aerosols and increases nucleation rates due to the long range charge-dipole interaction with neutral molecules. The understanding of nucleation and fission processes of charged aerosols is thus important to predict atmospheric nucleation rates.

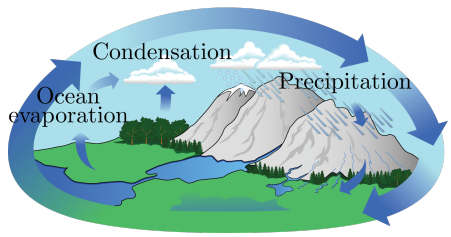

Figure 1.1: Schematic diagram of Earth's water cycle: vapour from oceans and lakes condensates to form clouds and precipitate back to earth's surface. Adapted from [17].

Fuel cells Understanding charge transfer can lead to improvement of the performance and lifetime of engineered structures. For example, a fuel cell converts the chemical energy of a fuel (often molecular hydrogen), into electrical energy, by the use of an electrolyte; a functional material that transmits protons formed from molecular hydrogen at the anode, to recombine with oxygen at the cathode of the hydrogen fuel cell (see Figure 1.2). Current fuel cell research aims for a deeper understanding of the proton transport processes that affect the bulk properties of different electrolyte materials [23].

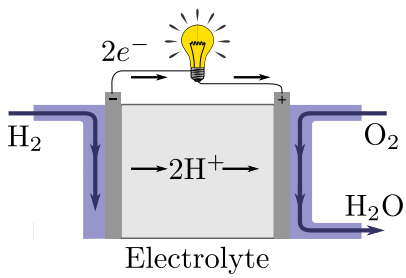

Figure 1.2: Schematic representation of electro-chemical flows in a hydrogen fuel cell. The electrolyte keeps the molecular hydrogen and oxygen separate, while transmitting protons.

Cell biology The study of proton transfer and single molecule conformational isomerization upon light absorption can aid the understanding of complex mechanisms in biological systems. For instance, the transport of ions or molecules across biological cell walls (membranes) is often facilitated by membrane transporters.

One of the simpler examples of such a protein is the bacteriorhodopsin protein (BR), a proton transporter powered by light absorption [25, 26]. The protein is embedded in the membrane, and can pump protons out of the cell using the energy from light absorption. This can lead to four orders of magnitude difference in proton concentration between the in- and outside of the cell [24]. The transporting mechanism involves the transition between the conformational cis- and trans-isomerization upon photon absorption of the light-sensitive part of the molecule, the retinal. This triggers a sequence of protein deformations that facilitates hydrogen atoms and protons to move in between the helical structures of the protein, see Figure 1.3. This membrane transporter is a prototype of many, more complex proteins that are found in biological cells.

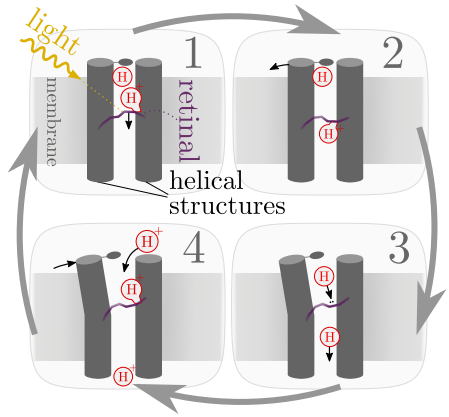

Figure 1.3: Molecular mechanisms in the bacteriorhodopsin protein. Photon absorption of the retinal, leads to conformational isomerization (1), moving the bonded proton (2). The proton then moves further across the membrane (3), and a new proton binds to the lone pair in the retinal, after which the structure closes (4). Drawing adapted from [24].

Processes in bulk systems, such as those discussed above, are difficult to investigate *in situ*. Therefore, we study the charge transfer processes in a bottom-up approach in prototype systems, starting from a single free molecule to a few molecules bonded into a cluster. The size of prototype systems can be controlled, allowing to shed light on the size evolution of the processes under study, from the single-molecule response to liquid-like behavior when many molecules are bonded in a cluster (Figure 1.4).

The experiments are initiated by photon absorption, and the subsequent response of the system is studied. In free molecular systems, X-ray photon absorption can transfer energy in a selected location, i.e. by targeting core orbitals of different electron binding energies. The following photoexcitation or photoionization acts as a trigger to initiate energy and charge transfer processes from the ionization center. The dependence of these processes on the ionization site is called the site-selectivity [27, 28]. We investigate the site-selectivity upon ionization of similar elements at different molecular sites.

The energy and charge flow upon ionization is spatially limited to Ångström length scales in single molecules, but expanded towards nanometer-scale in clusters and liquids (see Figure 1.4, bottom). The ionization of a molecule (A) is influenced by the presence of neighboring molecules (B) on a femtosecond timescale, through autoionizing mechanisms such as Intermolecular Coulombic Decay (ICD) [16, 29, 30] and Electron Transfer Mediated Decay (ETMD) [31–33]. Futhermore, the transfer of a proton from one molecule to a neighbor in hydrogen-bonded clusters happens within a few tens of femtoseconds after ionization [34–37].

At longer time scales, more molecular units around the ionization center are involved (C), and the process can better be described as a statistical mechanism. The environment around the ionization center can act as an energy absorber, exciting vibrational and rotational degrees of freedom in the surrounding molecules [38],

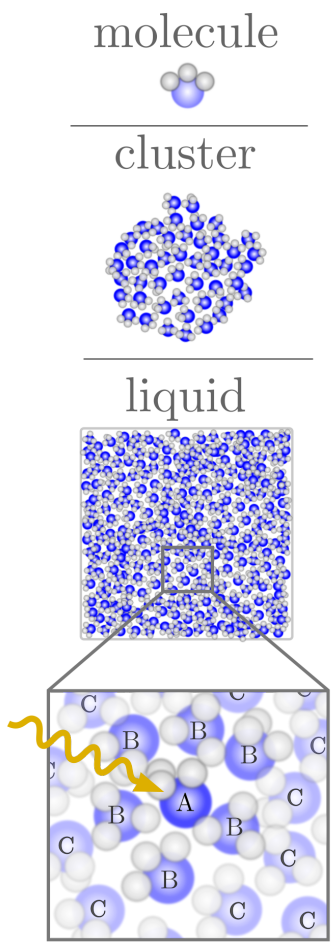

Figure 1.4: How do the energy and charge transfer processes change from an isolated molecule (a) to a free cluster (b), and a liquid (or bulk, c) environment? The inset (bottom) shows a zoom view of the photon absorption by a molecule (A), surrounded by nearest neighbors (B), embedded in a bath of molecules (C).

and acting as a charge transporter. This can ultimately lead to the stabilization of a multiply-charged system, whereas a single isolated molecule would dissociate. As the cluster size increases, macroscopic variables such as temperature, surface tension and permittivity become useful in the description of the observed processes, and we explore the transition from the molecular to macroscopic dynamics.

Scope

To facilitate the investigations of charge and energy flow in free molecules and molecular clusters, we have developed advanced spectroscopic techniques and instruments. An ion-electron mass and 3D momentum-imaging coincidence spectrometer is designed, optimized and tested. Tunable synchrotron radiation and high-intensity Free Electron Laser (FEL) radiation are employed as light sources, depending on the research aim of the experiment. Analysis methods have been developed and applied, in particular to study the correlation between momenta of multiple particles. The coincident mass and momentum measurement of correlated electrons and ions allows us to characterize the mechanisms that lead to the dissociation into fragments.

The thesis is organized as follows: The theory behind light-matter interaction and induced relaxation dynamics in increasingly complex systems is discussed in chapter 2. The experimental setup, such as the spectrometer design and characterization, as well as the molecular beam and light source are presented in chapter 3. The data treatment techniques developed in this thesis are presented in chapter 4. The research work on molecules and molecular clusters, focused on increasingly complex systems, is summarized in chapter 5.

Chapter 2

Theory of photo-induced processes

The fundamental processes we are interested in are charge and energy transfer processes initiated by photon absorption, in increasingly complex systems (from molecules to clusters). Generally, photoabsorption can result in the emission of a photoelectron (photoionization), or the photon energy is converted to electronic energy by promoting an electron to an unoccupied orbital (photoexcitation). After photoabsorption, the system can be electronically excited, and spontaneous electronic decay to a state of lower electronic energy can occur. Additionally, charge (and possibly proton) motion is initiated by photon absorption. This can occur within a molecule, but the presence of neighboring molecules in a cluster generally facilitates inter-molecular energy transfer processes. This section will present the photo-induced charge transfer in increasingly complex environments.

2.1 Light-matter interaction

Photon energy Photoabsorption by an atom or molecule can initiate different processes, depending upon the photon energy. In the visible spectral region, the absorption of a photon can result in emission of another photon (Raman or Rayleigh scattering [39, 40]). At photon energies significantly larger than the binding energy of the electrons (e.g. gamma rays), inelastic scattering (collisions) between photons and electrons becomes the dominant process, and the atomic/molecular orbitals do not play a determining role. In the UltraViolet (UV) and X-ray regime, the photon energy is of the same order of magnitude as the binding energies of bound electrons. An UV or X-ray photon can therefore promote electrons from one orbital to another, unoc-

cupied orbital or into the continuum. We are interested in the consequences of instant energy deposition, and want to control the initial electronic state, which is best achieved by the use of (soft) X-ray photons.

Photoionization and photoexcitation To remove an electron from an atomic or molecular orbital with a single photon requires the photon energy to be equal or larger than the orbital binding energy (photoionization), as observed in the photoelectric effect [41, 42]. The difference between the photon energy and the kinetic energy of the photoelectron is defined as the binding energy of that electron, and ionization can thus occur via each electron with a binding energy less than the photon energy. Alternatively, if the photon energy is equal to the difference of an occupied and unoccupied orbital energy, an electron from the occupied orbital can populate the unoccupied orbital (photoexcitation). Core excitation does not directly create a charged molecule, but rather an electronically excited one. Photoexcitation allows us to choose transitions by tuning the photon energy that matches the energy difference between the electronic states (resonant excitation). Photoionization and photoexcitation of core electrons is schematically presented in Figure 2.1 b and c, respectively. The different photoabsorption methods can be used as tools to perform different experiments; ones where many different states are populated by ionizing electrons from different orbitals, at one photon energy (photoionization), and others where the dominant result is an electron exchanging orbitals (photoexcitation).

Auger decay The removal of a core electron creates a vacancy in a deeply bound orbital, which will often be filled within a few femtoseconds [43, 44]. The electronic energy of the core-hole state is so high that the discrete electronic state is embedded in the auto-ionization continuum. The system can decay to a lower-lying state through emission of a photon (radiative decay), but core-excited states of light elements almost always decay through autoionization in a so-called Auger transition (Figure 2.1c), first observed by Meitner [45]. In core electron excitation, the excited electron can be involved (participator) or not (spectator) in the Auger decay (e.g. see Figure 2.1c). The time between core ionization and Auger electron emission (the *core hole lifetime*) is inversely propotional to the Auger decay rate [46]:

$$\Gamma_{i\to f} = \left| \sum_{a<b} \underbrace{\langle \Psi_f | c_b c_a c_c^\dagger | \Psi_i \rangle}_{\text{overlap}} \underbrace{\langle \phi_c \phi_\epsilon | \tfrac{1}{r_{12}} | \phi_a \phi_b \rangle}_{\text{electron interaction}} \right|^2 , \tag{2.1}$$

where $|\phi_c\phi_e\rangle$ denotes the two-electron wavefunction consisting of a core electron (ϕ_c) and free Auger electron (ϕ_ϵ), and $|\phi_a\phi_b\rangle$ the wavefunction where the two involved valence orbitals ($\phi_{a,b}$) are populated. The sum is over all combinations of ϕ_a and ϕ_b valence orbitals. The indicated overlap integral represents the integral of the adapted initial state wavefunction ($c_b c_a c_c^\dagger|\Psi_i\rangle$), and the final ($|\Psi_f\rangle$) state wavefunction, with ($c_c^\dagger$) the creation operator of an electron in the core orbital, and annihilation operators ($c_{a,b}$) of two electrons in valence orbitals a and b, respectively.

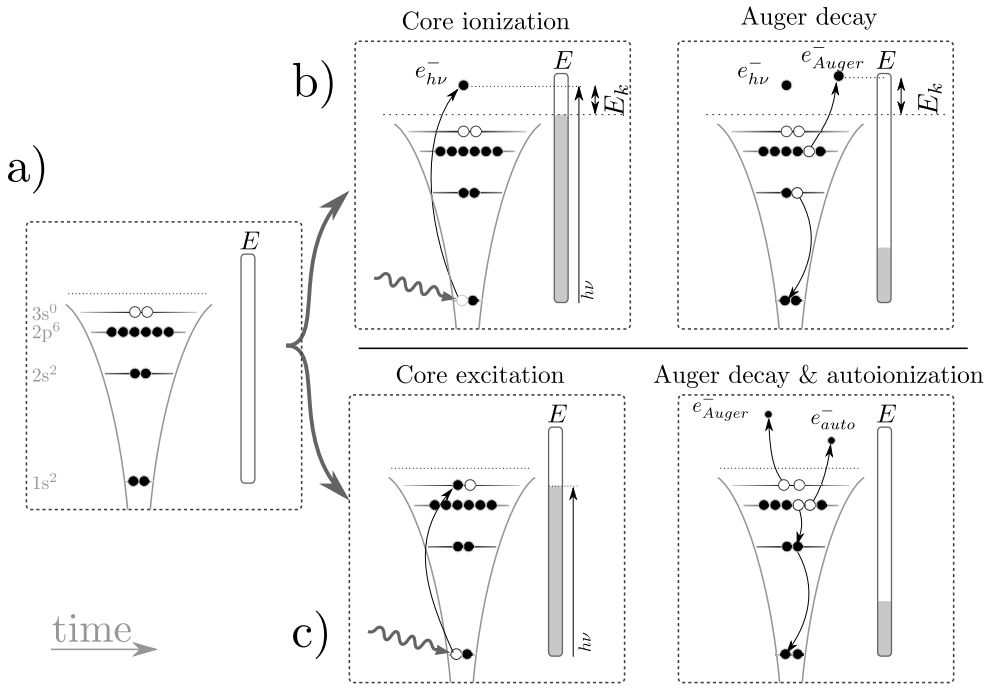

Figure 2.1: A simplified representation of typical orbital energy levels and their occupancy in a free atom/molecule (a), with an indicator of the internal energy (E) on the right, and the effect of core photoionization and photoexcitation, in this case from a 1s orbital. Core ionization (b) directly produces a singly charged atom, and the high internal energy leads to further autoionization (Auger decay). Core excitation (b) promotes the core electron to a higher-lying unoccupied orbital. Further auto-ionization processes can lead to a doubly charged atom, such as shown in this example.

The core vacancy is localized to a specifc atom, but this does not imply that the molecular Auger rates are solely dependent on the intra-atomic part of the wavefunction. The chemical environment of the molecule can influence the core hole lifetime. For example, the carbon core hole lifetime is increased from the methane case (CH_4, 6.3 fs) when the hydrogen atoms are exchanged by chlorine atoms one by one (10.6 fs for CCl_4 [47–49]). The increase in lifetime is an effect of the decreasing valence occupancy, and thus overlap, around the carbon nucleus, due to the electronegative chlorine.

If the Auger populated states are still embedded in the double ionization continua, further auto-ionization through radiationless decay can occur. Autoionization most often occurs through another Auger decay (Auger cascade [50, 51]), but electron shake-off or knock-off can also lead to a higher ionization state [52] (see Figure 2.1c, right).

2.2 Intra-molecular processes

So far, we have considered the processes induced by photon absorption to be of local (nuclear) nature, similar to those occurring in isolated atoms. However, in this thesis we study atoms bonded together into a molecule, in which the light-matter interaction and following electronic decay is influenced by the chemical environment. The molecular response to photon absorption is thus different than the atomic case. Most importantly, the molecule can dissociate into smaller molecules (or atoms). We will briefly discuss the theory behind molecular bonding, and continue by discussing the different types of dissociation that can occur.

Molecular orbitals A molecule can be described as an uncharged collection of nuclei and electrons, forming a stable ensemble; the total energy of the assembled molecule is lower than that of the separated atoms. The Hamiltonian (energy) operator of a molecule can be split into three terms:

$$H = T_N + T_E + V, \tag{2.2}$$

which is a sum of the kinetic energy of the nuclei and the electrons (T_N and T_E, respectively), and the potential energy V. In the case of a diatomic

molecule, the potential energy can be expressed as:

$$V = \frac{e^2}{4\pi\epsilon_0}\left(\underbrace{\sum_{i<j}^{N}\frac{1}{|\mathbf{r_i}-\mathbf{r_j}|}}_{\text{e-e repulsion}} + \underbrace{\frac{Z_A Z_B}{R}}_{\text{N-N repulsion}} \underbrace{-\sum_{i=1}^{N}\left[\frac{Z_A}{|\mathbf{r_i}-\mathbf{R_A}|}+\frac{Z_B}{|\mathbf{r_i}-\mathbf{R_B}|}\right]}_{\text{e-N attraction}}\right) \tag{2.3}$$

with the nuclei named A and B, N the number of electrons, R the internuclear distance ($R = |\mathbf{R_A} - \mathbf{R_B}|$), $Z_{A,B}$ the nuclear charge and r_i the position vector of electron i, e the elementary charge, and ϵ_0 the permittivity of free space[1]. The Hamiltonian operator couples the electronic and nuclear parts of the wavefunction. The Born-Oppenheimer approximation states that, due to the large difference of the typical mass of electrons and nuclei, the motion of the nuclei is much slower than that of the electrons. This allows one to write the wave function as a product of an electronic and nuclear part [53]:

$$\Psi = |\psi_e\rangle|\psi_N\rangle, \tag{2.4}$$

where ψ_N represents the nuclear wavefunction, and ψ_e the electronic wavefunction that depends parametrically on the nuclear positions. This leads to the electronic and nuclear wave equations:

$$(T_E + V)\,|\psi_e\rangle = E_E|\psi_e\rangle \tag{2.5}$$

$$T_N^*|\psi_N\rangle = (E - E_E)\,|\psi_N\rangle \tag{2.6}$$

where T_N^* is the uncoupled nuclear potential energy operator[2]. The electronic equation can be solved to yield the electronic state energy, E_E, with which the nuclear wave equation can be solved to calculate the total energy E.

The (nuclear or electronic) kinetic energy is always greater than or equal to zero, and so are the electron-electron and nucleus-nucleus repulsion terms in Eq. 2.3. The only term that causes a decrease in the total energy is thus the electron-nucleus attraction.

When two isolated atoms approach an internuclear distance of a few Ångström, the atomic orbitals can interact and form different molecular orbitals. The energy of these orbitals can be lower (bonding), higher (antibonding) or be equal to (non-bonding) the average energy of the two atomic

[1] The generally small spin-dependent terms are neglected

[2] The definition and detailed derivation of T_N^* can be found in [54]

orbitals. A bonding orbital can be formed between nuclei, when the electron density between the nuclei exceeds that of the sum of two non-interacting atoms at the same internuclear distance, since this increases the magnitude of the electron-nucleus attraction term (or decreases T_N around the nuclei [55]). Only unpaired electrons (one electron in an orbital, with spin up or down) contribute to chemical bonding, which is why noble gas atoms are chemically inert[3].

The potential energy increases as nuclei move even closer (sub-Ångström), due to the increasing nuclear repulsion. A bonded molecular system can thus stabilize in a configuration with a local potential energy minimum. This is often described as a minimum in the *potential energy surface*, where the dimension of the surface is determined by the number of nuclear degrees of freedom in the molecule. In a diatomic molecule, the surface reduces to a curve, since the internuclear distance is the only degree of freedom. In many-atom molecules, the term *reaction coordinate* is often used, which can represent a certain (combination of) nuclear degree(s) of freedom, or a pathway of geometries that the molecule is expected to follow during a (chemical) process.

The nuclear wavepacket can oscillate around a potential energy minimum when it gets vibrationally excited. The oscillation frequency scales with the steepness of the potential energy surface around the minimum (k), and the reduced mass of the system (μ) as $\omega \propto \sqrt{k/\mu}$. For example, the first vibrationally excited state of CO has an energy of 0.2 eV above the ground state energy, and oscillates with a period of 16 fs. An increasing number of vibrational modes exists in larger molecules, such as bending, wiggling, scissoring, torsion, as discussed in the supplemental material of **Paper II** for 1,3 *trans* butadiene.

In molecules consisting of more than two atoms, the molecular orbitals that participate in bonding can spread across several nuclei. An example of two different electron orbitals in 1,3 *trans* butadiene ($H_2C{=}CH{-}CH{=}CH_2$), one of the molecules studied in this thesis, are shown in Figure 2.2. Butadiene has a planar geometry with C_{2v} symmetry in the ground state, with two distinguishable nuclei, denoted the *terminal* and *central* nuclei. The Highest Occupied Molecular Orbital (HOMO) is mostly concentrated around the bond between terminal and central nuclei (terminal bond), increasing the (double) bond strength. The Lowest Unoccupied Molecular Orbital (LUMO) is mostly localized at the central C-C bond, also in a π-configuration, and the occupa-

[3]This does not exclude a net attractive force between the atoms, such as through van der Waals interaction

tion of this bond could lead to a stronger central C-C bond[4].

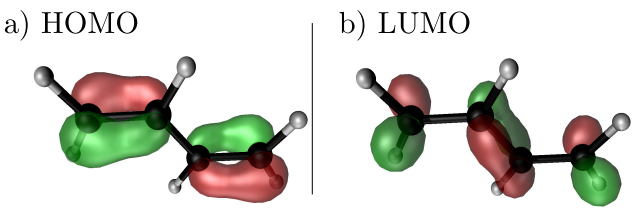

Figure 2.2: Iso-contour plots of the Highest Occupied Molecular Orbital (HOMO, a) and the Lowest Unoccupied Molecular Orbital (LUMO, b) of 1,3 trans butadiene.

Nuclear dynamics in core ionized states Since the electron mass is about three orders of magnitude smaller than a typical nuclear mass, it is often assumed that electronic processes such as photoionization and -excitation occur in a fixed nuclear arrangement (Born-Oppenheimer approximation). Therefore, it can often be assumed that the Auger decay precedes the rearrangement in the molecule (e.g. [56]). The *Franck-Condon* principle assumes that a vibronic (= vibrational and electronic) transition occurs in a stationary nuclear framework and that the transition probability to a certain state depends on the wave function overlap of the initial and final state. However, nuclear motion within the core hole lifetime can not always be ignored, as demonstrated by the observation of *ultra-fast* dissociation [57], i.e. breakup that is faster than electronic relaxation. If photoexcitation leads to a highly repulsive electronic state, the nuclei are already separated before Auger relaxation occurs. The Auger electron is thus emitted from a fragment, rather than the intact molecule. This extremely fast fragmentation before decay is limited to a few cases (often hydrogen halides such as HCl [57, 58]). At higher nuclear masses, the Auger lifetime is of the same order of magnitude as the dissociation time, or smaller.

Site- and state-specific photofragmentation The localized core hole can cause bond breaking close to it, referred to as site-selective bond breaking or site-selective dissociation [59]. The effect was first observed in small molecules by Eberhardt and co-workers [27, 28], and examples of strong site-specific behavior can be seen after core-ionizing halogenated alkanes (e.g.

[4]The molecular orbitals in the neutral ground state are different in an ionized or excited state, and more reliable predictions on bond strengths requires the study of the orbitals in those states.

$Br(CH_2)_nCl$ with $n = 1, 2, 3$, [60, 61], CF_3CH_3, [62] and BrC_2H_4I[63]). However, the ionization site is not the only determining factor, since an increase in internal energy (after Auger decay) has shown to decrease the site-selectivity of the fragmentation [61]. Moreover, in some molecules where no site selectivity is observed, the only relevant parameter for the dissociation pattern seems to be the internal energy (e.g. [64, 65]). The internal energy dependence can be interpreted as a fast distribution of the electronic energy into vibrational excitations [61], or as a consequence of similar populations of Auger final states [65].

In some cases, the final electronic state (rather than the excitation site) determines the fragmentation pattern of a molecule. In such a state-selective dissociation, different electronic states (with similar internal energy) can still result in a different fragmentation pattern (e.g. in acetaldehyde, acrylonitrile and 2Br-pyrimidine [66–68]), attributed to a change in charge distribution of the different electronic states [69], possibly influencing the bonding properties of the molecule. This could even cause a bond break between atoms of which none are core-ionized [70]. We have studied the site- and state-specific fragmentation through photoionization in **Paper I** and through photoexcitation in **Paper II**.

Coulomb explosion After electronic relaxation, the molecule has vacancies in the (inner-)valence orbitals. These orbitals are spread over mutiple nuclei, and are generally more delocalized than core orbitals. If two electrons are removed from the neutral molecule, the Coulomb repulsion between the two charges (vacancies) often causes the charges to separate, and break the molecule. If the fragmentation is dominantly driven by Coulomb repulsion, the breakup is referred to as a *Coulomb explosion* [71]. The energy released by a pure Coulomb repulsion can be calculated from the classical repulsion between point charges. In the case of two charges, we can write

$$T_C = \frac{1}{4\pi\epsilon} \cdot \frac{q_1 q_2}{R} \tag{2.7}$$

for T_C as the Coulomb kinetic energy. $q_{1,2}$ as the charges on point one and two, respectively and R as the distance between them. An example of pure Coulomb explosion is the hydrogen (or deuterium) molecule [72, 73], where the doubly charged molecule consists of only two bare nuclei, without (antibonding or bonding) electrons influencing the dissociation. In this case, double ionization maps the nuclear vibrational wavefunction to the Coulomb potential energy surface. The kinetic energy of the protons (deuterons) can thus be compared to the energy of two singly charged point-masses that are spread around

the equilibrium nucleus-nucleus distance. The relation between kinetic energy and internuclear spacing in many molecules cannot be determined without considering the (anti-)bonding role of the remaining electrons. However, the contribution of the Coulomb potential to the measured kinetic energy distribution might be dominating, especially at an initially small charge-charge (or internuclear) distance. For example, a typical kinetic energy distribution of CO fragments is presented in Figure 2.3. The measured kinetic energy of the two body breakup ($CO^{2+} \rightarrow C^+ + O^+$) is close to the one expected from two classical point charges at the neutral ground state equilibrium distance, indicating that the Coulomb repulsion dominates the kinetic energy of the two fragments.

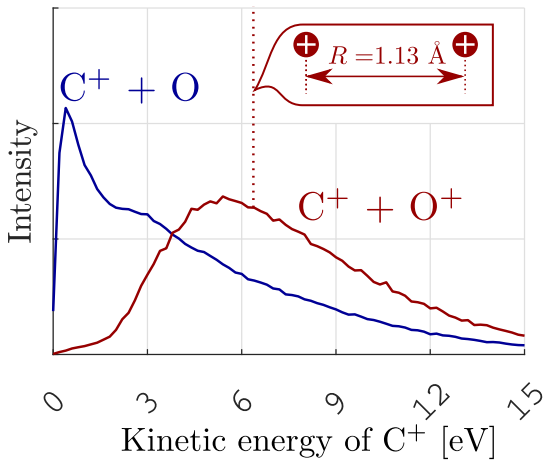

Figure 2.3: Kinetic energy distribution of carbon ions (C^+) from CO photoexcitation ($C1s \rightarrow \pi^*$) into singly (blue) and doubly (red) charged dissociation. The red vertical line indicates the expected kinetic energy from a classical Coulomb explosion of point charges at the CO equilibrium distance [74].

2.3 Intermolecular interactions

When a molecule is embedded, for example solvated in water, it can interact with its environment after photon absorption. In this section, we focus on fast interactions, i.e. on time scales typically in the same order of magnitude as the core hole lifetime (femtoseconds). We study hydrogen-bonded clusters and therefore highlight the processes involving proton transfer.

Hydrogen bonding Molecules can stick to other particles in different ways. In principle, the bonding can be any type of intermolecular/interatomic force, e.g. ion-ion interactions (electrostatic), van der Waals bonding, or hydrogen bonding. In this section, we present the general properties of hydrogen bonding. The importance of the hydrogen bond in charge and proton transport will be discussed in the subsequent paragraph.

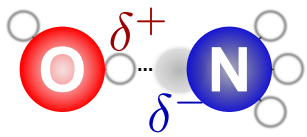

Figure 2.4: The hydrogen bond is formed between an electronegative atom (oxygen) and a nucleus with a lone pair electron (nitrogen), in this example connecting a water and ammonia molecule.

If a hydrogen atom is covalently-bonded to a more electronegative atom (the hydrogen donor, e.g. O−H), the proton is slightly bare, i.e. the shared electron orbital is more localized at the electronegative atom. This forms a dipole, with the hydrogen at the outer end slightly positively charged. The hydrogen end can form a hydrogen bond with a negatively charged part of a nucleus (the hydrogen acceptor), due to a lone pair, see Figure 2.4. The hydrogen bond is mainly electrostatic in nature. However, the water-water hydrogen bond, for example, can partly be described as a covalent bond [75].

A hydrogen bond has a typical dissociation energy of 0.1-0.2 eV [76], and is highly directional. If the proton donor and acceptor are not aligned correctly, the hydrogen bond is not formed, and the hydrogen bond is strongest when the donor-hydrogen-acceptor nuclei are aligned. Therefore, hydrogen bonding has an effect on the relative molecular orientation. This can be observed in every day life in the expansion of water when freezing; the amorphous liquid crystalizes and forms hydrogen bonds. The molecules need to orient with respect to each other, which requires more space per molecule and causes an increase of the specific volume.

Proton transfer If a hydrogen-bonded donor molecule is ionized, the hydrogen-donating atom becomes even more electronegative, and a bare proton can

transfer along the hydrogen bond to the hydrogen-accepting neighbor. This process happens on a femtosecond time scale after ionization [35–37], of the same order of magnitude as the core hole lifetime. Proton transfer can therefore play a role in electronic (Auger) decay.

Electronic relaxation Core photoionization and photoexcitation acts on one atom in a molecule, even when this molecule is embedded within a molecular ensemble. The following Auger decay can also remain relatively similar to the single-molecule response (e.g. see Figure 2.5a). However, within the typical core-hole lifetime, the excited molecule can interact with neighboring molecules, opening up a plethora of relaxation processes.

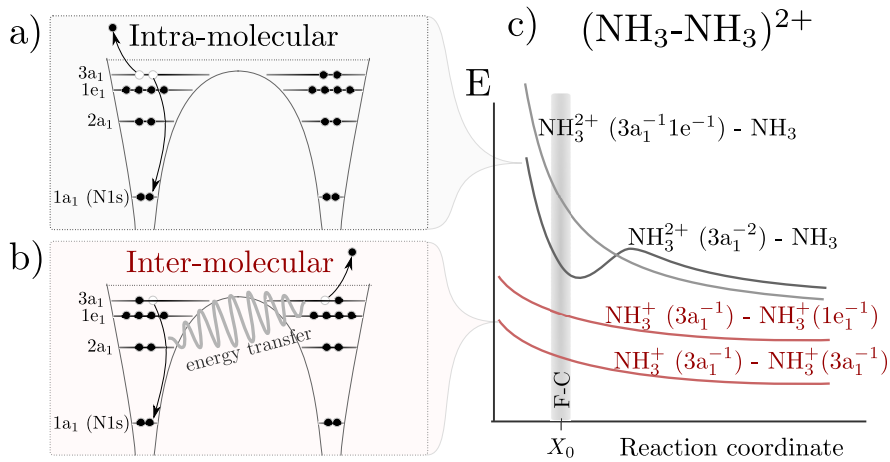

Figure 2.5: The schematic energy levels and occupation of orbitals of the ammonia dication dimer after intra-moleculer electronic decay (a) [77, 78], and inter-molecular electronic decay (b) [79], and the potential energy curves for the different orbitals involved (c)[1]*. Note that inter-molecular decay always leads to a lower internal energy, with a repulsive potential energy surface (Coulomb explosion). The vertical bar indicated by 'FC' is the Franck Condon region within which transitions occur without nuclear geometry change. The reaction coordinate is the N-H and ammonia-ammonia distance in the case of intra- and inter-molecular electronic decay, respectively.*

[1]The molecular orbitals are named according to their symmetry: 'a' and 'b' stand for orbitals with and without rotation symmetry (around the molecular symmetry axis), respectively, and the subscript '$_1$' and '$_2$' stand for orbitals with reflection symmetries in different planes of the molecule.

One of those fast interactions is Interatomic Coulombic Decay (ICD) [16, 29, 30, 80, 81]. Many forms of ICD have been predicted and observed, but the most generally observed process (direct ICD) can be compared to the normal Auger decay mechanism, where the emitted electron originates from a neighboring molecule (or atom), instead of the same molecule (compare Figure 2.5a and 2.5b). Note that ICD results in a larger charge separation than Auger decay, and that both molecules are singly charged. The energy required to singly ionize two molecules is lower than the double ionization of one molecule, and ICD therefore yields an overall lower final electronic energy. ICD has been shown to occur in many samples, and on a short time scale, for example in the water dimer[2], where it was shown to be faster than proton transfer [82].

The electronic decay can even involve two electrons of a neighboring molecule; Electron Transfer Mediated Decay (ETMD) can be described as Auger decay where both electrons (the one filling the vacancy and the one promoted to continuum) originate from the neighboring molecule(s) [31–33], see Figure 2.6. The internal energy after ETMD is as high as normal Auger decay if both electrons come from the same neighboring molecules [called ETMD(2)], but can be lower than the final ICD state if the emitted electrons originate from different molecules [called ETMD(3)].

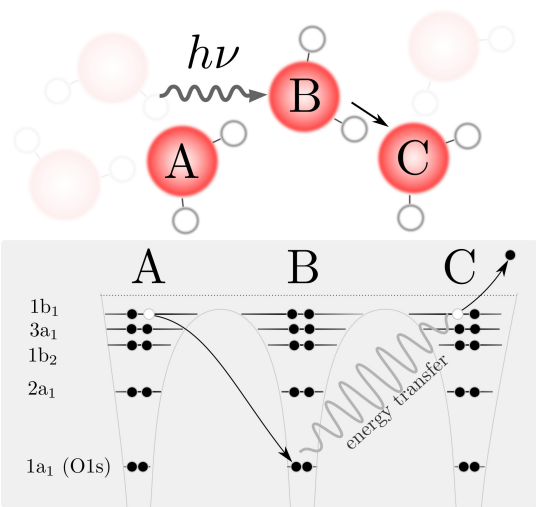

Figure 2.6: Simplified schematic of the three-molecule ETMD: Hydrogen-bonded neighboring molecules of a core-shell photoionized water molecule (B) can influence the decay by electron and proton transfer. In this example, one valence electron from a molecule A occupies the core vacancy, and molecule C ejects a valence electron.

The transition rate of ICD and ETMD processes depends strongly on

[2]Dimers, trimers, tetramers, etc. are names for clusters with two, three, four, etc. atoms or molecules

the internuclear distance, but could still occur without nuclear motion (i.e. a so-called vertical transition [3]). However, in a hydrogen-bonded network, a lightweight proton can move a significant distance within the core hole lifetime (9 femtoseconds as a typical vibration period). The proton can thus influence the electronic decay after core ionization in hydrogen bonded-networks [83, 84]. For instance, the core ionization of liquid water can lead to a fast proton transfer that decreases the internal energy after electronic decay [85, 86].

As the bonding in a condensate of molecules (or atoms) increases, the orbitals can become more *delocalized*. Electrons from these delocalized orbitals can be involved in Auger transitions, such as observed in hydrogen-bonded water clusters [87]. The spread of orbitals over several molecules implies that the potential barrier in Figure 2.5b) can be below the highest occupied molecular orbital.

[3] A vertical transition can be presented by a vertical line in a schematic of internal energy vs reaction coordinate, e.g. in Figure 2.5

2.4 Multi-body processes

In the previous sections, we introduced the processes that occur while the molecule is in the core-hole state. Multiply-charged free molecules break up during or shortly after the core-hole decay, forming singly-charged fragments. A major part of this thesis concerns the study of free molecular clusters, i.e. a bunch of molecules bonded together. The surrounding molecules can influence the breakup process in many ways, such as sterically hindering the breakup into singly charged fragments, or enabling the exchange of protons across hydrogen bonds. The cluster can even stabilize and host multiple charges where a single molecule would readily dissociate. This section introduces the multi-body processes that can occur after electronic decay of free clusters, with an increasing number of molecules involved: from Ångström to nanoscopic length scale.

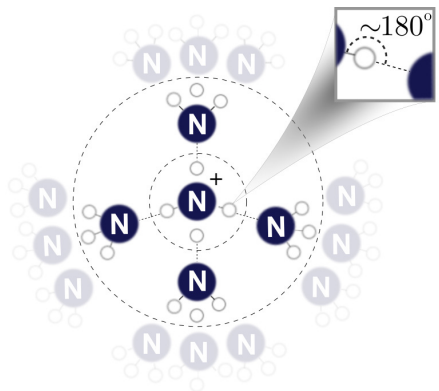

Figure 2.7: Schematic representation of the ammonium (NH_4^+) center and ligands. A second layer of ligands can bond to the first layer (semi-transparent). The inset shows the hydrogen bond angle, approaching 180 degrees in this geometry. Figure adapted from [88].

The ionization of valence electrons in a hydrogen-bonded molecule can cause a fast transfer of a proton along the hydrogen bond, towards the hydrogen acceptor. The neighboring molecule has now an extra covalently-bonded proton (it is *protonated*) and a single charge. The covalent bond is formed with the lone pair of the hydrogen acceptor. For example, $NH_3^+{-}NH_3$ can form $NH_2{-}NH_4^+$ within a few femtoseconds [35–37].

The protonated molecule forms a strong hydrogen donor (from 0.2 to 0.5 eV [88] hydrogen bond energy, in the example of NH_4^+), causing the hydrogen bond angle to become closer to 180 degrees [76], and the surrounding molecules to form a *shell* of ligands around the protonated core (see inset in Figure 2.7).

The protonated core forms as many hydrogen bonds as its number of protons, and thus acts as a donor only. In the case of ammonium, there are thus four molecules (or *ligands*) that can bind directly to ammonium (see Figure 2.7) and form a first *shell*. The hydrogen bond strength between the ammonium and the ligand is stronger than a neutral ammonia-ammonia bond

due to the ion-induced dipole interaction [89]. The filling of the first shell can be observed as a higher stability of that number of molecules. This number of molecules is often referred to as a *magic number* [90, 91]. The bonding of more molecules to these four ligands can form a second shell, now with $(4 \cdot 3 = 12)$ available spots. In water, the configuration of hydronium (H_3O^+) hydrogen bonded to three ligands is often referred to as the *Eigen* structure [92, 93].

Proton hopping As discussed, core ionization mostly leads to double ionization in the elements that constitute the systems under study. The presence of neighboring molecules around the ionization point inhibits the direct breakup of the molecule into singly charged fragments, but the repulsive Coulomb force can still cause the charges to move in a cluster. The charge can move by sticking to one host, which moves outward (*vehicular diffusion*). However, the hydrogen bond can ease the charge movement by *hopping* protons from one molecule to another (*structural diffusion*), see Figure 2.8. Structural diffusion can thus transport the charge from one host to another by moving the proton involved in the hydrogen bond between them. This mechanism was first described by De Grotthus [94], and it is now understood that fluctuations in the surrounding hydrogen-bonded environment are important in the description [95]. In Figure 2.9, a schematic representation of the evolution of a hydrogen-bonded (water) network is shown, where the charge hops from one molecule to a nearest neighbor. Note that the transfer is preceded by a hydrogen bond breaking outside the ligand structure. The decrease in coordination number creates the possibility to transfer a proton along that bond. During the transfer (Figure 2.9c), the proton is in between two nuclei, in a so-called *Zundel* configuration [96]. From that configuration, the proton can transfer to the new host (Figure 2.9d).

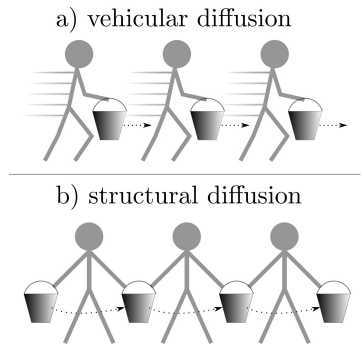

Figure 2.8: Diffusion of water on the meter length scale: Vehicular diffusion is transport of the diffusive species (bucket) by only one host (a), while the buckets hop across (more or less static) hosts in structural diffusion (b).

The proton hopping happens spontaneously in room temperature water [95], and occurs on the picosecond time scale (1,5 ps in liquid water [97], similar to the typical lifetime of a hydrogen bond in the medium [98, 99]).

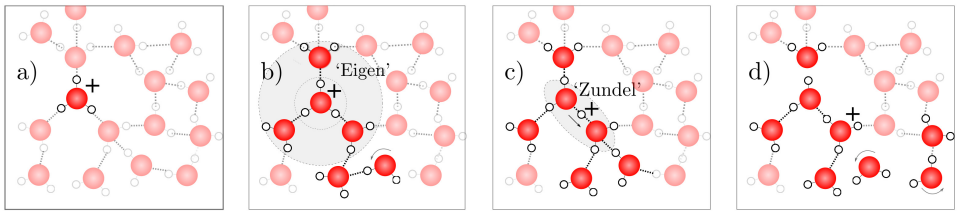

Figure 2.9: Schematic representation of proton hopping in a water network, and the evolution of proton bonds that form and break in the process. The hydronium (a) can bond to three surrounding ligands (b, the Eigen structure). The breaking of a hydrogen bond at the ligands facilitates the proton motion (c, Zundel structure), and moves the charge to a new host (d). Figure adapted from [95].

The hopping happens in random directions, but aligns to an electrostatic field as the field strength increases [100]. The proton hopping can thus cause a separation of the charges, and the increase of charge-to-charge distance will slow down as the distance increases (lower Coulomb force), but can cause a fission of the cluster into multiple charged fragments. As mentioned earlier, the protonated molecule tends to form a core with unprotonated ligands around it, resulting in magic numbers at which the structure is particularly stable. The relative abundance of fragments with magic-numbered sizes gives information on the time scales of the formation of this core-shell structure, relative to the fission process, and is studied in **Paper V** and **VI**.

Evaporative cooling The proton hopping vibrationally excites the involved molecules, thus increasing the average kinetic energy contained by a molecule (i.e. an increase of temperature). When the average internal energy approaches the cohesive (or binding) energy of a bonded molecule, molecules with high internal energy can evaporate from the cluster surface, effectively decreasing the average temperature. The time scale of evaporation of single molecules (unimolecular evaporation) after ionization has been measured to be on the order of microseconds for ammonia and water clusters (8-20μs [101, 102]). However, the precise evaporation rate depends upon the amount of energy deposited, as shown by electron impact ionization [103] and theoretical investigations [104].

Critical dication size The separation of charges (and their mutual Coulomb repulsion) is limited by the cluster size. At a critical cluster size, the charges can separate so far that the cluster does not dissociate into fragments, but

remains intact. The critical cluster sizes of hydrogen-bonded clusters are typically a few tens of molecules for two charges (size increases as hydrogen bond energy decreases), and can also be defined for a higher number of charges (e.g. [105]).

This critical size is classically predicted by Rayleigh's stability barrier [106]. In this model, the cluster is treated as a continuous mass, and the fissility parameter (X) predicts the stability of a cluster [107]:

$$X = \frac{Z^2}{64\pi^2\epsilon\sigma a_0^3} \tag{2.8}$$

where ϵ is the permittivity, σ is the surface tension in the medium, a_0 is the cluster radius, and Z is the number of charges. The criterion is used to predict the stability of a liquid droplet with a certain number of charges (Z), and it sets the basis for the Liquid Droplet Model. If $X > 1$, the model predicts fission of the cluster in charged fragments, and if $X < 1$, the cluster is predicted to remain intact. The model is successful in predicting critical cluster sizes (at $X = 1$) of Van der Waals-bonded clusters, due to their isotropic bonding properties. The criterion fails to predict critical sizes of hydrogen-bonded molecules accurately due to their dipolar nature [108], and reliable critical sizes are determined from measurement [105, 109, 110]. The influence of mixing molecular species on the critical dication size is investigated in **Paper VI**.

Inelastic electron scattering A cluster can reach even higher charge states than an isolated molecule through the electron-electron inelastic scattering of the photoelectron or Auger electron at a different site in the cluster. The process can create delocalized charges, where transfer through proton hopping would be of lower importance. Using the cross sections from electron scattering experiments, we can estimate that at most 30-40% of 300 eV free electrons scatter, emitted from the centre of a cluster of 52 molecules in a shell structured ammonia cluster [111, 112]. The scattering events have a near equal probability to result in ionization or elastic scattering [111], so about 15% of these scattering events can lead to ionization. In general, the electron inelastic mean free path, and thus the probability of scattering, is strongly kinetic electron energy dependent [113–116], and the probability of e^-- e^- scattering needs to be calculated for each combination of species, cluster size, and electron energy.

Chapter 3

Experimental setup

In this thesis, we study the consequence of photon absorption of free samples, be they molecules or clusters. Photoabsorption of the samples in this thesis leads mainly to non-radiative products, i.e. ions and electrons. Our approach is to measure the ions and electrons created from ionization or excitation in terms of their momentum, energy, and (ion) mass upon dissociation. In addition, we are interested in the correlation between the electron and ion momenta and kinetic energies, which requires the simultaneous detection of the particles. We discuss here the types of instruments (spectrometers) that can be used for this purpose, and their particular advantages in measuring (the correlation between) ion and electron momenta. After that, the spectrometer design, characterization and performance is discussed.

3.1 Electron-Ion spectrometers

The principle of a spectrometer is to control the trajectories of charged particles through the use of an electro- and magnetostatic field (the Lorentz force), and lead them to a detector. Modeling the trajectory of a charged particle in an electro- and magnetostatic field is often called *charged particle optics* [117, 118], since it bears resemblance to "regular" optics. In the spectrometers used in this work, the electro-/magneto-static field is designed such that the ions and electrons are driven towards their respective detectors, so as to increase the *acceptance angle* of the instrument, i.e. the range of solid angles of emission of a particle that will end up at the detector.

An important factor determining the performance of a spectrometer is the spatial extension of the source volume, defined as the interaction region

between the light and a gas jet. During the past decades various techniques have been used to compensate or minimize the impact of the extended source volume [119, 120], and it is therefore an important topic in the discussion of the spectrometer design.

Ions Ions are often detected by electrostatic mass (and momentum) spectrometers. The difference between the ionization and detector impact times is often called the *Time Of Flight* (TOF). The TOF can easily be translated to the ion's mass over charge ratio (as will be shown in section 4.2). In practice, the possible ionization position is spread due to the finite source volume, effectively changing the distance between ionization point and detector. Many of these ion time of flight instruments are therefore designed to operate under the so-called *Wiley McLaren* (or space focusing) condition [119], with the consequence that a spread in ionization point along the spectrometer axis does not result in a spread in time of flight.

Electrons The electrons often carry more energy (e.g. hundreds of eV from Auger decay), and steering them towards the designated detector is more challenging than in the case of ions. Therefore, different strategies exist to measure electrons, each with their advantages and compromises. When electron energy resolution is of highest priority, the hemispherical [121] (Figure 3.1a), double toroidal [122–124] (Figure 3.1b), or electron TOF (eTOF, e.g. [125]) energy analyzers are most suitable. A hemispherical analyzer is an energy-disperser and therefore only measures the electron energy, at a very high resolution. In addition to the energy-dispersion, the toroidal analyzer can measure the angular distribution of electrons as well. These spectrometers measure with a high energy resolving power (up to $\frac{E}{\delta E} \geq 500$ for the hemispherical analyzer). Their main disadvantage is the limited electron collection efficiency: only a few percent of all free electrons created by photoionization processes reach the detector. If an electron energy analyzer is used in combination with an ion spectrometer, with a high ion collection efficiency, ions are detected without the corresponding electron, and the correlation between detected electrons and ions becomes ambiguous. Therefore, electron-ion coincidence spectrometers equipped with a hemispherical/toroidal energy analyzer often use advanced acquisition schemes with pulsed electrostatic fields that warrant the electron-ion correlation [126].

On the other hand, if measuring the electron's momentum, or direction of emission, is a primary experimental objective, the Velocity Map Imaging (VMI) technique [120, 126–135] (Figure 3.1c) or the REaction MIcrosope

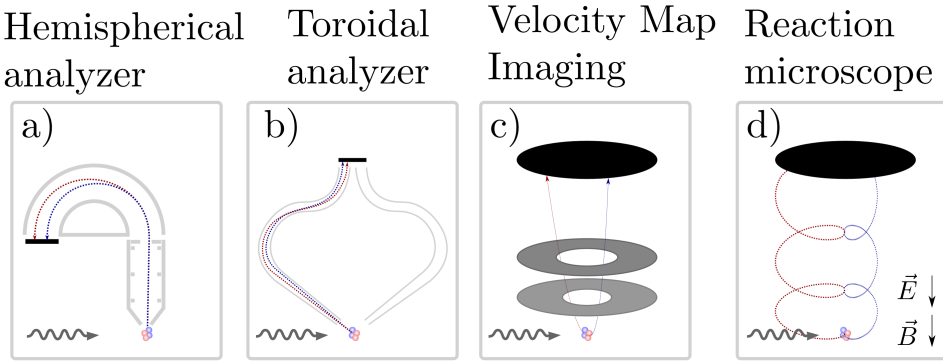

Figure 3.1: A schematic representation of the four different electron spectrometers used in studies in this work. The dotted lines represent possible electron trajectories for a low (blue) and high (red) kinetic energy.

(*REMI*, also called COLTRIMS, Figure 3.1d) [136] is particularly suitable. Both methods can be described as momentum imaging techniques, where the impact position of a particle on a two-dimensional detector yields information on the momentum of the particle, rather than its energy. REMI spectrometers use a uniform electrostatic and magnetostatic field, aligned with the spectrometer axis. The magnetic field restrains the electron to travel in cyclotron motion, restricted to the measurable region of the detector. This allows a lower electrostatic field strength, beneficial for the electron momentum resolution along the spectrometer axis. The high collection efficiencies of REMI and VMI spectrometers involve a compromise in energy resolving power when compared to the dedicated energy analyzers ($5 \lesssim \frac{E}{\delta E} \lesssim 30-100$).

The research question determines which combination of ion and electron spectrometer is most appropriate. The high energy resolution of a (toroidal or hemispherical) electron analyzer enables the identification of ionization sites, if the binding energies of different sites are different due to a chemical shift (**Paper I**). The hemispherical and toroidal energy analyzers are therefore suitable instruments in the study of site- and state-selective studies.

A high mass resolution of ionic fragments makes it possible to unambiguously identify the mass of large molecular and cluster fragments (**Papers V&VI**), and to identify processes where hydrogens have transferred or evaporated (**Papers II&IV**). The measurement of momenta (and angular distribution) of many charged particles is possible by employing a VMI-configuration at both the ion and electron side (**Paper VII**).

3.1.1 Design of an imaging spectrometer

In this work, we have further developed an existing ion mass and momentum spectrometer (bottom of Figure 3.5) to measure the momenta of electrons and ions simultaneously. This section will first describe the existing mass spectrometer, present the design criteria and the numerical simulations that have been performed, and finally show the design choices.

Specifications of the ion spectrometer The ion spectrometer built in our research group [137] has been optimized for high mass resolution and ion collection efficiency (up to 15 eV kinetic energy), and momentum imaging. To achieve this, the following spectrometer properties are important:

- A long TOF spectrometer (~ 0.8m), with double field ion acceleration, to achieve space focusing according to Wiley-McLaren principles and high mass resolution.
- A uniform and strong electrostatic field (about 300 V/cm) in the ionization region.
- An ion focusing lens that minimizes the effect of an extended source volume along the transverse axis of the spectrometer.
- A large, high resolution 2D-position and time (ion) detector[1], to combine a large collection efficiency at high ion kinetic energy with a long TOF drift tube.

An electron time-detector is installed at the side opposite the ion spectrometer. The detection of an electron is interpreted as the start of a measurement *event*, followed by possible detection(s) of correlated ion(s). The ion time of flight is measured by the time difference of electron and ion detection times[2].

Design criteria of the electron spectrometer In order to make preliminary choices for the design of the electron spectrometer, key aspects to achieve the measurement goals are:

- Detect correlated electrons and ions simultaneously.
- Detect electrons with a kinetic energy up to 100 eV.

[1] 80 mm diameter, 50-100 μm spatial resolution, 250 ps temporal resolution (see section 4.1).

[2] The electron time of flight (about 3-4 ns) is much smaller than the ion time of flight (in the order of μs), and can therefore be neglected.

- Measure angular distributions of electrons with up to 100 eV kinetic energy.
- No compromise on the ion measurement quality.
- Velocity focusing to compensate for an extended interaction volume.

The probability to detect correlated electrons and ions is greatly increased when the collection efficiencies of both the ions and electrons are high. Therefore, the use of electron energy spectrometers (such as hemispherical and toroidal analyzers, Figure 3.4a,b), with a low electron collection efficiency, make the correlation of detected particles challenging [126]. In contrast, the velocity map imaging technique (Figure 3.4c) provides a high collection efficiency and can measure angular distributions. The maximum attainable electron energy can be chosen by the applied field strengths. The interaction volume (where the molecular and photon beams overlap) is the resolution-limiting factor, and the VMI technique is designed to minimize the effect of the spatial extension of that volume by applying an electrostatic lens. Like a VMI spectrometer, a reaction microscope collects electrons of all ejection angles by using a magnetic field to contain the high energy electrons within the spectrometer area (Figure 3.4d). To maintain a separation of electrostatic and magnetic field-induced forces (along and perpendicular to the spectrometer axis, respectively), the fields are kept as uniform and aligned as possible, and therefore the use of *lensing* by nonuniform electric fields to reduce the effect of the extended interaction volume complicates the data interpretation[3]. The technique of choice is thus velocity map imaging.

Simulation and optimization Now that we have made a preliminary design choice that allows us to define a simplified version of the spectrometer geometry, we can perform numerical simulations that give insight into the possibilities and eventual compromises involved in an electron velocity map imaging system combined with an ion TOF spectrometer.

Simulations of electron trajectories The performance of the electron spectrometer is judged by the ability to *focus* electrons with similar momenta, but spread in ionization position, to a single impact position at the detector. The relatively high electron kinetic energies we aim to measure cause a large

[3] A magnetostatic field in combination with a non-uniform electrostatic field would not allow us to determine any momentum component unless all three dimensions (X, Y, TOF) are measured, because it causes a coupling of each individual momentum component ($p_{x,y}$ and p_z) with all three measurement quantities (X,Y and TOF).

divergence of the electrons emitted perpendicular to the spectrometer axis (i.e. a large angle of the electron trajectories with respect to the spectrometer axis). This can be reduced by the application of a high electrostatic field strength, or requires a low total spectrometer length. In our design, we aim to keep the detector size and electric potentials of the spectrometer elements and detector at practically feasible levels. This forms a limit to the total spectrometer length to 20-30 centimeter. The combination of a short spectrometer and relatively high electron kinetic energies results in a large angle of electron trajectories with respect to the spectrometer axis. In terms of regular optics, we can state that the paraxial ray approximation does not hold, which can cause *aberrations* in the electron focusing.

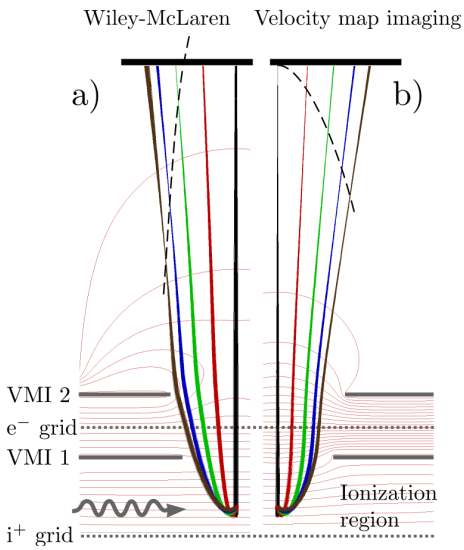

Figure 3.2: Simulated electron trajectories at 100 eV kinetic energy, with different emission directions, and a gaussian-broadened source position. The dashed black lines show the curved focal plane. The electrostatic field contour lines are shown by thin red lines.

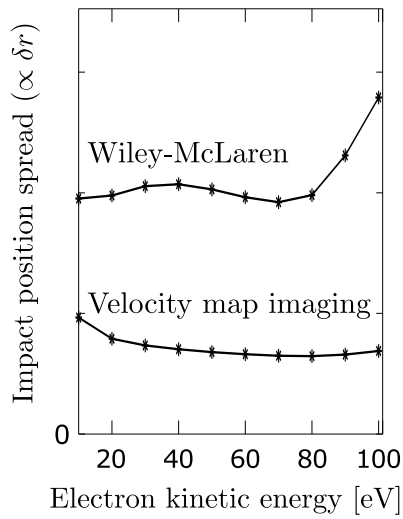

Figure 3.3: The minimized spread of the electron impact position (or loss function) of the two operation modes.

In the simulations, we have quantified the ability to focus electrons with similar momenta in a so-called *loss function*; a value determined by summing up the standard deviations of impact positions of electrons at different mo-

menta and energy. The loss function allows an easy estimation of the performance of the spectrometer and can be used to optimize the electric potentials of the spectrometer elements for the best performance at a specified geometry. This geometry is chosen such that different imaging strategies can be employed, as will be discussed later. In a typical optimization of the lens potentials, we model the source extension as nine source points distributed in a two-dimensional grid of 3·3 mm^2 size and 1·1 mm^2 spacing, located around the source center[4]. We run five trajectories per source point, with each a different angle of emission relative to the spectrometer axis. The loss function is defined by the radial spread of these 45 (9×5) trajectories, at each angle of emission, and we aim to minimise that value. The limited amount of sampling positions used here give only an approximation of the real resolution, but provide a means to find the optimal field configuration. The loss function is analogous to the resolving power, as discussed in **paper VII**. We have used a global minimum algorithm to find the lowest value for the loss function and the corresponding potentials of the spectrometer elements (grids and lenses, indicated as grey lines (lenses) or dotted lines (grids) in Figure 3.2).

Figure 3.2 shows the chosen geometry and examples of simulated electron trajectories. Note that these trajectories are calculated in the same spectrometer geometry, but with different constraints on the spectrometer elements. In the Wiley-McLaren configuration (left), the electrostatic field in the ionization region needs to remain uniform, while in the Velocity map imaging configuration (right), the potential of the electron grid is held at the average potential of lens VMI 1 and VMI 2, such that the grid does not influence the electric field profile. The dashed black lines represent the *focal plane*, as it would be defined in optics. The focal plane is curved (shorter focal length for larger emission angles), causing some emission angles to be *out of focus*. In optics, this is referred to as Petzval field curvature [138]. The focal plane curvature is lower (more parallel to the detector plane) in the case of the Wiley McLaren condition, resulting in a more even focus at the detector plane.

Figure 3.3 shows the minimized impact position spread (representing the overall position spread, chosen as the loss function) at different electron kinetic energies and the two different operation modes. The electron spread is larger in the Wiley-McLaren configuration, at all energies considered, as an effect of the Petzval field curvature discussed earlier. The electron energy resolution of the VMI configuration is about a factor two better than that of the Wiley-McLaren configuration, advocating for the measurement in the VMI

[4]We only consider a source extension in two dimensions, by assuming cylindrical symmetry around the spectrometer axis

configuration when electron momentum resolution is of highest priority.

Simulations of ion trajectories Combining the design criteria of both the ion and electron spectrometer, the ideal spectrometer setup would combine velocity map imaging with ion momentum imaging, fulfilling Wiley-McLaren conditions. However, velocity map imaging requires a non-uniform electrostatic field inside the ionization region (see Figure 3.2b). The effect of the non-uniformity of the electrostatic field around the ionization point on the ion momentum imaging is complicated to understand from general principles, and the following numerical simulations visualize the anticipated consequences on the ion momentum imaging.

The simulations shown in Figure 3.4 display the ion momentum imaging in a uniform (WM, left) or non-uniform (VMI, right) electrostatic field. In the electron velocity map imaging configuration, the field strength at the centre of the ionization is chosen such that the Wiley-McLaren condition is held locally. We can observe that the additional broadening depends on the

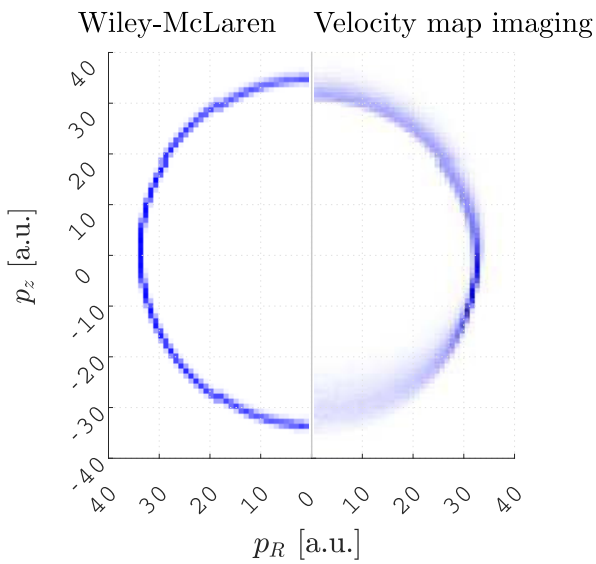

Figure 3.4: Simulations of ion trajectories where the Wiley-McLaren focusing is fulfilled (left), or the spectrometer is operated for optimum electron momentum imaging (right). The impact position of 1 million protons were calculated, with isotropically distributed momenta and a Gaussian distributed kinetic energy at 10 eV (σ = 0.1 eV). The histogram shows the volume density of momenta as calculated from the measurement position.

emission direction; if emission is at a right angle with the spectrometer axis, the broadening remains almost the same. However, the VMI-configuration causes significant momentum broadening when particles are emitted towards ($p_z > 0$) or away from ($p_z < 0$) the detector. This is thus the compromise in velocity map imaging of the electrons: the instrumental broadening of the ion momentum measurement increases for forward and backward emitted ions. It must be noted that the test case employed here represents an extreme case of a low mass (H^+) with high kinetic energy (around 10 eV), where the effects of the field uniformity are strongest.

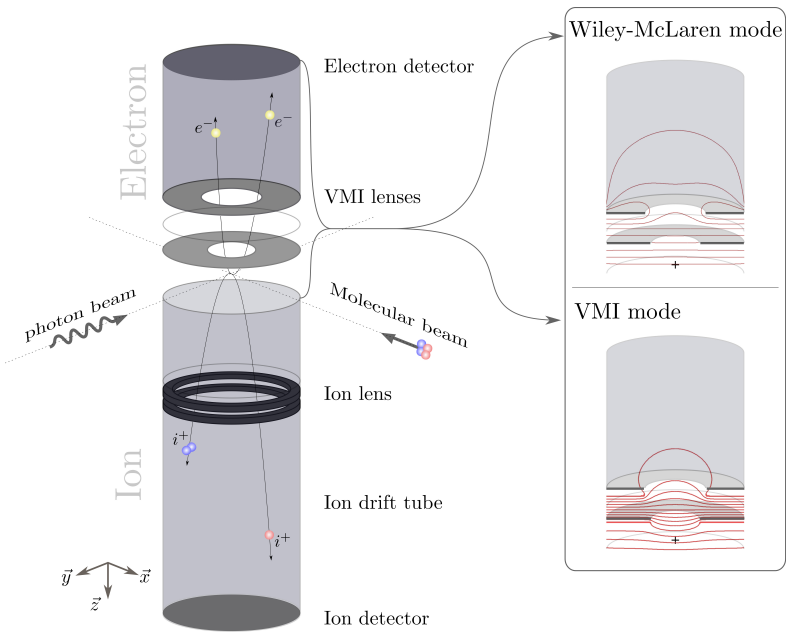

Figure 3.5: Schematic of the Ion-Electron momentum imaging spectrometer developed in this work. The arrangement of metal meshes (or grids) and lenses allows an easy swapping between a mode where the electron momenta are focused well ('VMI mode') or where the ion TOF space focusing is prioritized ('Wiley McLaren mode'). Insets show the electrostatic contour lines of the Wiley-McLaren (top) and VMI (bottom) operation mode. The plusses indicate the center of the interaction region.

Operation modes Summing up the conclusions obtained from the simulations shown above, we choose to define two different modes of operation: (i) a velocity map imaging mode, where the electron momentum imaging is

optimized, and the resolution of the ion p_z measurement is compromised, and (ii) a Wiley-McLaren mode, where the Wiley McLaren condition is fulfilled, optimized for ion 3D momentum measurements, but compromising the 2D electron momentum measurement. A schematic representation of the conceptual design showing both the ion and electron spectrometer, with the two different operation modes is visualized in Figure 3.5.

Final design We will now briefly discuss the practical design of the spectrometer, and the decisions made based on the operation requirements. A detailed view of the spectrometer is shown in Figure 3.6. First of all, the design should make it easy to switch between measurement modes, without the need to vent the vacuum chamber that hosts the spectrometer. This is achieved by refraining from in-vacuum resistors, but rather allowing the independent control of the electric potential of the lenses and grids from outside the vacuum chamber[5].

The elements of the spectrometer - the lenses, drift tubes and grids - are all mounted on top of each other, held by four common rods. This design allows an easy change of the geometry, e.g. by adding/removing an element or swapping the order of stacking. The mounting rods are positioned away from the centre to prevent static charging of the rods which would influence the electrostatic field inside the spectrometer [6]. Additionally, the electron spectrometer is shielded from stray electrons by the electron drift tube, instead of using flat and open electrodes. This tube is built in two sections, enabling to apply an Einzel-like lensing in the future.

The four rods that hold all spectrometer elements are mounted on a common ring. The ring is suspended in the vacuum chamber by a positioning system that allows easy alignment of the spectrometer (shown in red in Figure 3.6a). The positioning system is designed to ease three types of movements; vertical and horizontal translation, and rotation around the photon beam.

As mentioned above, electron trajectories are very sensitive to the magnetic field. The local magnetic field in the spectrometer during an experiment

[5]The switching between operation modes is done with two sets of adjustable resistors (potentiometers, one for VMI mode, one for WM mode) which can easily be swapped, such that only the relevant lenses and/or grid potentials are actively controlled, and the others follow passively.

[6]The electrostatic field is modeled by the Laplace equation. The depth of field penetration due to a different potential (V_{ext}) at the edge of two equi-potential parallel plates (held at V_{plates} and separated by height h) into the electrostatic field between those plates can be estimated by $d = \sqrt{\frac{1-C}{C}}\frac{h}{2}$, where C = $\frac{V_{test}-V_{plates}}{V_{ext}-V_{plates}}$ is the relative change of potential (e.g., 5 percent $\rightarrow C = 0.05$).

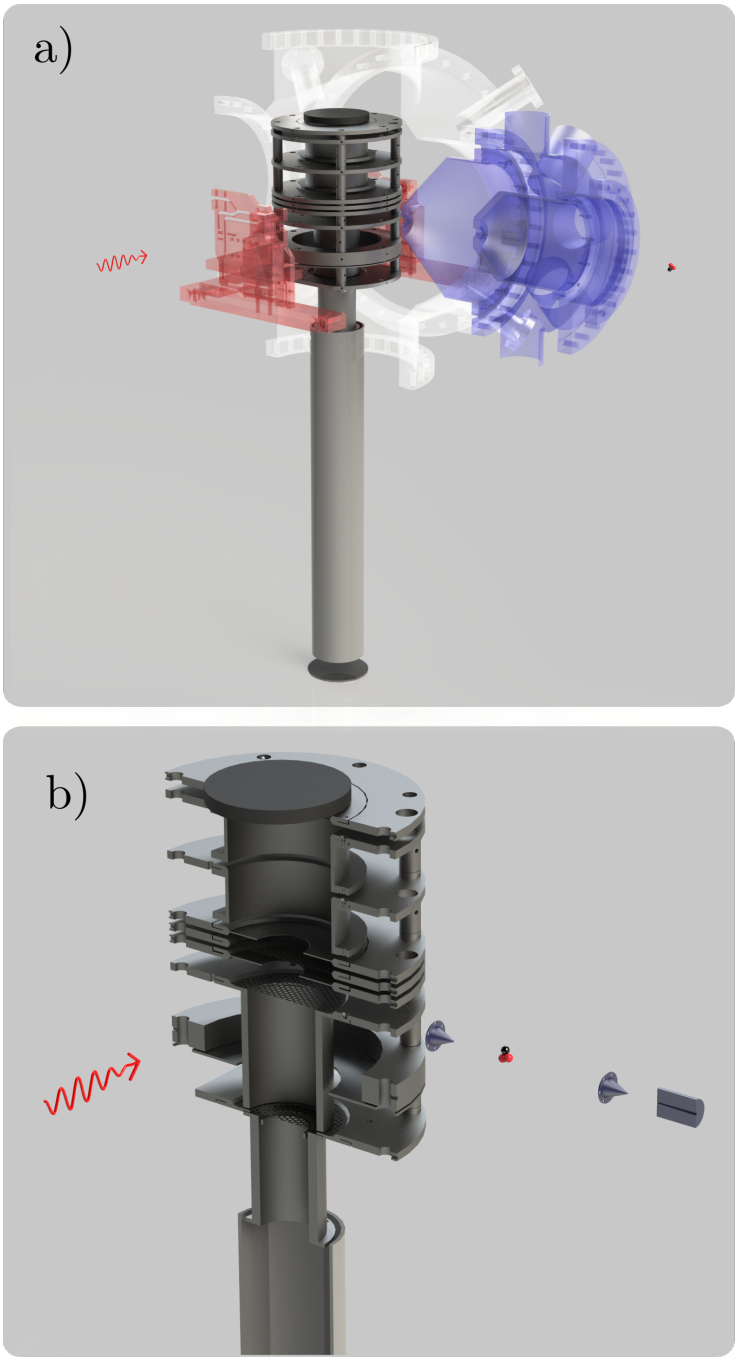

Figure 3.6: a) The main components of the newly designed spectrometer. The spectrometer (grey) is suspended in a vacuum chamber (white) by a positioning system (red). The molecular beam is supplied through two differential pumping stages, separated by beam skimmers (blue). b) A zoom view of the lenses and grids inside the spectrometer.

can be influenced by many factors (Earth's magnetic field, nearby equipment such as ion pumps, etcetera), and could therefore affect the electron trajectory in an unpredictable manner. The spectrometer is therefore covered by a so-called *mu-metal* shield; a tube made from material with low electromagnetic permeability, effectively shielding the electron spectrometer from disturbances in magnetic fields from the outside.

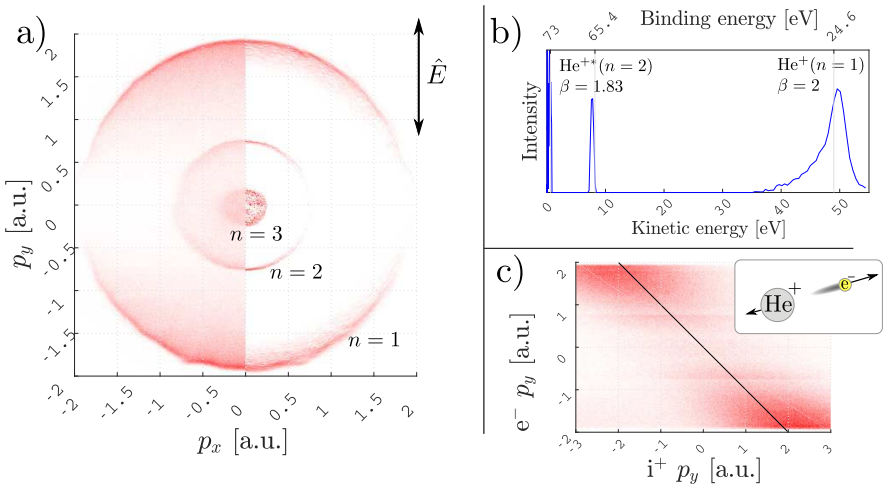

Figure 3.7: Atomic helium photoelectron spectrum upon photoionization at 73.6 eV, measured in 'VMI-mode'. The momentum image (a, left) with the light polarization vector ($\hat{E}$) as indicated, is calculated from the measured impact positions by assuming a constant transverse electron velocity. This image is Abel-inverted (a, right) to yield a radial intensity image [139]. The kinetic energy histogram is calculated by radially integrating the inverted Abel image (b), and compared to the known binding energies of the helium electronic states. In (c), the electron and ion (He^+) momenta in y-direction (in detector plane) show an anti-correlation, due to the ion recoil (see inset).

3.1.2 Characterization

As a means of characterizing the performance of the electron spectrometer, we have measured the well-known response of helium atoms to photoionization (e.g. [140–142]). In Figure 3.7a, the observed photoelectron spectrum is shown (left), along with the Abel-inverted image (right). At a photon energy of 73.6 eV, the helium ion's final state can be the ground state (largest circle in Figure 3.7a), or an electronically excited state with n=2 (smaller circle) or even n=3

(centre). The conversion to momentum is performed by assuming a constant transverse velocity (perpendicular to the spectrometer axis) of the electron.

The Abel-inverted intensity image (the right half in Figure 3.7a) is calculated by assuming cylindrical symmetry along the polarization vector [139]. From this intensity profile, the kinetic energy is then calculated by integrating the radial profile over all angles (Figure 3.7b). The measured kinetic energies span from zero (impact at detector centre) to a maximum greater than 50 eV, at a resolving power ($\frac{E}{\delta E}$) greater than 8, calculated from the FWHM of the $n = 1$ peak. The calculated binding energies (as seen in Figure 3.7b) deviate slightly from the published helium binding energies [143]. In section 4.3, we discuss corrections to this first order assumption in order to enhance the accuracy of converting measured positions to momenta.

The advantage of the simultaneous detection of correlated ions and electrons is demonstrated by the measurement of the helium ion *recoil* due to the electron emission in Figure 3.7c; the momentum of the electron results in the opposite momentum in the helium ion, as observed in the anti-correlation of the ion and electron momenta in y direction (along the polarization vector).

The momentum distribution of electrons in terms of angle of emission upon photoabsorption can be characterized by the anisotropy parameter β[7], ranging from 2 (ejection dominantly along the polarization) to -1 (ejection dominantly perpendicular to the polarization). The β value of the measured distributions can easily be determined from the Abel-inverted radial intensity distribution. The one-electron ionization (n=1) indeed yields a distribution of $\beta = 2$, as expected [146].

3.1.3 Future outlook

The electron-ion momentum imaging spectrometer has been successfully designed and built. The spectrometer detects ions and electrons with high collection efficiencies, optimized for the measurement of electron and ion correlations. The combination of measuring electron momenta and high ion mass resolution makes it possible to correlate the electronic processes (imprinted in the electron momentum) in complex molecules and clusters to their dissocia-

[7]The anisotropy parameter β is defined as [144, 145]:

$$\frac{d\sigma}{d\Omega} = \frac{\sigma_{total}}{4\pi} \left(1 + \beta P_2 \left(\cos\Theta\right)\right), \tag{3.1}$$

where $\frac{d\sigma}{d\Omega}$ represents the angle-dependent cross section, σ_{total} the total cross section, P_2 the second Legendre polynomial, and Θ the angle of the ejection angle with respect to the polarization.

tion products and their momenta. We provide here a brief outlook of possible spectrometer extensions or improvements.

Electron momentum resolution The peak width of the ground state helium photoelectron spectrum (Figure 3.7b) is 3.7 eV (FWHM) at 50 eV kinetic energy. This peak width is largely due to experimental broadening, which is likely a consequence of the focal plane curvature (*Petzval*). This effect could be reduced by the use of the electron drift tube as a simple Einzel lens (as demonstrated in [147]), or by increasing the effective drift length. However, without further changes, the increase of the drift tube length would result in a decrease in the maximum electron kinetic energy that can be measured.

Transmission of higher electron energies We have tested the spectrometer transmission for electrons up to an energy of 50 eV. The detection of higher kinetic energy electrons can be achieved by a higher field strength. Care must be taken to keep the electrostatic field configuration as close to the Wiley-McLaren conditions as possible, to ensure a high ion mass resolution. The detection of high kinetic energy electrons could also be facilitated by a static magnetic field, containing the electrons within the detector area. The magnetic field can be applied in the aforementioned Wiley McLaren detection mode, where the electrostatic field is kept uniform. The restriction to uniform electrostatic fields prohibits the use of electron focusing optics, and makes the size of the interaction volume the resolution-limiting factor. This smearing effect from the interaction volume can be reduced *a posteori* in the data treatment, by calculating the ionization position from the ion detection and applying that shift to the measured electron detection. This can only be done in a coincidence-type of acquisition, described in section 4.4. As an estimate, to detect an electron with a kinetic energy of about 300 eV, a magnetic field strength of around 30 Gauss is needed to complete half a magnetic node (as defined in [148]). When magnetic fields are applied externally along the spectrometer axis, the μ-magnetic shield (cylindrically symmetric around the spectrometer axis) may function as a guide to align the magnetic field lines along the spectrometer axis, but to verify the actual effect we need to perform further investigations.

Electron Time of Flight The electron spectrometer will operate at the new synchrotron facility MAX-IV in Lund, and in our home lab using a helium discharge lamp for characterization purposes. During normal operation (multi-bunch mode) at MAX-IV, the time between pulses is short (10 ns)

and the pulse length is relatively long (up to 200 picoseconds [149]), with unknown jitter between light pulses. This introduces an uncertainty in the determination of the ionization time of a measured particle. This uncertainty is caused in the first place by the fact that the time of flight of the particle is often much longer than the light pulse separation time. Secondly, the ultimate accuracy of the time of flight measurement is limited by the pulse duration time[8]. The rather high field strength applied in the electron spectrometer (about 300 V/cm) will result in an electron time of flight of the same order of magnitude as the light pulse separation (e-TOF$\sim$3-4 ns), and the spread in electron time of flight will be smaller than the pulse separation time. Hence, the measurement of an electron time of flight is, in principle, possible by the correlation of measuremt times to light pulse arrival times. In this measurement mode, the light pulse duration will impose a time resolution limit, but can nonetheless be a first step to the measurement of the three-dimensional momentum vector of electrons, and consequently their kinetic energy. For example, this would enable the measurement of molecular frame photoelectron angular distributions (MFPAD, e.g. [150, 151]).

If both the magnetostatic field and electron time of flight scheme are applied, we can define a third operation mode, similar to a reaction microscope. The Wiley-McLaren condition can still be fullfilled, making it suitable for the study of high energy electrons and heavier ionic species (e.g. clusters) due to the high ion mass resolution.

[8]The typical detection time resolution in our experiments is 100-150 ps, see section 4.1

3.2 Light sources

In this thesis, we study the dynamics induced by photoionization, mainly in systems with low-mass elements such as carbon, nitrogen or oxygen. The binding energy of the core-shell electrons of these elements requires a few hundred electronvolt ($\approx$ 300-600 eV) in energy, and can be achieved by soft X-ray photons. We want to select the ionization site, which implies the use of photons with energies near the core orbital binding energies where the ionization cross section of that core orbital is high. A precisely tunable photon energy thus allows element-specific core shell ionization. A narrow spectral width (monochromatic light) also allows the identification and selection of chemically-shifted sites (with a shift in the order of a few eV or less) in a molecule or cluster (e.g. [152] and **Paper I**) or the resonant excitation to high-energy electronic orbitals (e.g. [27, 28, 153, 154] and **Paper II**). Additionally, it allows the precise measurement of ionization energies (**Paper IV**).

There are currently several advanced light sources available that enable research in atomic and molecular physics. Synchrotron radiation facilities deliver tunable photon energies, from visible light to hard X-rays. Recently, X-ray Free Electron Lasers (FELs) have been developed [155], that generate light pulses of femtosecond duration. Lastly, extreme ultraviolet light sources based on High Harmonic Generation (HHG) create ultra-short light pulses (attosecond duration), have a high spatial coherence [156], and a wavelength range that can reach into the X-ray spectral region. The ultra-short and coherent nature of FEL and HHG light pulses has made many new time-resolved studies possible.

Synchrotron radiation facilities offer unparalleled energy tunability of a monochromatic light source in the soft X-ray regime, and the majority of the research presented in this thesis has therefore been performed using synchrotron radiation sources. This section will briefly present the history and physical concepts behind synchrotron radiation. The latter part of this section briefly introduces the working principles of FELs.

Synchrotron radiation The first systematic study of X-rays was conducted by Wilhelm Röntgen [157], using a high-voltage discharge tube. The polychromatic X-ray beams produced in these tubes are produced by the acceleration of charged particles (*bremsstrahlung*). In the case of synchrotron radiation, the acceleration is perpendicular to the longitudinal relativistic velocity of the particle [158, 159]. The radiation intensity increases with the electron energy, so more synchrotron radiation is emitted at high particle speeds, such as those used in particle accelerators. In the first particle accel-

erators, the emission of radiation at the *bending* of charged particle beams was seen as an annoying loss of kinetic energy. Starting from the early 1960's, the unique properties of synchrotron radiation were recognized [160] and electron accelerators were built that exploited synchrotron radiation as a light source. First, using *bending magnets* at the corners of the accelerator, and later using *undulators*; dedicated magnetic devices designed to produce intense and collimated light beams.

Components of a storage ring The main elements of a modern facility that produces synchrotron radiation are shown schematically in Figure 3.8a. The free electrons are supplied by a cathode, and accelerated to relativistic energies in a linear accelerator (LINAC) forming so-called *electron bunches*. These bunches are then steered into the storage ring, where magnetic bending sections force the bunches to circulate. The bending sections and undulators cause the electrons to emit synchrotron radiation, resulting in a loss of electron kinetic energy. To compensate for the lost energy, the electron beam travels through an externally applied Radio-Frequency (RF) electromagnetic field in cavities. In these cavities, standing waves are formed, synchronized with the electron bunches, such that the (slower) electrons experience an acceleration due to the (RF) electric field, replenishing the kinetic energy.

Undulators Modern storage ring facilities create radiation mainly by magnetic insertion devices such as undulators. When electrons propagate through an undulator, they are periodically forced to move in transverse directions by means of oscillating magnetic fields, resulting in the forward emission of synchrotron radiation (see Figure 3.8b). Each cone of emitted radiation has a broad energy range, but the constructive interference of radiation from each magnet pair results in narrow spectral bands of radiation (harmonics). The fundamental radiation wavelength can be calculated by the so-called undulator equation [161]:

$$\lambda = \frac{\lambda_u}{2\gamma^2}\left(1 + \frac{K^2}{2}\right), \qquad K = B_u \lambda_u \frac{e}{2\pi m_e c_0} \tag{3.2}$$

Here, λ is the principal wavelength, the undulator period is denoted λ_u (typically 60 mm) and γ is the Lorentz factor (approximately $6{\cdot}10^3$ at the 3GeV MAX-IV synchrotron [162]). The constants e, m_e and c_0 are the elementary charge, electron rest mass, and speed of light, respectively. The undulator parameter K depends on the product of magnetic field strength and undulator

period. Note that the wavelength of constructive interference can be shifted by tuning K, in practice by changing the magnetic field strength (B_u) in the undulator[1].

Free electron laser Free Electron Lasers (FELs) in the Vacuum-UV (VUV) and X-ray regime are sometimes referred to as the latest generation of synchrotrons. As in the case of a conventional synchrotron, electrons in an FEL are accelerated to relativistic speeds, and emit radiation in an undulator. An FEL typically consists of multiple undulators that contain more undulating periods than those used in a synchrotron. The higher number of undulations gives electron bunches time to not only emit but also amplify radiation after the development of so-called *microbunches*, see Figure 3.8c. The emitted electromagnetic radiation from the first undulations, propagating along the electron bunch beam, creates a transverse magnetic field. The transverse motion of the electrons in this magnetic field causes the electrons to experience a (longitudinal) Lorenz force, dividing the macro-bunch into slices, with a spacing corresponding to the radiation wavelength. After this separation, the wave emission from each microbunch is correlated. The correlated emission is an efficient amplification of the radiation field, generating a high intensity light pulse[2].

Beamlines The light beam produced by the undulator is prepared for the use in experiments through optical elements in a *beamline*; for example by a monochromator to select light in a narrow photon band width in one of the high intensity harmonics, resulting in a monochromatic light source. In this work, experiments have been conducted at the French national synchrotron facility SOLEIL at beamline PLEIADES in **Paper I** [167, 168]; at the Swedish synchrotron laboratory MAX-Lab at beamline I411 at MAX-II in **Paper II, V** and **VI**; at the I3 beamline at MAX-III in **Paper IV** (now MAX-IV [162]); and at the X-ray FEL FLASH in Hamburg in **Paper III** [169]. Typical parameters of the light at beamlines at these sources can be found in Table 3.1.

[1] More information on synchrotron radiation and beamlines can be found in [163].

[2] More information on free electron lasers and a comparison to synchrotron radiation light sources can be found in [164, 165] and [166], respectively.

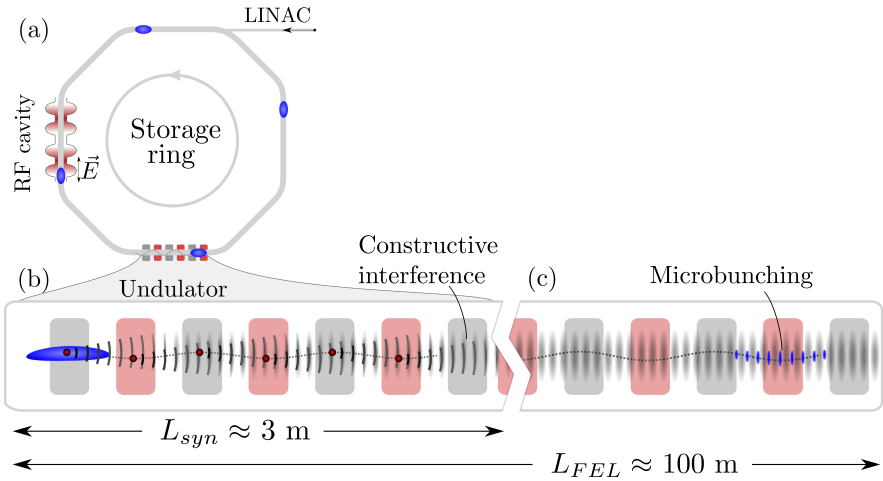

Figure 3.8: Schematic representation of the key components of a storage ring (a) and undulator (b). Charged particles (electrons) are emitted in bunches from a cathode and linearly accelerated (LINAC) into the storage ring. At each undulator, the electron bunches (blue) are accelerated in the transverse direction, and emit synchrotron radiation around their acceleration maxima (red), (b). In Free Electron Lasers, the electrons are sent directly from the LINAC to the undulator. The longer undulator(s) (c) allow interference of the radiation from previous undulation pulses, creating a harmonic energy spectrum. The Lorenz force induced by the radiation influences the relative positioning of the electrons in the bunches and causes microbunching within a bunch, an important feature in the amplification of radiation in FELs.

Table 3.1: Typical parameters for the light sources used in this work.

Facility Beamline	MAX-II [162] I411 [170]	SOLEIL [167] PLEIADES [168]	FLASH [169] -
Photon energy (eV)	5-1000	10-1000	30-200
Resolving power	10^4	10^5	10^2
Pulse duration (s)	10^{-10}	10^{-11}	10^{-15}
Photons per pulse	10^4	10^4	10^{12}
Peak flux (photons/s)	10^{14}	10^{15}	10^{27}

3.3 Molecular and cluster beam

The light beam interacts with the sample in the spectrometer. The sample is traditionally supplied by effusive jets [171], employing a thin needle through which the sample flows. The sample exits the needle close to the light beam, where a high sample density is delivered. The use of an effusive jet can however lead to a large photon-sample interaction volume, due to the large divergence of the sample beam leaving the needle. An increase of interaction volume decreases the spectrometer resolution. In addition, the effusive jet does not cool the molecules in the sample, so the production of free clusters by condensation is not possible when using the effusive jet. The use of a so-called molecular beam, which is produced via supersonic expansion of a gas into vacuum, can yield a narrow and cool sample beam. The cooling can be so severe that condensation of atoms/molecules to atomic/molecular clusters occurs. The molecular beam usually consists of a nozzle through which the sample flows and cools, and subsequent skimming of the produced jet selects the coolest part of the beam. Most studies in this work make use of molecular beams, and this section will therefore explain the production of such a beam, followed by a brief description of the condensation of the sample to form clusters[1].

Nozzle flow The flow through a nozzle is driven by the pressure difference between the ends of the nozzle. At a pressure ratio larger than two ($\gtrapprox 1.89$), the flow becomes supersonic, i.e. the fluid velocity surpasses the local sound velocity in some parts of the flow. The ratio of local velocity to sound velocity is called the *Mach number* (M, supersonic flow $\rightarrow M > 1.3$). Under our operating conditions, the pressure difference is so large that a supersonic flow can exist outside of the nozzle (an *under-expanded jet*). An example of such a jet can be seen in Figure 3.9a. In the so-called *zone of silence*, the flow remains isentropic and laminar, and is therefore the zone from which one wishes to extract the molecular beam. It was empirically found [174] that the spatial extension of the zone of silence beyond the nozzle exit can be described as:

$$L_{\mathrm{ZOS}} = D \cdot \frac{2}{3}\sqrt{\frac{p_0}{p_b}} \tag{3.3}$$

where the nozzle diameter D (e.g. 150 μm), the pressure before the nozzle p_0 (e.g. 1 bar), and the pressure after the nozzle p_b (e.g. 10^{-5} bar), can estimate the zone of silence length L_{ZOS} (e.g. ≈ 4.7 cm).

[1] This section is largely based on information found in dedicated books about molecular beam flows [172, 173], and the reader is directed to those for more information.

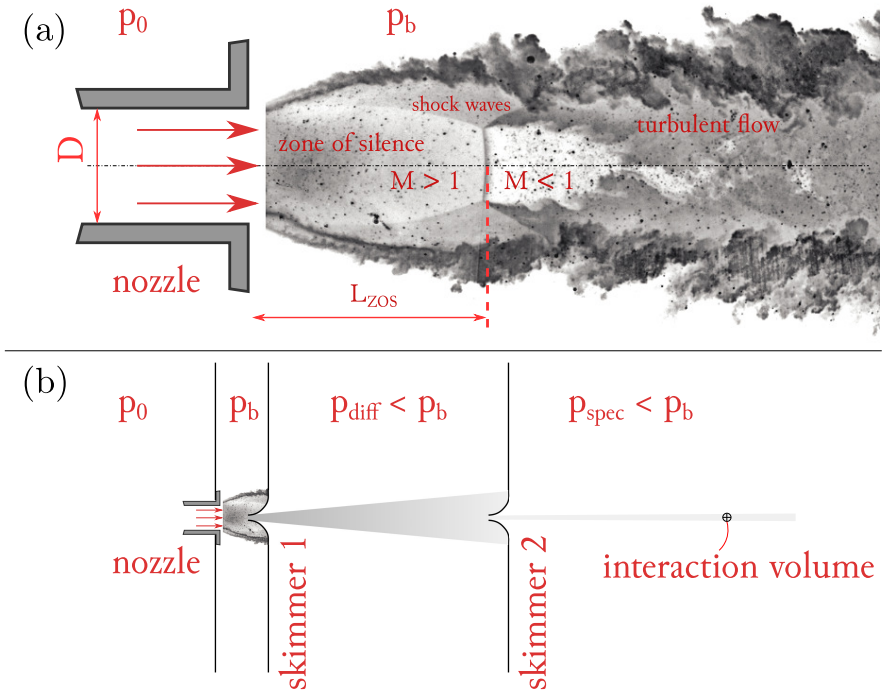

Figure 3.9: (a): Image of a severely under-expanded supersonic jet flow[2]*, imaged by Planar Laser Mie-scattering. Image adapted from [175]. The image shows the key regions in the flow, highlighted in red text. (b): The molecular beam arrangement, including the nozzle and two beam skimmers, resulting in a narrow sample jet that interacts with the photon beam.*

Skimmers The jet emitted by the nozzle travels through apertures (around 0.5-1 mm diameter in our case) through which only the central (coolest and densest) part of the beam travels (see Figure 3.9b). These beam *skimmers* serve two purposes: (i) to decrease the transverse dimensions of the molecular beam, therefore minimizing the interaction volume, and (ii) to form a pressure barrier between the low vacuum nozzle chamber and the high vacuum spectrometer chamber. The first skimmer is placed within the zone of silence, where interaction of the jet with residual gas is minimal. The skimmers are conically shaped to reduce the perturbation of the skimmer on the jet flow.

[2]The nozzle opening and symmetry of the imaged flow (22 mm and planar symmetry) are different from the typical nozzles (150 μ, circular symmetry) used in this work, but the key flow features remain the same.

Condensation The supersonic flow is often assumed to be adiabatic, i.e. the expansion is so fast that the heat exchanged with the environment can be neglected. Adiabatic expansion in the beam causes a high degree of cooling, reducing the internal energy of particles. If the internal energy is decreased to the same order of magnitude of the binding energy between the particles, through Van der Waals interaction or hydrogen bonding, nucleation of particles can occur. Nucleation from a supersonic expansion was first observed in 1956 [176]. The quick expansion (decrease of pressure) and cooling (decrease of temperature) causes an isentropic transformation. The sample phase in the zone of silence can be expressed in thermodynamic terms as a *super saturated* state; the sample is still in gas phase, while the equilibrium phase is liquid or solid under these conditions (see Figure 3.10). From a microscopic perspective, we consider the nucleation mechanism in a series of two-body collisions. The first interaction forms the dimer complex. The dimer collisions can then be grouped: those where the particles agglomerate to clusters (and heat up from the decrease in potential energy), and those where the clusters cool down by transfering heat to particles in the surrounding medium [177]. In the case of larger condensates, cooling can also occur through evaporation of single hot particles from the cluster. Note that a high collision frequency is necessary for the nucleation process to occur, which is facilitated by the high local mass density in the zone of silence.

As a result of the random nature of the condensation process, a large range of cluster sizes is produced. The size distribution can be described by a log-normal distribution, and empirical expressions exist to predict the size distribution of Van der Waals clusters [178, 179] and hydrogen-bonded clusters [103]. Measurement of the size distribution is challenging, due to the low dissociation energy that causes evaporation of molecules upon ionization. The evaporation can be prevented by *doping* the cluster (i.e. adding a particle on the surface of the cluster after condensation) with an atom that is even more weakly bonded than the constituents of the cluster. Upon *soft* ionization (i.e. a photon energy just above the ionization potential of the cluster molecule), the atom evaporates and the evaporation of molecules from the cluster is prevented. An example of such measured size distribution of an ammonia cluster at different stagnation pressures is shown in Figure 3.11.

Molecular beam velocity In the case of measuring heavy ions originating from a molecular beam, the velocity of the neutral molecular beam can result in a drift in detection position as the mass (and thus flight time) increases. An example is shown in Figure 3.12a, where the molecular beam is perpendicular

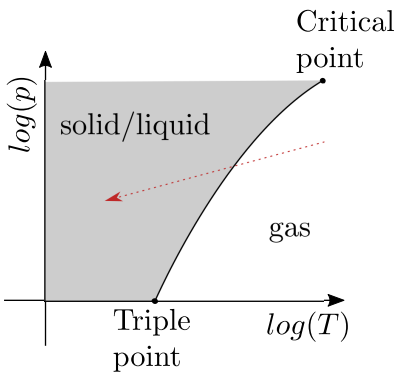

Figure 3.10: Schematic p-T diagram with an illustration of the phase evolution during expansion, where the sample reaches a 'super-saturated' state (red dashed line).

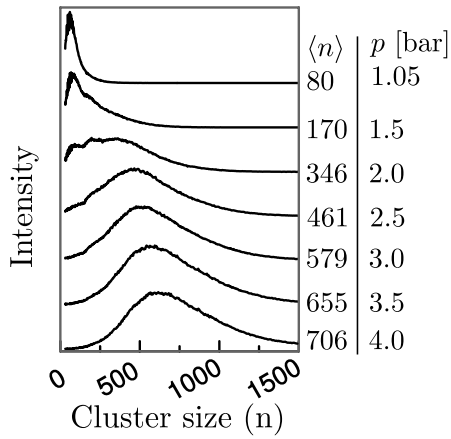

Figure 3.11: Measured ammonia cluster size distribution as a result of adiabatic expansion, at different stagnation pressures, see column left. Nozzle diameter: 76 μm, nozzle half opening angle: 20.1°, nozzle length: 6 mm. Figure adapted from [103].

to the spectrometer plane (in X-direction), yielding a linear shift in the impact position on the detector as the ion flight time increases. Figure 3.12b shows an example of CO_2 and propanol clusters. The position shift of larger propanol clusters is so large that they land on the wall of the spectrometer, rather than on the detector, causing a limit of the maximum measurable cluster size. The limiting cluster size does not impose a restriction in this work, but could be increased for instance by tilting the molecular beam with respect to the spectrometer, such that the beam and spectrometer axes are more aligned [181].

In the data treatment, the velocity of all particles in the sample beam is assumed equal, as is verified by the proportional increase of the X positions and TOF in Figure 3.12b. We can thus define a moving frame of reference, moving at a speed v_{MB}, from which the sample interacts with the photon.

This speed can be expressed as: [173]

$$v_{MB} = \sqrt{\frac{\gamma RT}{M}} \tag{3.4}$$

where γ is the heat capacity ratio, R the gas constant, T the absolute temperature (often assumed equal to the nozzle temperature) and M the molar mass. Some typical sample velocities, estimated from the TOF-X measurements, and the corresponding nozzle temperatures are listed in the table inset in Figure 3.12c.

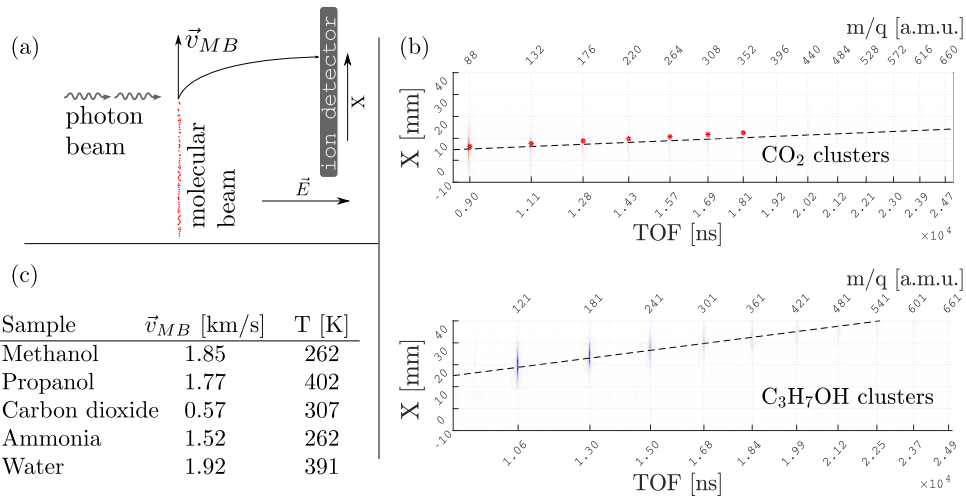

(c)

Sample	$\vec{v}_{MB}$ [km/s]	T [K]
Methanol	1.85	262
Propanol	1.77	402
Carbon dioxide	0.57	307
Ammonia	1.52	262
Water	1.92	391

Figure 3.12: (a): The molecular beam velocity causes a drift of ion position, due to the longitudinal beam velocity (along X, in this case). (b) top: CO_2 clusters at 307 K nozzle temperature. A velocity of 0.57 km/s results in the best correspondence to the measurements (black dashed line). As a reference, we show dedicated cluster beam velocity measurements in red asterisks [180], with a higher nozzle temperature (343 K), explaining the higher longitudinal beam velocity. Bottom: Propanol clusters at 402 K: Note how the large propanol clusters fly out of range of the detector (detector radius of 40 mm) and land on the spectrometer wall before reaching the detector. (c): Table of typical velocities of the molecular (cluster) beam measured in our spectrometer for different samples and nozzle temperatures.

Chapter 4

Data acquisition and treatment

In the previous chapter, the goal and design of different spectrometers have been described. Here we will present how we acquire and subsequently treat data obtained with such instruments. The spectrometers used in this study steer oppositely charged particles towards different detectors, allowing us to collect data from multiple detectors simultaneously. In the work presented in this thesis, we mostly use position sensitive detectors that can detect the impact time and position of single electrons or ions at a time, at a high rate (up to MHz). The basic working mechanism of these detectors is briefly explained in the first section. The detectors can inform us on the incident particle's time and position. These physical quantities are usually not of direct interest, but are instead converted to properties that are physically interpretable, such as mass, linear momentum and energy. The conversion to these physical quantities is presented in section 4.2. Additionally, we are often interested in the correlation between observations on the same detector, or even between detectors. There are two schemes of acquisition presented in section 4.4, the so-called *coincidence* and *co-variance* technique. In section 4.5, we discuss the possiblities to *filter* data in order to select only the part of a measurement that is of interest.

4.1 Detection

To study the fragmentation processes of single molecules or clusters, we detect the charged fragments that result from it. The particle is detected by the amplification of a charged particle to many electrons in a Multi-Channel Plate (MCP). The plate can thus create a cloud of free electrons initiated by

the impact of one particle, and the depletion of electrons in the plate yields a small but measurable electrical pulse. The position of the charged particle is measured by a Delay-Line Detector (DLD) or a phosphor screen. In this section, we will present the amplification and position measurement techniques used in delay line detectors and briefly describe how the detector information is stored to a digital file.

Signal amplification The amplification of single incident particles to more electrons relies on secondary emission: the impact causes one or more electrons to be ejected from the (low work function[1]) surface. A local electrical field accelerates the electrons towards another spot on the surface, whose impact in turn yields even more free electrons. The electron avalanche is similar to the workings of a photomultiplier tube or channel electron multiplier, and occurs in a single microscopic channel ($D \approx 20\mu$m) of a so-called Multi-Channel Plate (see Figure 4.1, top right). The avalanche typically yields a factor $10^3 - 10^4$ increase in the number of avalanche electrons per MCP, and multiple MCPs can be stacked to enhance the signal strength. The collection of electrons (*electron cloud*) leaves the MCP plate at the side opposite the input face (see Figure 4.1, top right). All electrons released by the MCP together cause a measurable decrease in electron density in the plates. This brief electron deficiency can be measured as a pulse in MCP potential, and provides a measure of the detection time. Note that the detection efficiency does not only depend on the impact particle's properties, and the work function of the surface, but also on the area on the detector that consists of channel openings. This property is usually expressed in *Open Area Fraction* (the area related to the total detector opening), and has a typical value of 60%. Recently, detectors with funnelled channel openings have been developed, increasing this fraction to 90% [183]. More information on detection efficiency and a calibration procedure is found in appendix A.

[1] The low work function can be achieved by coating the MCPs input face [182]

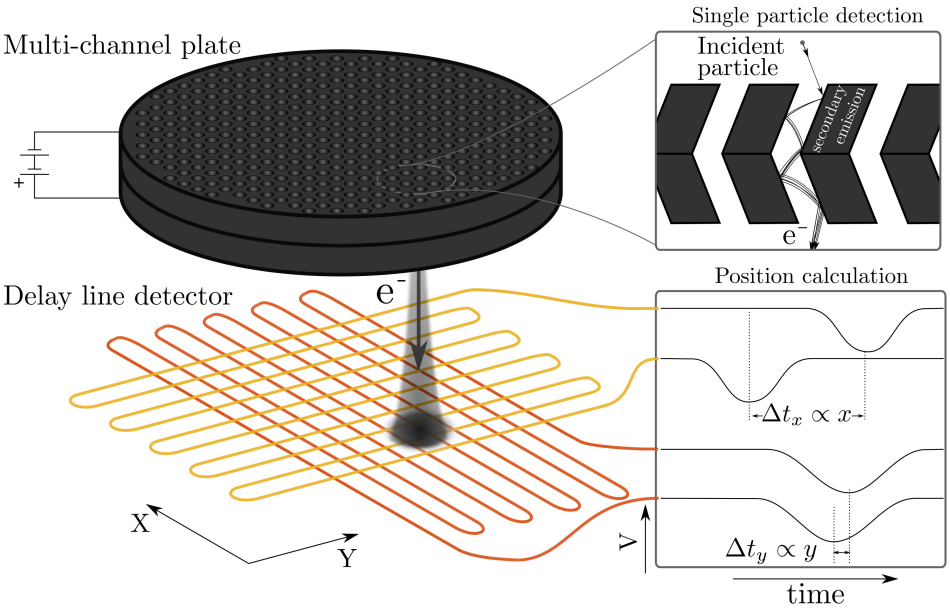

Figure 4.1: The time and position of a single incident particle hitting the detector is determined using a multi-channel plate (top left) and a delay line detector (bottom left). If the incident particle lands inside a channel, and causes secondary emission of electrons, an electron cascade can occur (top inset). This cascade forms an 'electron cloud' that exits the multi-channel plate and is partially absorbed by delay lines. This causes small electric pulses to travel to both sides of the line, and the measured pulse arrival time difference from these ends is proportional to the landing position of the particle (bottom inset).

Position measurement Due to the microscopic channels in the MCP, the X,Y position of the outgoing electron cloud remains very close (μm) to the position of the incident electron. The electron cloud position can be detected by Delay-Line Detectors [184, 185], in which long conducting wires are zig-zagged below the MCP (see Figure 4.1, bottom left). The electron cloud is partially absorbed by the wires, and this causes a measurable pulse in the electric potential in the wires. These pulses propagate in both directions of the wire (*delay line*) and the relative timing of the pulses on either end of the wires is proportional to the position of the electron cloud across the winding direction. With this technique, a large detection area can be spanned, with a spatial resolution that can reach down to a few tens of micrometers (e.g. [186, 187]).

The shortcoming in the delay-line method is the inability to detect the simultaneous impact of multiple particles; the simultaneous impact will cause two peaks closely spaced in time in the delay lines, and make the interpretation of the time and position of those impacts ambiguous. Many detectors can therefore not register two particles within the so-called *dead-time*, typically a few nanoseconds. This problem can partially be solved by a three-layer (HEXagonal, [188]) or Four-Quadrant [189] delay line detector. In the case of the HEX detector, the three delay wire stacks are rotated 120 degrees with respect to one another, yielding position information in three different directions. This redundancy in position measurements enables the reconstruction of most simultaneous impacts of two particles. The Four-quadrant detectors use four delay lines in parallel, enabling the measurements of simultaneous impacts of multiple particles on different quadrants. In this thesis, we have made use of *orthogonal* delay line wires (DLD) and the three-stack delay line wire (HEX) detectors.

Each delay line wire is often accompanied by a second wire (the reference wire). This wire is held at a slightly lower potential, such that more electrons get attracted to and absorbed by the other wire (also called signal wire). The reference wire is a measure of background noise, which can be used to increase the signal-to-noise ratio on the signal wire.

Acquisition method During an experiment, the signals generated by the multi-channel plate(s) and delay line detector(s) have to be acquired and saved to a digital file. A scheme of a possible acquisition setup is shown in Figure 4.2. The first stage of the signal processing is to amplify the pulses coming from the delay lines, increasing the peak height by one to two orders of magnitude. The amplified pulse height should be typically above 50 mV to allow an efficient discrimination against electronic noise.

In our acquisition setup, the discrimination is performed by a constant fraction discriminator (CFD). A CFD converts an analog signal to a logic signal, where the logic signal gives the time at which the peak in the analog signal has reached a certain fraction of the total peak height. This timing from a CFD is independent of the total peak height, making it a more accurate absolute time measurement than discriminating with a constant threshold potential. A typical time resolution of these discriminators is 250 ps [186]. The logic signal is fed to a *Time-to-digital* (TDC) converter, which transmits the data to a PC.

Alternatively, the amplified analog signal from the MCP and delay lines is fed to an *analog-to-digital* (ADC) converter, which discretizes the analog

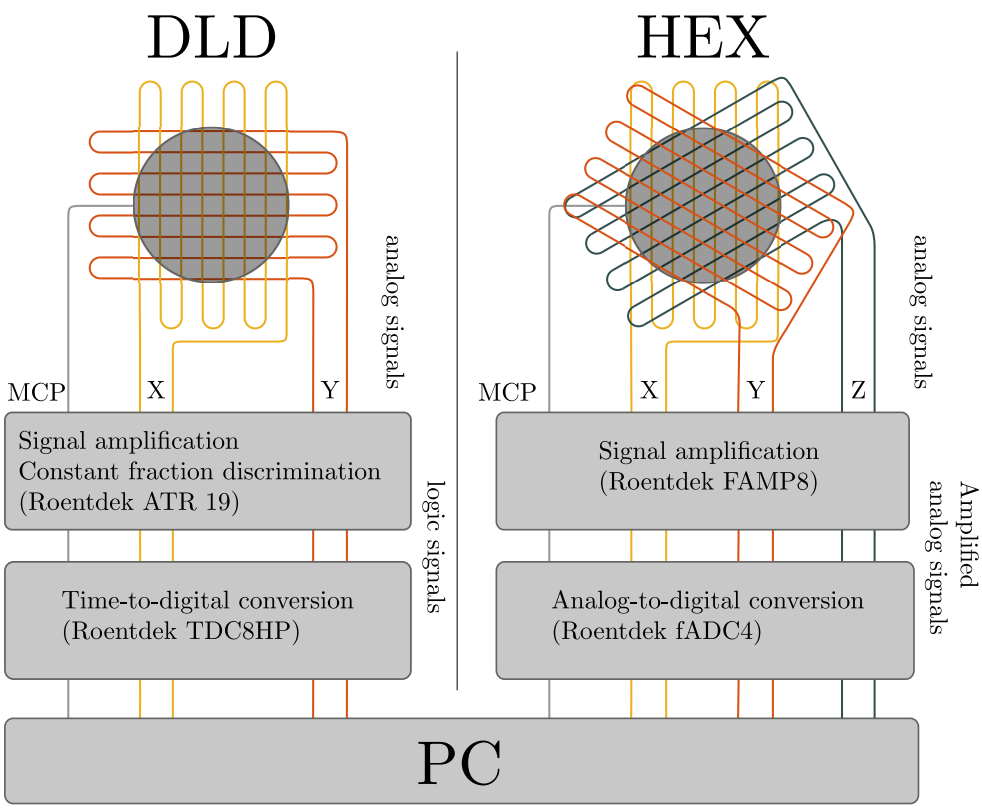

Figure 4.2: An example of an acquisition scheme where two detectors operate simultaneously. The two-stack detector (DLD) is connected to an amplification and Constant Fraction Distiminator (CFD) unit, with outputs connected to Time-to-Digital Converter (TDC) units. The three-stack detector (HEX) signals are amplified and fed to an Analog to Digital Converter (ADC).

signal and transmits this to the PC. This method is more appropriate in the use of three-stack (HEX) delay line detectors, since they allow for advanced peak recognition algorithms to handle simultaneous electron impacts (Note that a CFD would only transmit the peak time of the first of possibly more peaks). The acquisition software in the PC converts these digital signals into timestamps.

In the PC, the absolute timestamps (either directly from the logic signals through a TDC, or converted from the ADC) from each delay line stack are subtracted from each other, and the difference in signal arrival time is used as a measure of position. At the end of the data acquisition, the position and time (X,Y,T) of impact are calculated and stored to a digital file. The typical time resolution of the MCP and DLD timestamps is around 100 picoseconds, and this results in a typical spatial resolution of 50-100 μm [186, 189].

4.2 Conversion

The detector's output is often not directly physically interpretable. In the case of the above described detector, the position and time of impact (X,Y,T) is measured. To translate this information to physically interpretable quantities, we apply manipulations to these *raw* detector outputs. Different spectrometers and detectors require different conversions, and in this section we will present the ones most applied. The coordinate system referred to in the following description and used throughout this section is presented in Figure 4.3.

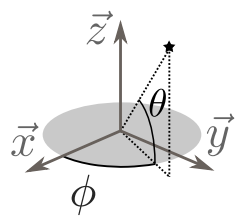

Figure 4.3: The coordinate system used throughout this chapter. The detector planes are parallel to the XY plane.

Mass spectrometry The equations of motion of a charged particle in a uniform electrostatic field dictate the relation between the Time Of Flight (TOF), the mass and the charge of the particle. If we assume that the electric field is aligned along $\vec{z}$ (the spectrometer axis), the particle's trajectory can be calculated by solving the one-dimensional equation of motion, resulting in a predicted TOF from the ionization point to the detector. The following relation can be shown to hold for particles created with no momentum along the spectrometer axis, even for spectrometers with different field strengths along the trajectory: [190]

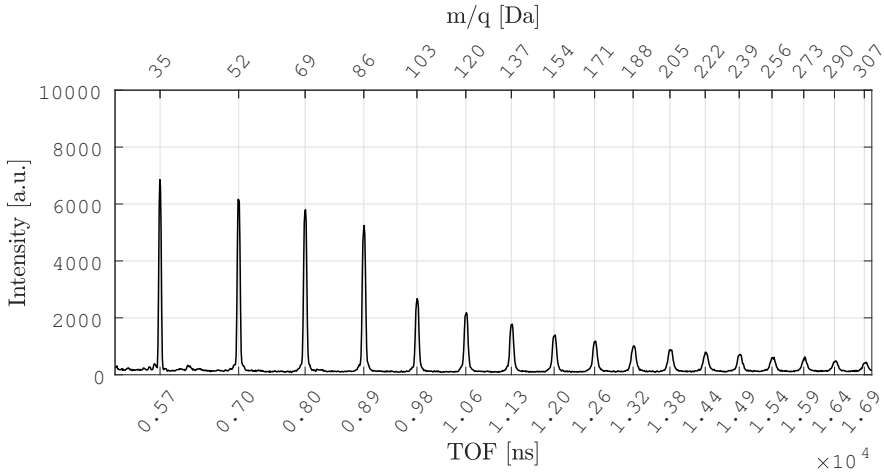

Figure 4.4: An example of a Time Of Flight (TOF) spectrum, with the conversion to mass-to-charge units at the top x-axis. Example: core-ionized ammonia clusters ($h\nu = 420\ eV$)

$$\frac{m}{q} \propto TOF^2 \tag{4.1}$$

where m and q represent the mass and charge of the particle. An example of this relation between the TOF and the mass-to-charge ratio can be seen in Figure 4.4, where a TOF spectrum of ammonia clusters after ionization is shown. The cluster peaks are equally separated in mass by one molecular mass (17 [Da]). Note that the peak-to-peak spacing in TOF is not equal, due to the quadratic dependency given in Equation 4.1.

Momentum imaging The x, y, z-components of the momentum are calculated from the TOF and impact position [190]. The momentum in the z-direction (along the spectrometer axis) is calculated from the TOF of the particle, related to the TOF of a particle with no momentum along the spectrometer axis ($\Delta TOF = TOF_{p=0} - TOF$):

$$\vec{p}_z = q \cdot E_{ER} \cdot \Delta TOF \tag{4.2}$$

where E_{ER} is the field strength in the extraction region, and $\vec{p}_z$ the momentum along the spectrometer axis.

The momentum in the z-direction is thus reflected in the width of peaks in TOF-histograms (such as in 4.4). The momentum in x and y-direction (parallel to detector plane) can be calculated as:

$$\vec{p}_{\{x,y\}} = \frac{m \cdot \{X, Y\}}{TOF} \tag{4.3}$$

where $\vec{p}_{\{x,y\}}$ represents the x, y momentum component, respectively, and $\{X, Y\}$ their positions. This relation assumes a constant velocity of the particle parallel to the detector plane, implying that the electric field vector always points along the spectrometer axis. In practice, an ion spectrometer often uses so-called *lenses*, introducing optical aberrations, as mentioned in section 3.1.1. The aberrations can be corrected in an empirical manner as discussed in section 4.3.

The conversion of X,Y,T data to momentum is an important step in the data analysis, since other physical quantities (such as the kinetic energy) are derived from the momentum. In the analysis of the data shown in this work, we have used a momentum visualization technique that is shown in appendix B, which is implemented in the calibration of the momentum conversion.

Kinetic energy The determination of the momentum in three dimensions allows the calculation of the kinetic energy of the particle upon breakup:

$$KE = \frac{|\vec{p}|^2}{m} \tag{4.4}$$

The linear momenta and kinetic energies of particles from the same ionization event can be compared, exposing many details of the fragmentation process. We will give several examples of the application of this research method in Section 5.

4.3 Aberration correction

In the conversion calculations discussed above, the electrostatic fields in the spectrometer are assumed to be uniform. In reality, the electrostatic field is not perfectly uniform, for instance due to electrostatic lenses used, or imperfections in the charge distribution on the surface of spectrometer elements. The corrections for these ion optics aberrations are presented in this section.

Circular aberration The assumption of uniform electrostatic fields (i.e. $\vec{E} \parallel \vec{z}$) simplifies the conversion equations to linear relations between detected position and momentum components. However, electrostatic lensing

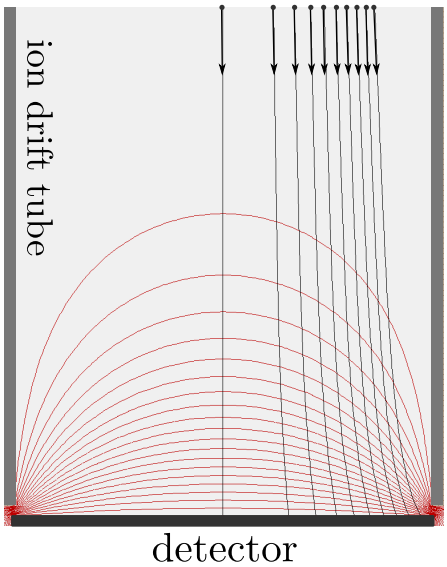

Figure 4.5: Example of an ion optics aberration: the ion trajectories (black lines) near to the ion detector, kept at a different voltage than the ion drift tube (resulting in field contours shown as red lines), change both the ion's time of flight and the radial position at the detector.

can distort this linear relation, and cause a non-linear relation of the measured coordinates to the physical values. The aberration influences the particle's time of flight and position. In the example of an aberration caused by the ion detector (Figure 4.5), the detector is held at a higher voltage, decelerating the ions before detection, increasing the time of flight. Moreover, the difference in voltage causes a *magnifying* effect, such that particles end up at a larger radial distance to the detector centre compared to the situation without a difference in voltage.

An example of a distorted physical distribution is the momentum distribution due to the ion imaging lens and a difference in drift tube voltage and detector voltage. This non-linearity is illustrated in Figure 4.6 (left) for the example of protons from free molecular ammonia. The magnitude of the physical momentum of the proton does not depend on the direction of that momentum, but the measured distribution (Figure 4.6 (left)) does. We will use this to design an appropriate aberration correction.

The non-linearity can be reproduced by SIMION [191] simulations. From those simulations, a mapping of uncorrected to corrected coordinates (TOF, X, Y) is made. This mapping is applied to the experimental data, as shown in Figure 4.6 (right). The transformation reshapes the original angle-dependent momentum distribution to a momentum distribution that shows much less angle-dependence, as expected. In order to increase measurement accuracy, ion optics aberrations should be avoided when possible, for example by operating the detector at the same voltage as the drift tube. However, aberrations

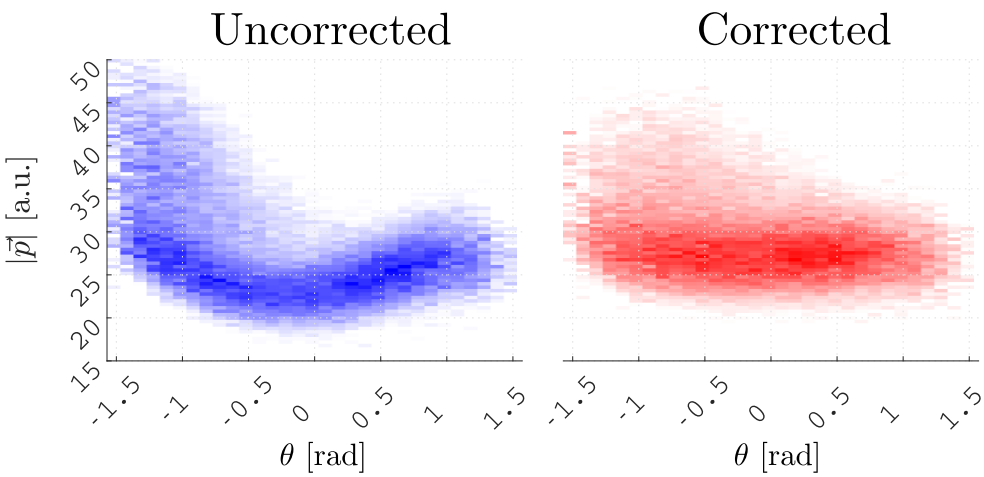

Figure 4.6: Proton (H^+) momentum distribution without correction (left) and with correction (right). The physical momentum norm ($|\vec{p}| = \sqrt{p_x^2 + p_y^2 + p_z^2}$) is invariant to the momentum emission angle (in this case θ), and the histogram should therefore display horizontal features only. Data: C1s photoionization of ammonia molecules.

may be unevitable, and in that case a correction procedure such as the one presented here can help to increase the data accuracy in post-acquisition data treatment. More information on the correction of ion optics aberrations can be found in the description of the software developed in our research group [192].

Non-circular aberration The electrostatic field in the spectrometer can be estimated by numerical means, but the exact field during experiments remains unknown. Non-circularly symmetric patterns can arise in the measured histograms, for example due to non-symmetric distortions of the electrostatic field. This type of aberration is found in different spectrometers, here we present an example observed in the EPICEA spectrometer [122, 193], stationed at SOLEIL, Paris. The toroidal spectrometer detects photoelectrons, and their energy (and thus the detected radial position) should not depend on the azimuthal ejection angle (the angle in the plane parallel to the detector). The detected radial positions of photoelectrons should therefore be invariant to the in-plane ejection angle ϕ, and all non-uniformities are due to experimental artefacts. In Figure 4.7 (left), the directly observed radial position is shown. The lines show radial wiggles, expected to be caused by holders

mounted in the spectrometer that locally change the electrostatic field. The pattern of these wiggles is found by tracing the lines of maximum intensity. Afterwards, these lines of maximum intensity are shifted to the average value of all points of maximum intensity. The radial shift is used to calculate the shift of each measured radial position in the uncorrected data: the linearly interpolated shift between the points of maximum intensity. In the example shown, applying the map results in the histogram shown in Figure 4.7 (right). This procedure is applied to all photoelectrons, and in this case results in an increase in energy resolution approximately 40 percent. More information can be found in the software description [192].

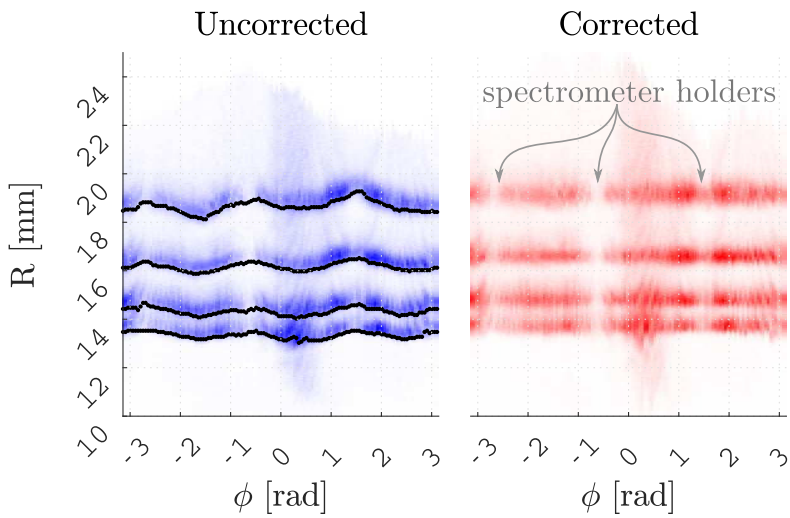

Figure 4.7: Left: Histogram showing the angle-dependent electron radial position from a toroidal energy analyzer, where an angle-independent radial position is expected from physical principles. In this analyzer, the radial position is converted to electron kinetic energy. The non-circular aberration causes the oscillatory pattern, making the radius to electron energy conversion ambiguous. Right: the corrected electron radial position, showing a horizontal stripe pattern, so that a radial position corresponds to an electron energy. The location of the suspected cause of the instability (physical holders in the spectrometer) are indicated in the right plot. Data: photolines upon C1s ionization of ethyl trifluoroacetate ('ESCA molecule') at 411 eV photon energy, as presented in **Paper I**.

4.4 Correlation

In the previous sections, we have discussed how and which physical quantities can be measured. This section will present how we correlate different detected particles to each other. As mentioned, the detectors used in this work can detect impact time and position of particles (e.g. electrons, ions), and this allows us to study the correlation of the detected particle to other particles from the same origin. For instance, a molecule can break up into two charged fragments, and the kinetic energy of both particles can give information on the electronic state of the molecule before breakup. We therefore define *events* as instances where one or more particles from a breakup are registered. An event can be initiated (triggered) by the measurement of a (relatively fast) electron in the case of a continuous light source, or by the start of a pulsed light source.

There are two main acquisition approaches to event-based measurements. In the so-called *coincident* regime [194], the average number of ionizations after each trigger is usually kept well below one (about 0.1 ionizations/pulse), and allows us to assume that all measured particles in the event originate from the same parent particle (molecule or cluster). However, many modern (laser) pulsed light sources offer a high intensity light pulse, at a limited repetition rate. In this case, to keep the recording time of an experiment below a feasible duration, the amount of ionizations in one event is increased. The measured particles can then not directly be correlated one to one. Instead, the covariance between particle properties can be mapped [195–197]. Both the coincidence and covariance method will be briefly introduced and compared.

Coincident detection In the coincident detection mode, one assumes that all particles recorded in one event are correlated. It is then a straightforward procedure to combine and compare properties of particles measured in one event, such as the mass-to-charge ratio of all measured ions. In the example shown in Figure 4.8a, a photoelectron has triggered an event, leading to the *coincident* measurement of a first and second ion (PhotoElectron-PhotoIon-PhotoIon map, PE(PI)^{2}CO map) after ionization of the CO molecule. One can recognize the main fragmentation channel ($O^+ + C^+$) with a metastable tail, an isotope satellite (^{13}C), and a weaker contribution of fragment pairs from triply-charged states ($C^{2+} + O^+$ and $O^{2+} + C^+$).

If one or more charged particles from a parent molecule are not detected, for instance due to particle absorption in a spectrometer grid or a failed detection at the MCP, we record a so-called *aborted event*. The modeling of the relative amount of aborted events, as compared to the true ones, depends

on the detection efficiencies [198]. The calibration of the detection efficiency is discussed in appendix A.

In a coincidence measurement, there is a finite probability to detect a set of particles in one event that does not originate from the ionization of the same parent molecule (or cluster), but from multiple molecules (or clusters). The probability to record such so-called *false coincidences* increases when the ionization rate is increased, or when the detection efficiency of either detector decreases. False coincidence events are observed as vertical and horizontal lines in PEPIPICO maps such as shown in Figure 4.8a. In the case of pulsed extraction fields, a relatively large fraction of the detections can be false coincidences, and can be corrected by randomly triggered events [126].

Covariance mapping In the covariance measurement regime, the origin of the measured particles in one event can generally not be traced back to one, but to multiple parent particles. Therefore, the relation between particle properties (mass, energy, momentum, e.g. [199]) is calculated by studying their correlation over many events. The covariance of a quantity (X) with another (or the same) quantity (Y) can be deduced by calculating a histogram of that quantity at each event (remember that the covariance technique involves many detections in one event). This yields a histogram vector that stores the number of detections within each bin (**X, Y**). The covariance is then defined as [196]:

$$cov(X,Y) = \langle \mathbf{X}\mathbf{Y}^T \rangle - \langle \mathbf{X} \rangle \langle \mathbf{Y}^T \rangle$$

where the angular brackets denote the averaging over all events. Note that this results in a matrix, the so-called covariance map. An example of the ion mass-to-charge variance with itself, in the case of carbon monoxide upon ionization, is shown in Figure 4.8b. The measurement is recorded in the coincidence regime, and artificially converted to a covariance measurement by merging fifty consecutive events into one.

A high intensity in this map denotes a positive correlation, for example at ion pairs that are likely to be detected in the same event. This is why a diagonal (auto-correlation) line always dominates, which states the obvious fact that 'ion X is always detected when ion X is detected', this does not give us any information and is therefore masked in Figure 4.8b. Note that the weak pairs ($C^{2+} + O^+$ and $O^{2+} + C^+$) can also be detected, especially at the edges where the momentum is (anti-) aligned with the spectrometer axis ($\vec{p}||\vec{z}$).

The coincidence (Figure 4.8a) and covariance map (Figure 4.8b) originate from the same experiment and can thus be compared. The metastable tail

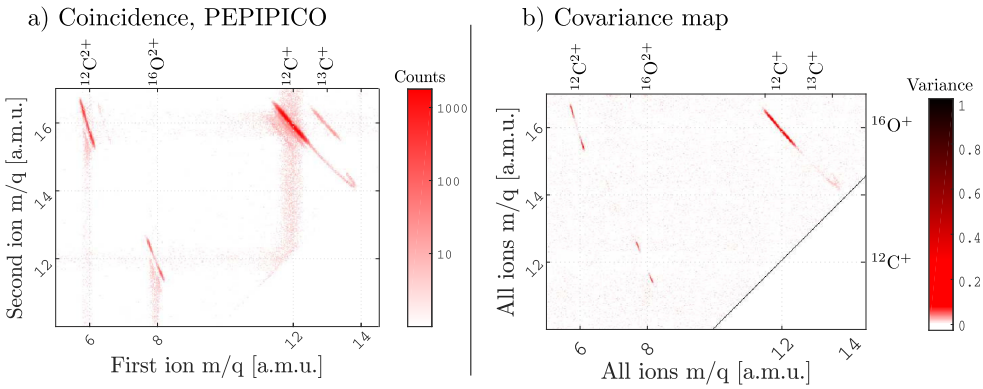

Figure 4.8: Correlation maps created from coincidence and covariance methods. Left: PhotoElectron-triggered PhotoIon-PhotoIon COincidence map (PEPIPICO). Right: covariance map of the same measurement, with every fifty subsequent events merged into one[1]*. The measurement shows data from merged experiments of carbon monoxide (CO) photoionization at 320 eV. Note that the color map is displayed in log scale (left), and the covariance color map is saturated to white below zero, and set to red between 0.1 and 0.3 (right).*

is recognized in the coincidence and covariance map, albeit at lower relative intensity in the case of covariance mapping. The coincidence map can detect the isotope (^{13}C) fragment pair, whereas it is not visible in the covariance map. This indicates that a typical covariance experiment might have lower sensitivity to detect weak fragmentation channels.

Papers I-VI make use of synchrotron or FEL facilities, where the light repetition rate is sufficiently high to operate in coincidence mode. However, the use of coincidence techniques can increase the acquisition times so much that instabilities in a complex experimental setup decrease the measurement accuracy. The use of covariance techniques can provide a means to handle the decrease in information correlation associated with multiple ionizations in one event (or laser shot). The count rate of the experiment is then not dictated by the repetition rate of the light, and covariance is therefore an often used technique in modern laser experiments. **Paper VII** presents an experimental setup that is designed to operate in covariance mode and demonstrates the effective application of covariance techniques.

[1] We have tried several statistical methods to combine events, using various distributions of number of merged events, or a complete reshuffling of the data, and found that the presented scheme leads to the clearest histograms.

4.5 Filters

The data collected in an experiment often needs selection before it can be analyzed, for example when the experiment's aim is to study a small effect that occurs only sporadically or for a particular fragmentation channel. The use of coincidence spectroscopy allows to select the data of interest to a detailed level. We perform the selection by defining conditions. By testing each event to those condition(s), we can create a filter. This filter can then be applied to the data, to create a subset of data that can represent the data of interest. We show two examples of such filters below.

Example: Molecular beam The detection of one particle at a time can result in the measurement of many quantities linked to that particle (e.g. X, Y, T, mass, momentum, etc). This allows the selection of data based on one quantity, and presenting a histogram of that data in terms of another physical quantity. This filtering is useful, for instance when we are interested in a small signal with respect to the background noise. In Figure 4.9, a mass-to-charge histogram of ammonia clusters is shown (blue line). The peaks correspond to singly and doubly charged protonated ammonia clusters. The full histogram is shown in blue, where the signal-to-noise ratio is about 3/2 or lower. In this case, many uncorrelated (noise) hits cause a large background signal. As mentioned in Section 3.3 and shown in Figure 3.12, the molecular beam causes a drift of the impact position, which is especially relevant for heavier ions. The single-particle detection of both mass-to-charge and impact position enables us to select only the data in the vicinity of the molecular beam centre (in this case all within a 15 mm radius). This results in a data selection shown by the red line in Figure 4.9. As seen, the selection results in cutting a large part of the background signal, and the average signal-to-noise ratio increases by a factor of more than 2.5.

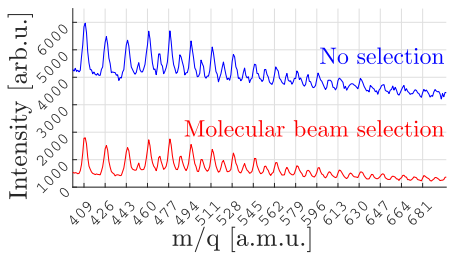

Figure 4.9: Demonstration of the effect of data filtering, in this case on a mass-to-charge histogram of ammonia cluster photoionization: The full dataset (blue curve) is subjected to a filter that selects only data with impact positions with a 15 mm or lower radial distance from the molecular beam centre (red curve).

Example: Ion pair selection The coincident detection of particles allows us to assume a correlation between particles in the same event, and ions that are detected in coincidence can often be assumed to originate from the same parent molecule. From that assumption, we can draw ion-ion correlation maps (such as shown in Figure 4.10a) from the core-excitation of butadiene (CH_2=CH−CH=CH_2). If we want to focus the data treatment on one or a group of these correlated pairs of fragments, we can apply a filter based on ion mass. For example, if we want to only study those fragment pairs that have evaporated two hydrogen atoms, we need to focus on pairs with a total mass of (54-2=) 52 atomic mass units, such as demonstrated in Figure 4.10b.

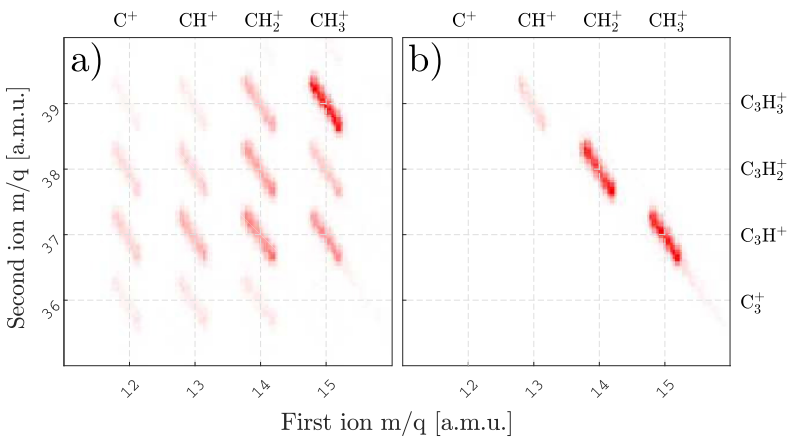

Figure 4.10: Ion correlation maps demonstrating the effect of an ion mass filter. Out of the map of fragment pairs from core-excitation ($C_C \rightarrow \pi^*$) shown in (a), we can select those pairs that have lost two hydrogen atoms (2), by selecting only those pairs with a total ion mass of 52 [a.m.u]. Note that two different color scales have been applied in (a) and (b), each normalized to the maximum intensity.

A filter can thus act on one of the detections (*hit*), such as discussed in the first example, or on a variable composed of the detections in one event, such as the total ion mass in the second example. During analysis, filters can be combined to yield an even more specific filter, and allow the selection of the particular data of interest.

Chapter 5

Results

This chapter will serve as an introduction and overview of the papers in this thesis. The central scientific topic is the transfer of energy and charge within a single free molecule or across molecules in a hydrogen bonded cluster. The charges are created using photons: through core electron ionization, core electron excitation, or valence electron ionization. We will start with examples of charge transfer in molecules and their relation to site-selective dissociation. We first study the core ionization of ethyl trifluoroacetate and continue with a study of core excitation of butadiene in section 5.1.2. The competition between charge transfer and Coulomb explosion is investigated in methyl iodide in section 5.1.3. Afterwards, we introduce the study of charge transfer in hydrogen-bonded clusters. First, the valence ionization of small acetamide and acetic acid clusters is discussed in section 5.2.1, followed by core ionization of ammonia and water clusters in section 5.2.2.

5.1 Energy and charge transfer in molecules

Removing an electron from a core orbital in a molecule creates a local vacancy at a single atom. On a femtosecond time scale, charge delocalization, Auger electron emission and Coulomb explosion can compete, and the electronic and nuclear motions can couple. The localized hole can disperse before it breaks up (statistical dissociation), or the molecule can keep memory of the core site that results in a characteristic break up near the photon absorption location (site-specific fragmentation).

Even though core ionization acts on a local orbital, it is influenced by the chemical environment, which can be observed as a shift in the binding energy

of these core orbitals (*chemical shift*). We employ the chemical shift to choose the location of core ionization or excitation and study the resulting breakup.

5.1.1 Core ionization

We study the site-specific fragmentation of ethyl trifluoroacetate, also known as the *ESCA* molecule (Electron Spectroscopy for Chemical Analysis, [201, 202], see Figure 5.1b). The large relative chemical shifts of the core electronic state binding energies of carbon atoms in the ESCA molecule allow the identification of the core ionization site, seen in Figure 5.1a. The spectrometer employed in this study is a double toroidal energy analyzer, EPICEA [122–124] (Figure 3.1b), to measure the electron energy, and a mass and 3D momentum ion spectrometer, used in coincident measurement mode. The photoelectron energy is thus used as an indicator of the ionization site, and a coincident detection of corresponding ions allows the study of fragmentation patterns at different carbon atom ionization sites.

Core ionized states decay through the emission of an Auger electron, creating a doubly charged molecule. The separation of charge and the subsequent

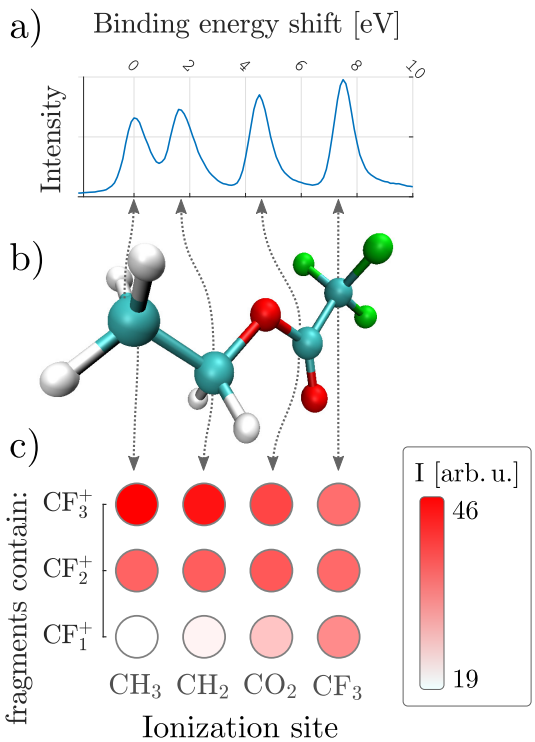

Figure 5.1: (a): The measured photo-electron energy spectrum, with an energy scale relative to the methyl carbon binding energy. (b): A schematic drawing of the ethyl trifluoroacetate molecule. The shown molecular geometry is the most abundant of two existing conformers [200]. (c): The branching ratio of fragment pairs that contain CF_x^+. Note that the color (Intensity) range does not start from zero, to empasize the differences in branching ratios at different ionization sites.

Coulomb explosion creates two singly-charged fragments[1]. The fragment distribution from different core ionization sites (CO_2, CH_2, CH_3 and CF_3) does not induce a large change in the fragmentation behavior. However, a closer look at the relative intensities (or *branching ratios*) of fragment pairs that contain fluorine reveals an increasing level of fluorine loss when the ionization site approaches the CF_3 group (see Figure 5.1c). A similar, but smaller effect is observed for methyl and ethyl fragments, where the methyl branching ratio increases when the core ionization takes place close to the ethyl tail of the molecule (not shown).

We can investigate the sequence of breakup using the coincident measurement of ions, in a momentum analysis of the involved ions; the momentum before breakup is often known, and by momentum conservation, the momentum of an undetected (e.g. uncharged) fragment(s) can be calculated from the measured fragments. In the following, we will denote the momentum of the undetected fragment as *residual momentum* (p_{res}).

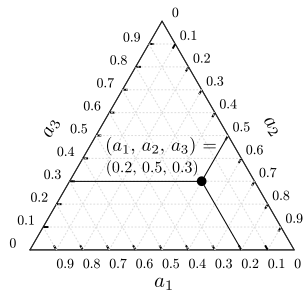

Figure 5.2: Example of a Dalitz plot, where the three axes variables a_1, a_2 and a_3 always add to a value of one.

In the case of two or three measured fragments, a *Dalitz plot* can be used to visualize their relative momenta [203]. A Dalitz plot is a barycentric plot on which three variables sum to a constant. Figure 5.2 shows an example of a Dalitz plot, and an example of a set of (a_1, a_2, a_3) values. A Dalitz plot is often used to visualize the distribution of three values that are related by a conservation law (e.g. energy, momentum).

The momentum sharing between fragments discloses details on the fragmentation sequence in the following way; if the momenta between all charged fragments is the same, and the sum of momenta is close to zero, the breakup was instantaneous. If one of the charged fragments carries less momentum than the other, it originates from a sequence of dissociations.

Let's study the formation of $C_2H_n{}^+$ and $CF_3{}^+$ first. It can be formed as follows:

$$C_2H_5{-}CO_2{-}CF_3{}^{2+} \longrightarrow C_2H_n{}^+ + CO_2 + CF_3{}^+ + (5-n)H \tag{5.1}$$

Note that CO_2 remains uncharged in this dissociation[2]. The momentum sharing of the two charged fragments and the residual momenta is shown in

[1] No singly or doubly charged intact parent molecules were detected.
[2] CO_2^+ is not detected as a charged fragment in our experiment.

a Dalitz plot in Figure 5.3b; only a relatively small amount of momentum is given to CO_2, and the momenta between the two charged fragments are equally shared. This indicates an instantaneous breakup of the two bonds shown in reaction 5.1.

The situation changes when the fragments become smaller, when either a methyl or fluorine atom is lost (Figure 5.3a, c, respectively). The relative size of the residual momentum increases, due to a decreasing momentum of the charged fragment that undergoes additional breakup. This provides evidence for a secondary breakup after the main splitting of the charged fragments:

$$\begin{aligned} C_2H_n{}^+ &\longrightarrow CH_k{}^+ + CH_{n-k} \\ CF_3{}^+ &\longrightarrow CF_l{}^+ + (3-l)F. \end{aligned}$$

We can thus show that the formation of CF_2^+ (and CF^+ as well, not shown) is formed after an initial breakup into CF_3^+, followed by fluorine loss. As shown before in Figure 5.1, the relative intensities of different degrees of fluorine loss depend on the core ionization site. There is thus a limited memory of the ionization site during this secondary breakup.

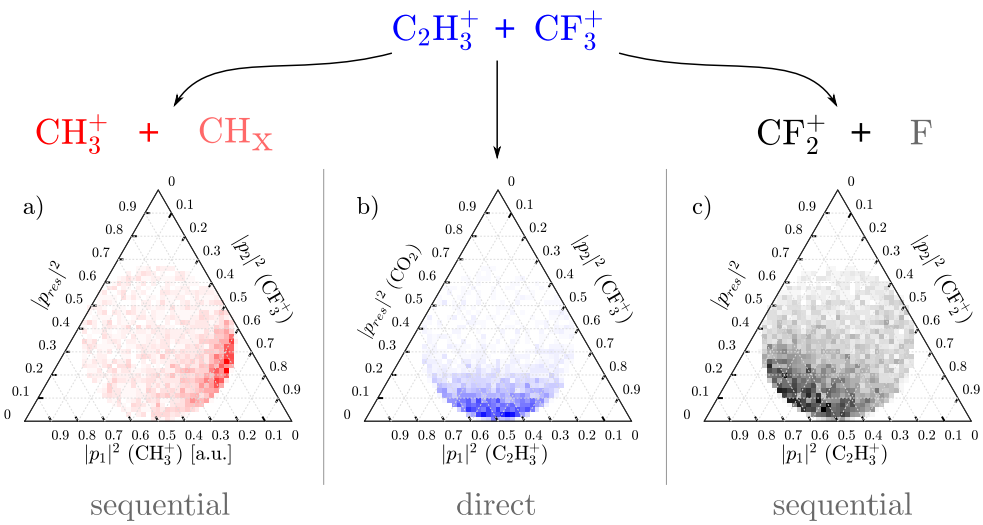

Figure 5.3: The momentum sharing map of two fragments and its residual momentum (at any ionization site): $CH_3{}^+ + CF_3$ (a), $C_2H_3{}^+ + CF_3{}^+$ (b) and $C_2H_3{}^+ + CF_2{}^+$ (c). Each of three axes represents the absolute momentum squared, normalized to the sum of absolute momenta squared $\sum_n |\vec{p_n}|^2$.

Quantum chemical calculations predict the existence of a plethora of final two-hole states, closely spaced in energy. In Figure 5.4, we show density contour plots of the total electron density of the ground state (a), and two examples of the difference in electron density between the two-hole final states and the ground state, (b) and (c). These examples are chosen for their difference in charge distribution, where in Figure 5.4b the charge has increased at the (electronegative) fluorine nuclei, while Figure 5.4c shows an increased electron density at the terminal (methyl) tail. The evolution of a single final state to the breakup into fragments involves both electron and nuclear dynamics, and is challenging to predict numerically. However, the state-averaged properties of the electronic Auger final states (without taking further electronic/nuclear motion into account) can confirm the bond weakening around the CO_2 group and a large probability of charging the two ends of the molecule. A detailed experimental and numerical study on the site selectivity can be found in **Paper I**.

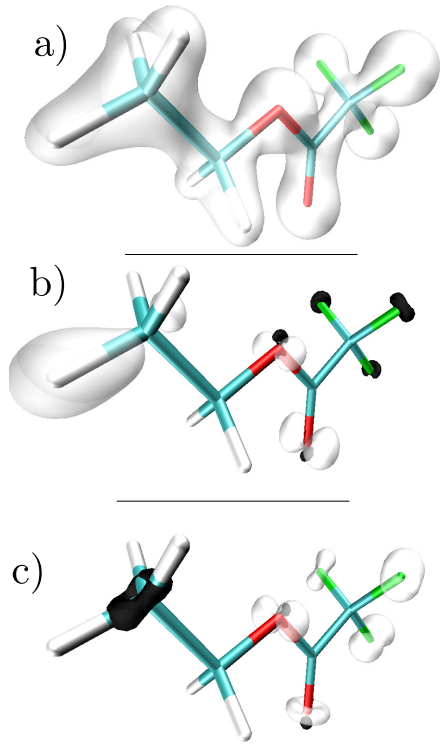

Figure 5.4: Density contour maps of the full electron density in the ground state (a) and the difference between the full and two low energy electronic states (b and c), showing the 7th and 25th lowest energy state, respectively. The white contours show regions where the electron density has decreased, and the black contours show an increased electron density in (b) and (c).

5.1.2 Core excitation

The original vision of Eberhardt *et al.* [27] was to break large organic molecules at certain selectable bonds by choosing a certain photon energy. In the core ionization process discussed before, all sites are ionized with a (nearly) equal probability, and the site-selective effect can only be observed with the help of data treatment techniques. If the site-selective nature of fragmentation were to be used to selectively break a single bond in molecules, a core electron from only

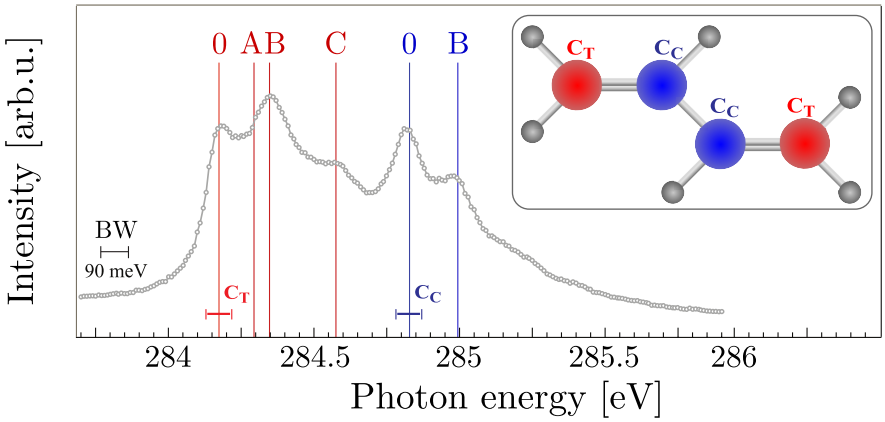

Figure 5.5: The total ion yield upon C1s excitation shows an increase of intensity when the core electron from a terminal or central core carbon atom is excited to the π^* molecular orbital, and the corresponding vibrational excitations. The inset shows a schematic of the butadiene neutral ground state geometry, with the terminal (red) and central (blue) carbon atoms indicated.

one site would need to be promoted. In this study, we employ highly tunable synchrotron radiation to resonantly promote a core electron to an unoccupied valence orbital in 1,3 *trans* butadiene. Butadiene can be viewed as a model system of a conjugated (π) system with alternating single and double (unsaturated) bonds. Unsaturated bonds enable fast proton motion between carbon atoms (e.g. 60 fs in acetylene [56, 204]), and conformal isomerization is thus expected to be a fast process, competing with Coulomb explosion.

We employ a different measurement strategy to study the effect of the core excitation site, as compared to core ionization measurements. As observed for the ethyl trifluoroacetate molecule, the chemical shift can change the binding energies of different core electrons. This can be observed in photoelectron spectra. The excitation energy to promote an electron from different atoms to the same valence orbital is affected by the chemical shift as well. The tunability and small spectral bandwidth of the synchrotron lightsource enables the selective excitation from different core orbitals. In Figure 5.5, we show the amount of observed ions upon photoexcitation of free butadiene at different photon energies. In this narrow photon energy range, certain *resonances* are found, where the photon energy equals the energy required to promote an electron, in this case to an unoccupied anti-bonding (π^*) orbital.

The separate peaks in Figure 5.5 are denoted O and $\{A, B, C\}$, indicating the vibrational ground and excited states, respectively [205]. One can see that

the difference in chemical environments of the four carbons, denoted central C_C (blue) and terminal C_T (red), causes a shift in core-to-valence electron promotion energy (about 0.65 eV), that is close to the C1s binding energy shift (about 0.6 eV [206])[3]. The small difference between these shifts is the result of the difference in how the excitation site influences the π^* orbital.

The determination and assignment of the resonant photon energies (Figure 5.5) allows us to perform separate experiments where the photon energy is tuned to one of the resonances, and study the resulting fragmentation pattern. This allows the creation of a core hole at either the central or terminal carbon atom, possibly in a vibrationally excited state. Each experiment records the correlated ion fragment production in a 3D ion mass and momentum spectrometer as described in [137].

An example of the fragment pair distribution at one of the excitations ($C_C \rightarrow \pi^*$, 0) is shown in an ion-ion correlation map (PEPIPICO) in Figure 5.6. The insets show a schematic of three of the many observed fragment combinations. The direct breakup, without any evidence of hydrogen transfer or hydrogen evaporation (top right inset), is a minor channel. Instead, fragment pairs that cannot be formed by simple bond breaking, but that require hydrogen movement (intra-molecular transfer, or evaporation) are observed. One example is the relatively large two-body fragmentation channel $CH_2{-}CH{-}CH^+ + CH_3{}^+$ that can only be formed by hydrogen transfer, for instance from a central to a terminal carbon atom.

The total number of detected fragment pairs can be summed up and compared at each photoexcitation energy. In Figure 5.7, the relative amount of terminal bond breaking (in this case resulting in the breakup into CH_3^+ and $C_3H_3^+$) is compared to the relative amount of central bond breaking (producing $C_2H_2^+$ and $C_2H_2^+$). The off-resonance branching ratios are shown as reference points. The relative abundance of fragment pair production from off-resonance photoabsorption does not seem to deviate strongly from central carbon excitation. The excitation at the terminal carbon site, however, leads to a more frequent breaking of the C_C-C_T bond, compared to the C_C-C_C bond. The memory of the terminal core excitation thus appears to be present during dissociation, and cause an increasing probability to break the bond closest to that site. The C_C-C_T (or terminal) breakup has been related to a conformational *gauche* isomerization of the molecule before dissociation [207]. The C_C excitation might thus increase the probability for the *trans*-to-*gauche* isomerization and cause a more localized dissociation.

[3]Note that the chemical shift in butadiene is smaller than that in the ESCA molecule due to the absence of electronegative atoms that can induce large shifts.

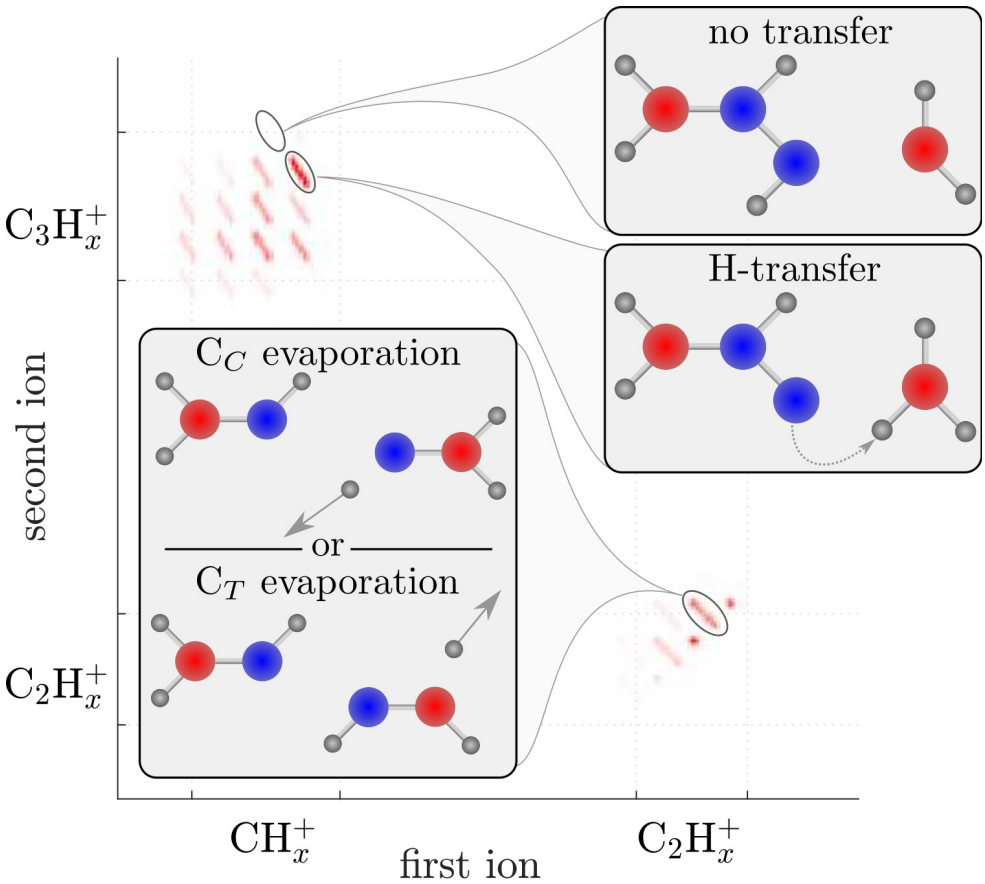

Figure 5.6: Ion-ion correlation map (or PEPIPICO) of the most complete fragment pairs. The insets highlight fragment pairs where the molecule broke up without noticeable dynamics ('no transfer'), where a proton has migrated to a terminal end ('H-transfer'), and where a hydrogen has evaporated from one of the fragments ('C_C or C_T evaporation'). In this example, $h\nu = 284.9$ eV ($C_C \rightarrow \pi^*$).

The molecule has a high probability for hydrogen to evaporate from the central (C_C) or terminal (C_T) carbon atom, as is for instance seen in Figure 5.6, inset bottom right. Fragments formed by a break of the (double) $C_C{-}C_C$ bond are observed as well. The evaporation site (central or terminal) and the relation to the excitation site can clarify the dependence of the evaporation process on the excitation site. The site of the evaporated hydrogen is not clear due to the similar mass of both products. Therefore, we employ butadiene that is partially deuterated at the terminal carbon ($CD_2{-}CH{-}CH{-}CD_2$) to lift

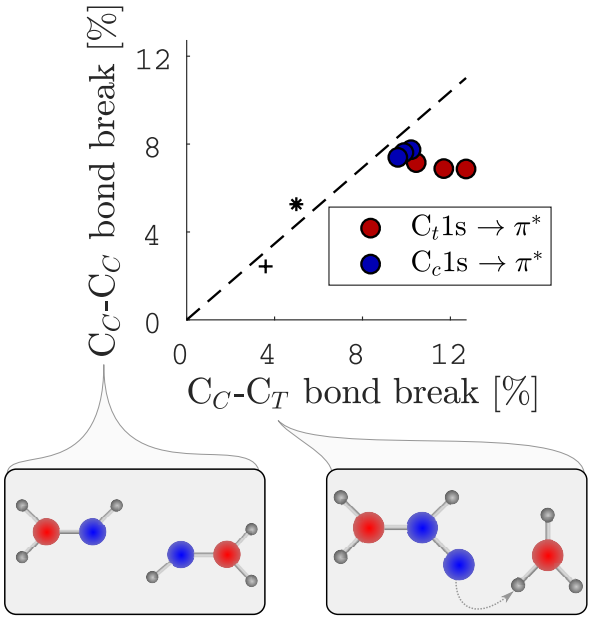

Figure 5.7: The branching ratio of terminal bond breaking (producing CH_3^+ and $C_3H_3^+$) versus that of central bond breaking (producing $C_2H_2^+$ and $C_2H_2^+$)[4]. The branching ratios upon photoexcitation are shown in circles, ionization below resonance in crosses, and above resonance by asterisks, along with a least square fit (dotted line) from the origin along the off-resonance points. Red/blue markers indicate excitation of the terminal/central core shell electron, respectively .

the mass ambiguity of a terminal and central-evaporated hydrogen.

Figure 5.8 shows the branching ratios of fragment pairs that arise from evaporation from either the terminal or the central carbon atoms, taken from measurements on partially deuterated butadiene molecules. The branching ratio is normalized by the total number of fragment pairs detected. A relative increase of fragment pairs that have evaporated a protium/deuterium from a central/terminal carbon leads to a higher X/Y value in the plot, respectively. For the off-resonance measurements, where no core electron is promoted to a high valence orbital, the evaporation from central and terminal carbon increases proportionally (positive correlation) as the photon energy is changed.

The on-resonant excitation mostly increases the evaporation from terminal carbons, at the cost of evaporation at the central carbon (negative correlation). The anti-correlation could be interpreted as an energy conservation effect: evaporation at one site decreases the total internal energy of the molecule and inhibits further evaporation at other sites. We can further observe that ionization at the terminal carbon causes a higher hydrogen evap-

[4]Fragments with equal mass (C_C-C_C bond break) have very similar detector impact times, possibly leading to detection of only one of two particles (dead-time), leading to an underestimation of its real branching ratio.

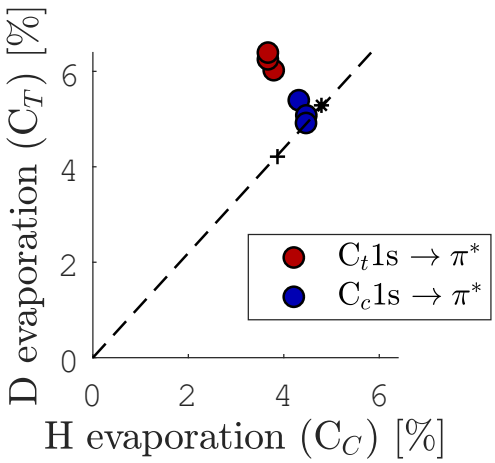

Figure 5.8: The branching ratio of hydrogen evaporation from the terminal or central carbon atom (fragment pairs shown in the left inset in Figure 5.6), for photoexcitation or ionization below resonance (black cross), and above resonance (asterisk), along with a least square fit (dotted line) from the axes origin along the off-resonance points. Measurements performed on partially deuterated butadiene ($CD_2{-}CH{-}CH{-}CD_2$).

oration rate at the terminal carbon. This indicates that the evaporation is at least partially an effect of localized energy. A detailed study of the branching ratios of different fragment pair channels can be found in **Paper II**.

5.1.3 Charge transfer vs Coulomb explosion

In the results presented before, the charge separation is faster than the dissociation, and the double ionization therefore always leads to the formation of singly charged fragments. We will now investigate the rate of charge separation in a small multi-charged molecular system. We want to study the dependency of charge transfer on the number of charges in the molecule and the distance between nuclei in the molecule. We investigate the charge transfer by sequentially photoionizing one part of a molecule, and observing the redistribution of charges in the resulting fragments.

To initially localize the electron hole at only one of the nuclei, the ionization should remove electrons from the inner shell or core orbitals, often requiring X-ray energies. Additionally, the absorption of multiple photons by a molecule requires a high intensity light source. The combination of a short high intensity light pulse with a well-defined X-ray photon energy distribution are the unique properties of an X-Ray free electron laser, and are thus the light source employed in this study. To control the ionization site, we choose a molecule with a strong difference in ionization cross section at different atoms, namely methyl iodide (see Figure 5.9). At the used photon energy of around 90 eV, the ionization cross section of neutral iodine ($4d^{-1}$) is 20 times larger than that of neutral carbon ($2s^{-1}$ or $2p^{-1}$) [208, 209]. The photoabsorption

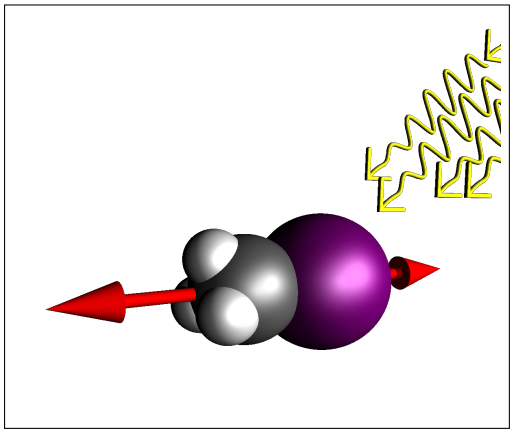

Figure 5.9: Schematic drawing of the methyl iodide molecule. We study the momentum and charge distribution upon multi-photon ionization and Coulomb explosion. The red arrows indicate the direction of movement of the carbon and iodide nuclei during Coulomb explosion. Geometry from [210].

is thus most likely to occur at the iodine nucleus, and the charging of other parts of the molecule will mostly be due to intra-molecular electron transfer.

We perform ion-ion coincidence momentum imaging, which allows us to measure the momentum correlation of the detected fragments. We detect mostly carbon and iodine ions in charge states up to three and seven, respectively. However, at a low number of absorbed photons, the hydrogen does not always dissociate from the carbon atoms (as reported from single photon ionization [211]), and methylium is detected in coincidence with the iodine cation. Figure 5.10 shows the momentum correlation at increasing methyl carbon loss. The momentum of the iodine ion is anti-correlated to the methyl ion (CH_3^+, see Figure 5.10a), aligning with the diagonal reference line. The methyl ion momentum decreases slightly as more hydrogens leave the fragment (see Figure 5.10b-d) compared to the iodine ion, seen by the slight deviation from the pure anti-correlated reference line. The measured correlation is close to that expected when the detected and undetected methyl fragments share the velocity equally (black dashed refererence line). Note also the strong increase in momentum distribution broadening as one or more hydrogen remains undetected, as compared to the two-body breakup forming CH_3^+. Both the changing momentum correlation and the increased momentum broadening imply that the hydrogen atoms participate in the momentum sharing, and are therefore still present at the time of dissociation.

At high FEL intensity[5], iodine will be further ionized and this can lead to the formation of carbon containing fragments of higher charge states as

[5]The experiments were conducted at average pulse energies of 0.4 μJ and 0.9 μJ, and intensities above 2×10^{13} W/cm^2.

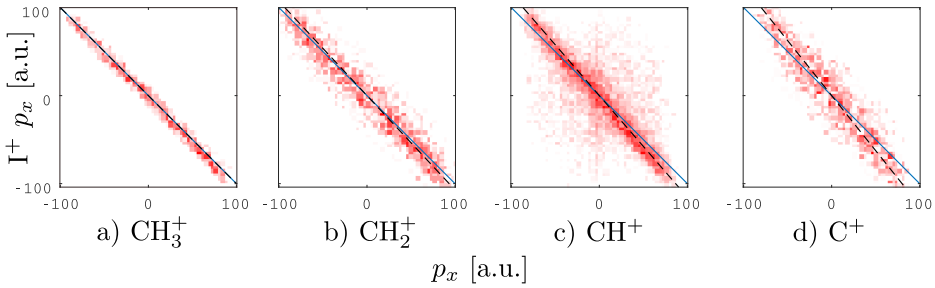

Figure 5.10: Momentum correlation between singly charged Iodine and methyl fragments, with an increasing number of hydrogens evaporated from the methyl group: from a complete two-body fragmentation (a) to the loss of three hydrogen nuclei (d). We show the correlation between momentum component x, and correlations between other components show the same trend. Blue reference line indicates a pure anti-correlation ($p_{x1} = -p_{x2}$), and black dashed line an equal velocity of (undetected) hydrogen and carbon fragments. Data recorded at a (low) pulse energy of 40 nJ.

well. At higher charge states of the carbon containing fragment, the carbon fragment does not contain any hydrogen. The covalent C-H bonds are broken when the bonding orbitals are emptied, suggesting the charging of hydrogen (to protons) before they fragment. The collection efficiency of (relatively fast) protons is limited through the use of weak electrostatic field strengths in the spectrometer, and the coincident proton(s) with the carbon and iodine ions were therefore difficult to detect in this experiment.

In order to provide additional insight into the charging mechanisms, we have developed a Monte-Carlo statistical model to describe the charging and charge distribution during the photoionization and Coulomb breakup. The charging of the molecule is initiated by photoabsorption. The cross section of photoabsorption is assumed independent of the iodine charge state, as extrapolated from the expectations from quantum calculations up to the triply charged state [212]. After inner-shell ionization, electronic relaxation through Auger decay can occur. This relaxation channel dominates in the neutral and the first few multiply charged states of iodine at the photon energy used in this study [208], as in xenon [213, 214], but is expected to become unlikely at higher charge states. We therefore assume that the normal Auger decay from higher charged states than four is not energetically allowed. The hole lifetime of these charged states is not known from literature, but the best agreement between model predictions and experimental observations indicates that normal Auger decay occurs a few femtoseconds after ionization of iodine (with initial state I,

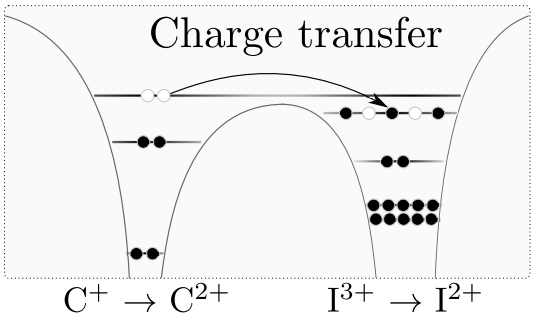

Figure 5.11: Example of a carbon to iodine electron transfer: the Classical Over Barrier model predicts a transfer of charge when the maximum of the classical potential energy between two nuclei is below the electron orbital energy.

I^+, I^{2+}), similar to that observed in neutral photoionization [215]. The lifetime is lower than the typical time between photoabsorption at our experimental conditions. Therefore, normal Auger decay is most likely to occur after one photoabsorption (and before another one occurs). The charging mechanism can thus be described as a sequential chain of photoelectron and normal Auger electron emissions[6].

The modeling of the distribution of charge is partially based on the Classical Over Barrier (COB) condition [216]; The nuclei are treated as charged point masses, and the charge transfer from one nucleus to the other is only allowed when the maximum classical potential energy is lower than the energy of the highest occupied orbital, see Figure 5.11. If the transition is COB-allowed, it is assumed to be instantaneous. Furthermore, the model takes the anticipated hydrogen charging into account by assigning a 'partial charge' to each hydrogen in a three-fold symmetric configuration. For the sake of clarity and simplicity, we illustrate in Figure 5.12 the modeled charge buildup and transfer until the formation of triply charged carbon.

Figure 5.12a presents how we model the charging and sequential removal of electron density around the hydrogens in the methyl group. The charge transfer is initiated when iodine is doubly charged, and the charge density of a single charge on the methyl group is assumed 'split' into ten percent on every hydrogen nucleus, and seventy percent on the carbon nucleus. At increasing methyl charge states above one, it is assumed that one hydrogen atom becomes fully stripped of an electron with each increase in charge state. Since the model uses a three-fold symmetry around the C-I axis, this results in an increase of 0.3 partial charge at the hydrogens, and an increase of 0.1 at the carbon nucleus. The decision for these charge distributions is based on

[6]The relatively weak channel including Auger decay cascade is also included in the simulation

the best agreement with experimental observation.

Figure 5.12b shows how the charging and charge transfer is modeled after all hydrogen atoms are assumed to be stripped from electrons. The critical distance decreases as the charge states of both nuclei increase [217]. However, the average internuclear distance increases as well. The charging and charge transfer rate are thus strongly correlated: a high iodine charging rate, before a substantial increase of internuclear distance, allows for charge transfer to carbon, while a low iodine charging rate will cause dissociation that inhibits further charge transfer. The exploration of different charging mechanisms in the model helped us to identify that mostly the lowest iodine charge states are responsible for the formation of the doubly and triply charged carbon states; the internuclear distance increases at a higher rate than the critical distance increase (induced by photoabsorption and Auger decay). The final carbon charge state is therefore mainly dependent on the ionization rate at the onset of dissociation, and reaches a maximum charge state of three under our experimental conditions. A detailed discussion of experimental and numerical results can be found in **Paper III**.

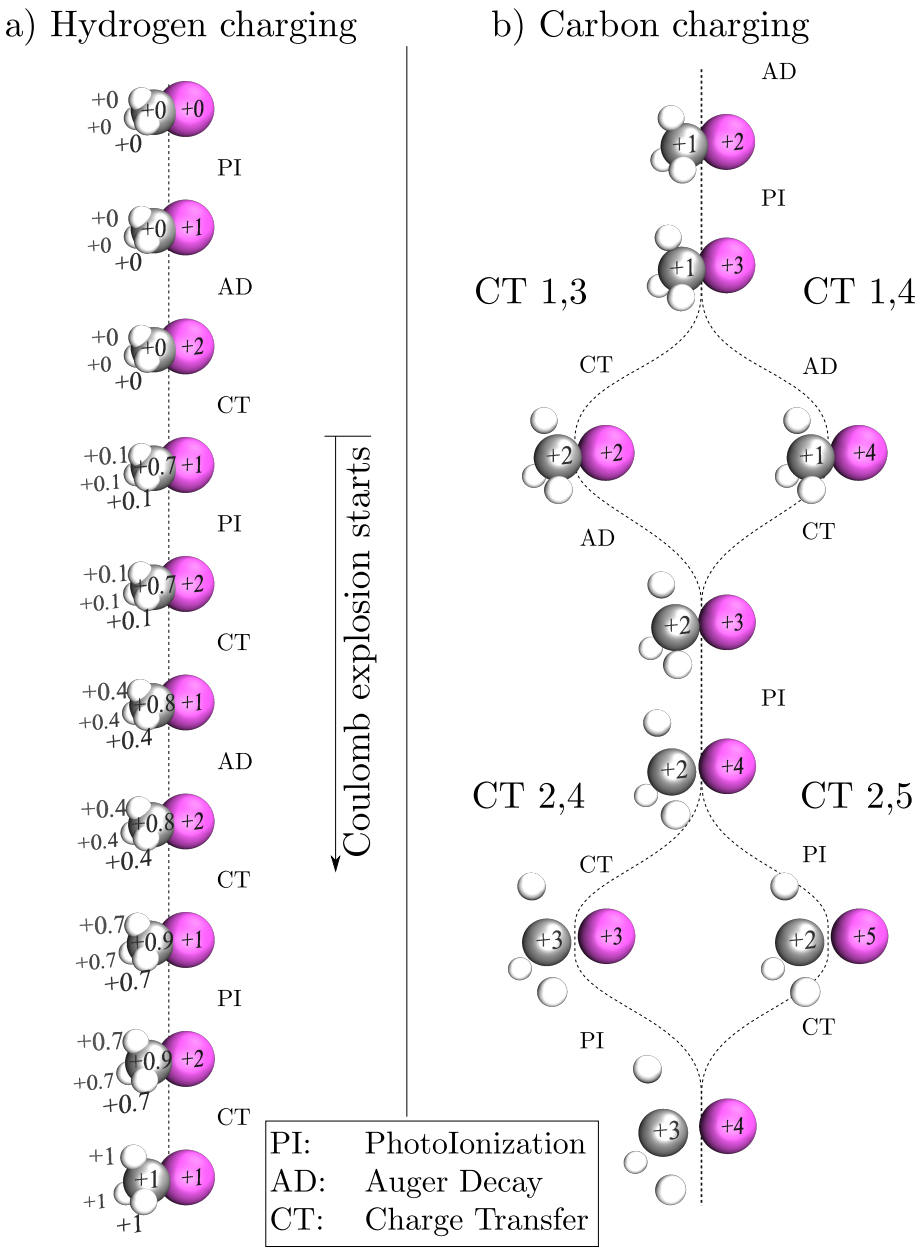

Figure 5.12: Charging mechanism of methyl iodide through sequential X-ray absorption. (a) Removing the electrons from the protons, and (b) the further removal of electrons from carbon orbitals. The branches in (b) are pathways when charge transfer is allowed (left, CT 1,3 and CT 2,3) or not (right, CT 1,4 and CT 2,5).

5.2 Energy and charge transfer in H-bonded clusters

In small clusters, the charge has more freedom of movement than on an single isolated molecule. As discussed in section 2.4, proton transfer and hopping can play a role in the charge transfer in hydrogen bonded condensates. In the research presented below, the charge transfer upon valence and core ionization of hydrogen-bonded clusters is studied by using mass and momentum spectroscopy.

5.2.1 Single ionization

One of the simplest model systems for the study of proton transfer is a small singly-charged hydrogen-bonded cluster (dimer, trimer, etc). The proton transfer barrier and temperature dependency in these systems can be studied without the interference of a second charge (e.g. through Coulomb interaction) or complex multi-body dynamics of surrounding molecules (such as in a liquid). We use acetic acid and acetamide clusters as such model systems. Acetic acid and acetamide differ only in one functional group, namely a carboxyl (acetic acid) or amide (acetamide) group. Both of these groups contain a doubly-bonded oxygen, so the difference in hydrogen bonding properties is restricted to a hydroxyl ($-$OH) in acetic acid and a primary amine ($-NH_2$) in acetamide. Note that these differences are comparable to the differences between the water and ammonia molecules.

In this experiment, the clusters are produced through supersonic expansion[1], ionized by means of synchrotron radiation (MAX-III) over a range of photon energies (around 10 eV) and the ionic fragments are detected by an ion TOF spectrometer. Mass spectra upon photoionization of acetic acid and acetamide are shown in Figure 5.13 at photon energies around the single ionization energy. The spectra are dominated by the monomer, mostly from the uncondensed part of the molecular beam. Note that a large part of the cluster fragments contain an extra proton. These fragments are called *protonated*, a result of proton transfer from the ionized site to a hydrogen-bonded neighbor molecule:

$$(CH_3COOH)_k^+ \longrightarrow (CH_3COOH)_{k-1}H^+ + CH_3COO$$
$$(CH_3CONH_2)_k^+ \longrightarrow (CH_3CONH_2)_{k-1}H^+ + CH_3CONH$$

[1]The cluster source is designed and built by Kuno Kooser at the University of Turku.

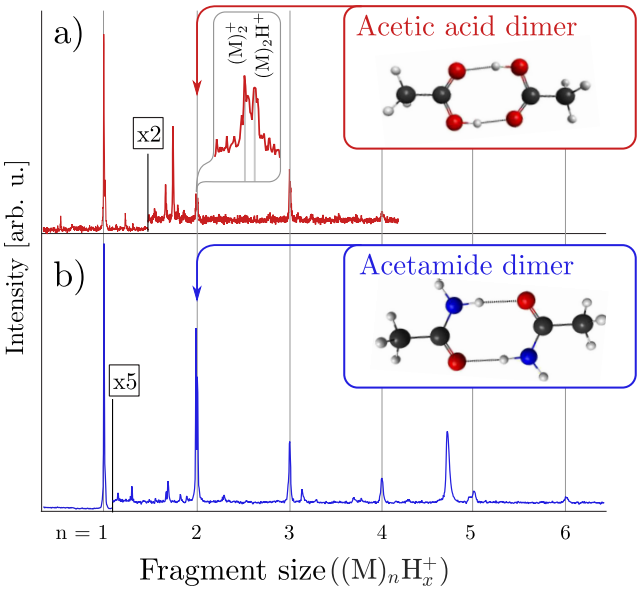

Figure 5.13: Mass spectrum of acetic acid (a) and acetamide (b) with a schematic representation of the neutral dimer configurations in the insets [218]. The hydrogen bonds are indicated as long lines. The fragment size is expressed in the number of molecules (M) in the cluster. The spectra shown are integrated over the photon energies ranges 9-11.3 eV (acetic acid) and 8.5-10.5 eV (acetamide). A complete mass peak assignment can be found in [218].

in the case of acetic acid and acetamide, respectively. The size of the neutral molecule before ionization (the *parent* cluster) is thus at least one monomer subunit larger than that of the detected fragment size.

Hydrogen migration

In order to reach the proton-transferred state, intra-molecular geometric changes are required to migrate a hydrogen (isomerization) within the molecule. The isomerization requires to cross an energy *barrier* due to a transition state with a higher potential energy. The energy barrier sets a lower limit to the internal energy in the system above which hydrogen migration can occur; a higher average cluster temperature allows a higher fraction of the cluster to reach the proton transferred state. This can be verified by the smaller relative amount of protonated cluster fragments measured when the temperature is decreased by stronger expansion conditions of the cluster beam (not shown). The hydrogen migration energy barrier of acetic acid and acetamide is estimated by quantum mechanical calculations to be around 1.11 eV and 1.5 eV, respectively. The higher barrier of acetamide corresponds to a larger amount

of unprotonated acetamide fragments observed, compared to acetic acid.

Appearance energy

If the photon energy is close to the ionization energy of a molecule and well below the double ionization potential, photoabsorption can cause ionization of one electron at most. A partial ion yield can be recorded by scanning the photon energy across the ionization threshold energy. The minimum photon energy at which a certain (cluster) ion is observed is called the appearance energy[2] and can be determined from these partial ion yields. The appearance energies of acetic acid and acetamide clusters are shown in Figure 5.14. The ionization potential of the single molecule (dashed reference line) and the appearance energy of a cluster ion of the same molecule are closely linked, and the appearance energy and ionization energy indeed line up with the appearance energies of the neat monomers. The neat monomer at those energies can thus be expected to originate from the uncondensed molecule. At larger sizes, the appearance energy is always lower than the single molecule's ionization energy. The decrease in appearance energy (and thus ionization energy) is an effect of the neighboring molecules that provide the possibility to populate (less localized) ionic states. Note that the decrease in appearance energy is not monotonic in acetic acid, where the appearance energy of the dimer fragment shows the lowest appearance energy. An electron spectroscopic study of the energy deposited - the difference in photon energy and photoelectron energy - could shed more light on the reasons behind the particularly low appearance energy of the acetic acid dimer.

The protonated acetic acid monomer appears at a lower photon energy than the corresponding neat monomer, indicating that the protonated monomer signal originates from larger parent clusters followed by proton transfer and dissociation. In contrast, the protonated acetamide cluster does not appear at lower photon energies than the acetamide monomer. This could be a consequence of the lower hydrogen transfer energy barrier of acetic acid, such that less internal energy needs to be deposited by the photon to result in proton transfer.

A detailed study on the possible fragmentation pathways, including the role of covalent bond breaking and supported by *ab initio* quantum mechanical calculations, is performed on acetic acid and acetamide clusters in **Paper IV**.

[2]The ionization energy can be different from the appearance energy due to dissociation into a charged and uncharged fragment.

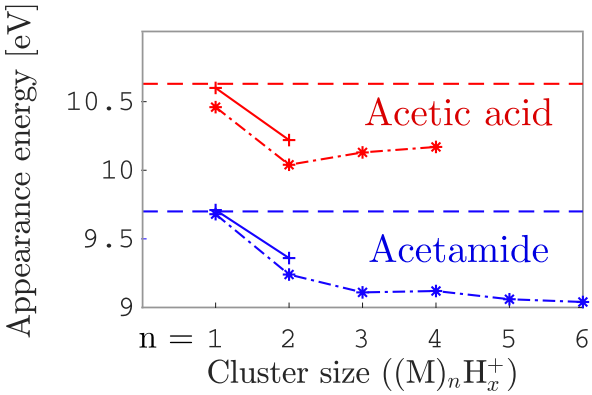

Figure 5.14: The size-dependent appearance energy of acetic acid (red) and acetamide (blue), protonated (dash-dotted lines, $x = 1$) or neat (solid lines, $x = 0$) clusters. Single ionization energies indicated by horizontal dashed lines [219, 220]

5.2.2 Double ionization

The length scale of proton motion induced by single ionization can remain limited to interactions between nearest-neighbor molecules in the absence of a driving force to move charges. When more charges are created, initially close to one another (i.e. on one molecule), the Coulomb repulsion drives charge and proton motion over a longer range. Upon charge separation, the repulsive force decreases, which can even lead to a stable doubly charged cluster. Here, we are interested in studying the charge and proton dynamics over a longer length scale. To investigate the important parameters for stabilization, we analyze the mass and momentum of ionic products.

In the following, we present an overview of the ions produced upon double photoionization of hydrogen bonded clusters. Firstly, we discuss the fast fragments that form before proton transfer can occur; this is followed by a discussion on the protonated fragments formed by doubly- and triply-charged parent clusters, and finally the larger stabilized dication clusters are presented. These three study cases focus on the response of pure ammonia and mixed ammonia-water clusters.

Methods

The neutral clusters are produced in an adiabatic expansion, producing a broad range of cluster sizes (e.g. see Figure 3.11). The production of mixed hydrogen-bonded clusters is achieved by expanding a premixed flow of water and ammonia (co-expansion). We employ core ionization to produce two near charges in the cluster, mostly on one molecule or on two H-bonded neighbors (see section 2.1). Figure 5.15 shows the three types of products that we will discuss: the products that formed before proton transfer (a), the fragments

formed after proton transfer (b), and the larger doubly charged clusters that can host two charges[3] (c).

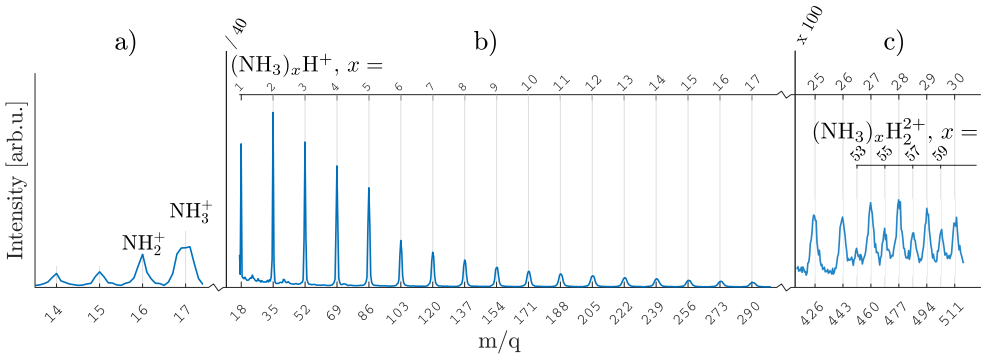

Figure 5.15: Mass-to-charge spectrum of ammonia clusters upon photoionization, in three regions: (a) unprotonated fragments detected with correlated clusters (in coincidence), (b) protonated fragments ($(NH_3)_xH^+$) that have broken in two or more fragments, and (c) the appearance of stable doubly charged clusters at around 53 ammonia units. Spectrum measured at a photon energy of 420 eV, and an expected average neutral cluster size of about 50 ammonia units.

Dissociation before proton transfer

The proton transfer from the ionization center to a hydrogen-bonded neighbor occurs on a femtosecond timescale [34–37] and is exothermic by about 0.74 eV [221, 222]. However, we observe that a small portion of the clusters dissociate before proton transfer has occurred on both fragments. We observe that they are correlated to small protonated clusters (e.g. $(NH_3)H^+ + {NH_3}^+$), as shown in a PEPIPICO correlation map in Figure 5.16a. An analoguous channel is not observed in water (Figure 5.16b). This might be because proton transfer in water is more exothermic than in ammonia [223], and the typical water-water hydrogen bond is stronger than in ammonia [76], which can make proton transfer in water more likely to occur within the time scale of the dissociation.

[3]The spectrum displayed in Figure 5.15c is calculated using the molecular beam filter discussed in section 4.5.

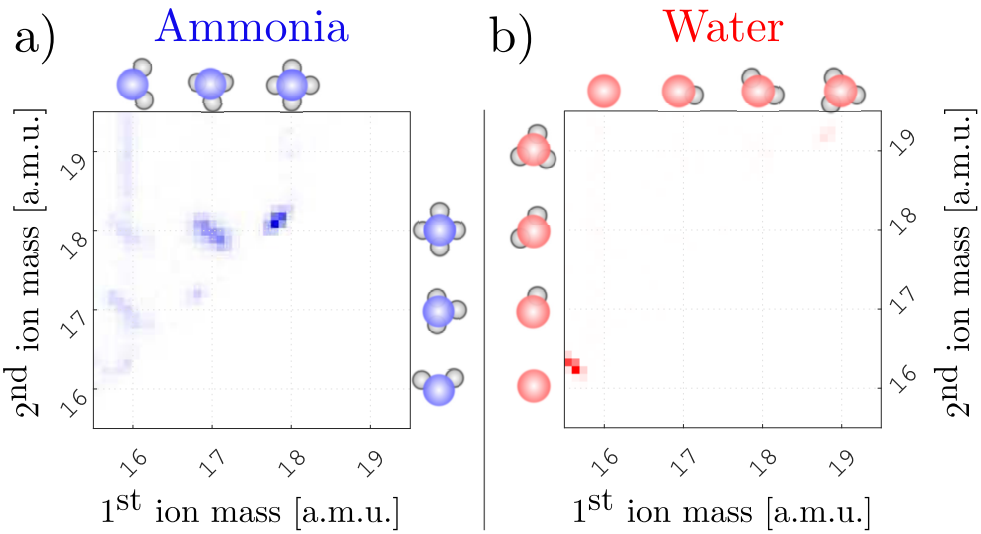

Figure 5.16: Ion-ion mass correlation map (PEPIPICO) in the mass range of monomer fragments. The unprotonated ammonia channel is observed in (a) at the masses (17,18) and (16,18). Note the absence of such channel in water clusters at (18,19) or (17,19) in (b)[4]. Photon energy: 420 eV (NH_3) and 550 eV (H_2O).

The production of the unprotonated fragment (NH_3^+) must therefore be the result of a limited interaction with surrounding molecules, inhibiting proton transfer. The origin of the fragment pair can thus be a small cluster (where no other molecules are available to interact with), or at the very surface of a larger cluster.

The probability of producing small clusters such as dimers and trimers (2 and 3 molecules, respectively), relative to the total production of clusters, can be controlled by the stagnation conditions of the adiabatic expansion (as shown in Figure 3.11). However, the relative abundance of unprotonated fragment pairs does not change as the neutral size distribution changes (not shown), indicating that the unprotonated channel cannot exclusively originate from small neutral clusters.

The study of the unprotonated fragments in heterogenous clusters of water and ammonia allows for a more detailed view on the origin of this channel. As discussed, the unprotonated pair is not produced from pure water clus-

[4]Note the measurement of residual O_2 around (16,16) in the vacuum chamber, partly masked due to detector dead-time

ter ionization (Figure 5.16b). Paradoxically, the relative abundance of the unprotonated channel does not decrease with water mixing. Geometry optimization calculations of the neutral cluster suggest the water molecule to be centrally located, and ammonia molecules to be more prevalent at the surface [224]. The prevalence of water molecules at the centre indicates an earlier condensation of water during adiabatic expansion, and therefore we expect a high concentration of water molecules in small heterogenous clusters. All above statements indicate that this channel originates at the surface of larger cluster hosts.

We therefore suggest that this partly unprotonated fragment pair originates from the surface of a larger cluster, such that the kinetic energy of the fragments is reduced by the nearest neighbor bond breaking. The ionization, delocalized decay (e.g. ETMD(2)), and dissociation can all occur rapidly at the surface (see Figure 5.17).

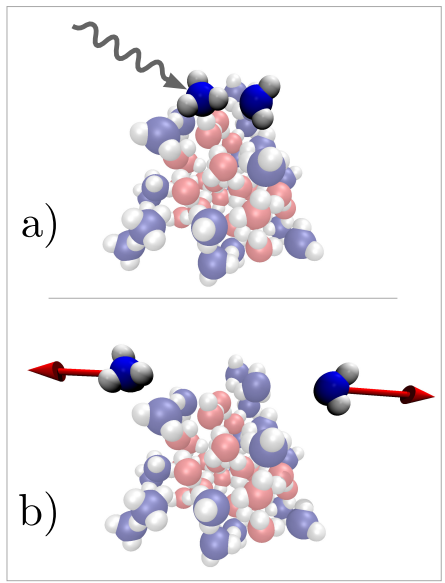

Figure 5.17: Suggested mechanism leading to unprotonated fragments: ionization of a molecule close to its surface (a), and two (or three) neighboring molecules are involved in the electronic decay, leading to the dissociation of two singly charged molecules without further interaction (b). Geometry from [224]

5.2.3 Dissociation after proton transfer

The majority of fragments are protonated (see Figure 5.15b). Note that the average size of these fragments (3-4 cluster units) is much smaller than the neutral cluster size (around 53). The detected fragment(s) thus only contain a small portion of the total amount of molecules in the cluster. The single-molecule evaporation is too slow to be observed in our spectrometer [101, 102], and to explain the decrease in size by unimolecular evaporation would require an evaporation rate that is much higher than expected [104]. We therefore expect the formation of (large) uncharged fragment(s) to be the origin of the large size discrepancy between the neutral parent cluster and the detected charged fragments.

Momentum correlation

The strength of a coincidence experiment is the ability to detect all charged particles from a single origin. However, this is not always achieved due to a limited detection efficiency. The ion detector might have registered only two of three fragments from a triply ionized parent cluster. Such aborted detection is in general very likely since the typical ion detection efficiency is around 30% (see Appendix A).

However, an aborted detection leaves a signature in the momentum correlation of the fragments that are registered. For example, Figure 5.18(a-c) shows the anticipated directions of momenta of specific charge states (2, 3 and 4 charges in a, b and c, respectively), as a result of Coulomb repulsion. One can see that the angle between the momenta is different for various charge states, namely 180° (2 charges), 120° (3 charges), and 109.5°(4 charges, tetrahedron).

Figure 5.18d,e shows polar histograms of the smallest angle between two measured momenta in one event, in the case of two (a) and three (b) coincident detections (red plusses), respectively. These show that most momenta are opposite to one another (angle larger than 90°), due to the Coulomb repulsion. However, we expect that this data contains aborted coincidences with one or two charged fragments undetected (as mentioned earlier). With the use of conservation of momentum, we can design filters that select only those events that have detected all charged fragments. The contribution of fully detected two-particle events can be selected by restricting the sum of all momenta:

$$|\vec{p}_{\mathrm{sum}}| = \left| \sum \vec{p}_i \right|, \tag{5.2}$$

where $\vec{p}_i$ is the momentum change of fragment i. We limit $|\vec{p}_{\mathrm{sum}}|$ to 40 and 60 atomic momentum units in double and triple coincidences, respectively, which lead to a peak centred at the expected relative angles (180°and 120°). The validity of this filter is confirmed by Gaussian peak fits at these angles (solid grey line), where the filtered momentum correlation lines up with the fit of the expected charge state. The total intensity of aborted and complete detections is in good agreement with that from the detection efficiency model (see Appendix A).

Kinetic energy release

If the cluster dissociates, it forms a fragment around each charge. These fragments have time to rearrange to the most energetically favorable orientation.

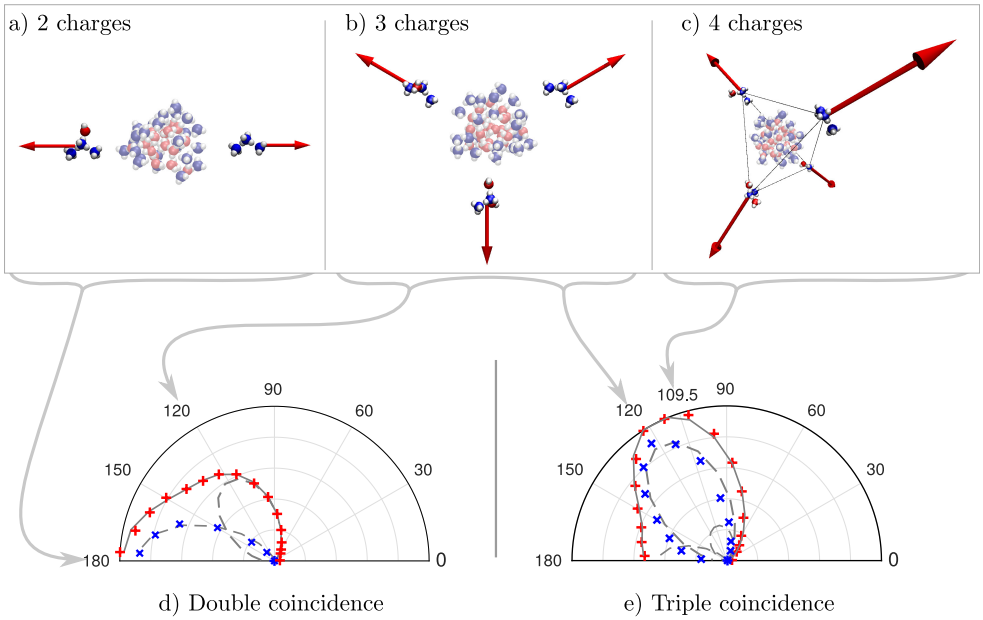

Figure 5.18: (a-c): Coulomb repulsion steers charge carriers along minima in the potential energy surface which maximizes the mutual charge-to-charge distances. The energy-optimized directions are given for 2, 3, and 4 charges in (a),(b),(c), respectively. Optimized neutral parent and fragment geometries are drawn from given geometries, [224] and [225], respectively. The measured angular momentum correlation of two and three coincident particles (red plusses in (d) and (e), respectively), can be separated into contributions from different charge states. The detections where charged fragments have been detected, possess a total momentum ($|\vec{p}_{sum}| = |\sum \vec{p}_i|$) below 40 and 60 [a.u.] for (d) and (e), respectively. This yields a histogram centred at 180° and 120°, respectively, as expected from (a) and (b). The grey dashed lines indicate Gaussian peak fits centred at the expected peak centres.

The charge movement through proton hopping causes rotational and vibrational excitations [226], thus heating up the cluster. Upon (instantaneous) fragmentation, the Coulomb repulsion accelerates the charges in the fragments. This causes the fragment to accelerate, but can also cause additional ro-vibrational excitations in the fragments [38]. From the momentum and mass of all detected particles, we can calculate the total kinetic energy release (KER) of all charged fragments (see Figure 5.19a).

The Coulomb energy upon instantaneous breakup to the charge-to-charge distance at breakup can be written as a sum of the measured kinetic energy release and the energy in ro-vibrational modes in the fragment (E_{int}):

$$KER + E_{\text{int}} = \frac{1}{4\pi\epsilon} \sum_i \sum_{j<i} \frac{q_i q_j}{r_{i,j}} \tag{5.3}$$

$$= \frac{1}{4\pi\epsilon} \sum_i \sum_{j<i} \frac{1}{r_{i,j}}, \text{ with } q_i = q_j = 1 \tag{5.4}$$

$$= \frac{1}{4\pi\epsilon} \frac{1}{r} \binom{N_q}{2}, \text{ with } r_{N_q} = r_{i,j} \tag{5.5}$$

where ϵ is the permittivity, q_i (q_j) is the charge of fragment i (j), $r_{i.j}$ is the distance between charges, N_q is the number of fragments (or charges)[5], and r_{N_q} is the distance between N_q fragments, assumed constant for all fragment combinations. The kinetic energy release in these multi-body systems is thus a lower limit of the Coulomb energy of the system directly after ionization (see Figure 5.19b), with E_{int} a generally unknown variable.

The above expression can be specified for the triply and doubly charged clusters as:

$$[KER + E_{\text{int}}]_{\text{double}} = \frac{1}{4\pi\epsilon r_2} \tag{5.6}$$

$$[KER + E_{\text{int}}]_{\text{triple}} = \frac{3}{4\pi\epsilon r_3} \tag{5.7}$$

At the same interfragment distance (r), one can thus expect a three times higher Coulomb potential energy in a triply charged state, to be redistributed in internal energy and kinetic energy.

Figure 5.19a indeed shows a kinetic energy release of the triply charged states that is significantly higher than that of fragments from doubly charged clusters. Figure 5.19c shows the correlation of the average measured KER of the doubly and the triply charged clusters. The average KER is calculated at one recorded cluster size n, the sum of the number of molecules in all detected fragments. The dashed reference line is drawn at $\langle \text{KER}_{\text{triple}} \rangle = 3 \cdot \langle \text{KER}_{\text{double}} \rangle$, and the measured distribution follows that trend closely.

[5]The binomial coefficient $\binom{N_q}{2}$ is short for: $\frac{N_q!}{2!(N_q-2)!}$

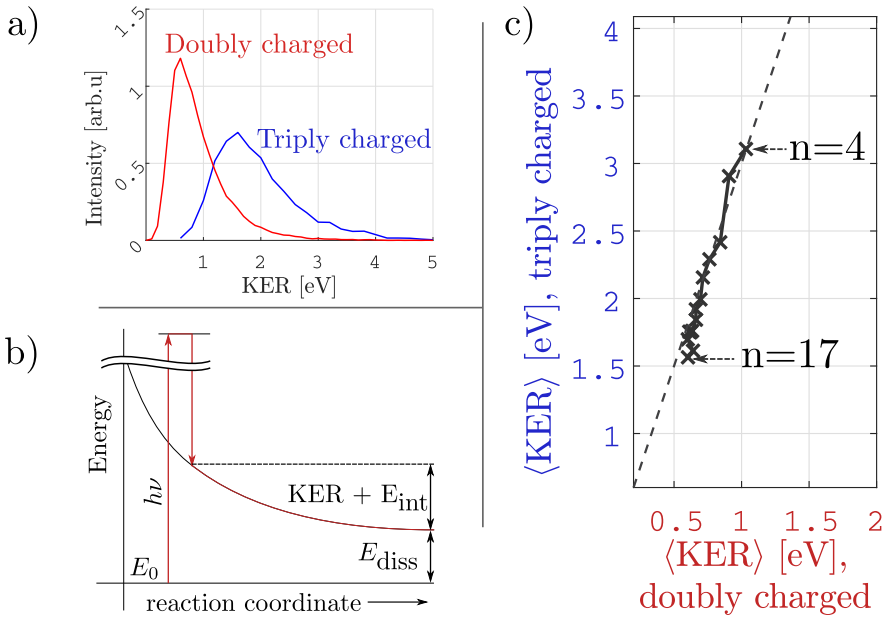

Figure 5.19: (a): The Kinetic Energy Release (KER) distribution of all doubly (red) and triply (blue) charged clusters. (b): A schematic energy diagram of ionization of the cluster, followed by dissociation. Part of the Coulomb explosion energy is transferred to KER, and part to internal degrees of freedom of the cluster (E_{int}). (c): the average KER of doubly and triply charged clusters, at the same recorded cluster sizes (from n=4 to 17). The dashed black reference line follows $\langle KER_{triple} \rangle = 3 \cdot \langle KER_{double} \rangle$. The momentum filter, as presented in Figure 5.18, is applied to all data shown.

The kinetic energy release thus seems to show a clear imprint of the number of charged fragments involved, despite the possibly different inter-fragment distances (r) in variously sized parent clusters. This might be a consequence of the long-range nature of Coulomb repulsion ($1/r$). Alternatively, the energy exchange and transfer to ro-vibrational degrees of freedom (i.e. a change in E_{int}) can be the underlying reason. Indeed, a recent study on the dissociation dynamics of water dimers shows that the energy exchange between the fragments diminishes above a certain distance ($r_{\text{crit exch}} \approx 11$Å) [38]. The correlation in Figure 5.19c implies an increasing $r_{\text{crit exch}}$ as the fragment size increases. It can be argued that the exchange of energy through Coulomb repulsion can sustain over a larger length scale when the involved energy levels are lower (i.e. a lower threshold to energy transfer). As the am-

monia fragment size increases, its lowest vibrational excitation energy indeed decreases [227]. This could possibly explain the (correlated) decrease in KER at increasing fragment size. However, the conclusive explanation for the clear correlation in kinetic energy release requires a systematic study, for instance by studying higher charge states and different molecular or atomic clusters.

Fission of mixed ammonia-water clusters

The cluster size distribution in Figure 5.15b shows a steep decrease in intensity as the cluster size increases from 5 to 6 molecular units. This can be an effect of the shell structure of ligands bound to the central ammonium (see Figure 2.7 in section 2.4), and thus suggest time for molecular rearrangement around the ammonium into the energetically favorable shell geometry.

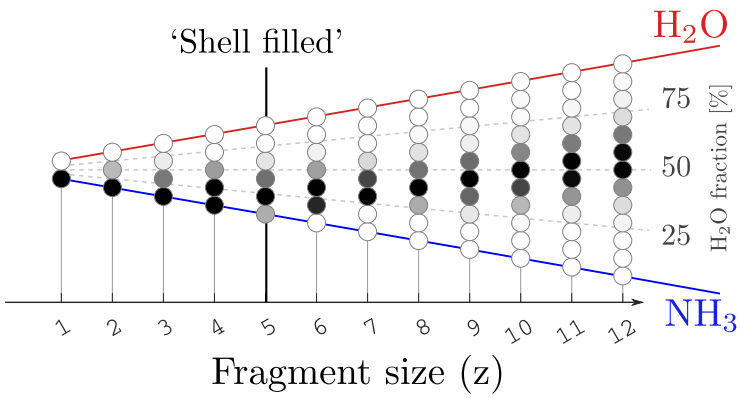

Figure 5.20: The water fraction of fragments from mixed ammonia-water clusters as a function of the fragment size. The intensity, expressed in gray scale filling of the circles, is normalized for each fragment size. Measurement taken at a photon energy of 450 eV, and an 18% water partial stagnation pressure.

Figure 5.20 shows the fragment cluster composition of mixed ammonia-water clusters. The fragment size is expressed in the total number of molecules in the fragment z ($(NH_3)_x(H_2O)_yH^+$, $z = x + y$), and the water fraction is defined as the percentage of water molecules, compared to the total number of molecules in the cluster. The majority of detected small fragments ($z \leq 5$) are almost exclusively composed of ammonia molecules, while at $z = 6$ there are no clusters detected *without* at least one water molecule, and the uptake of water increases with fragment size. The fragments that have not yet formed a filled *solvation shell* around the ammonium core (as shown in Figure 2.7) thus exclude water as a ligand, while water is found in larger fragments [89, 228].

This confirms that the typical fission time allows for structural rearrangement before dissociation and that the selection of ligands can be element-specific.

5.2.4 Stabilization

Above a critical cluster size, the Coulomb repulsion does not exceed the binding forces between molecules (discussed in section 2.4). Figure 5.15c shows stable doubly-charged ammonia clusters, appearing at a minimal size of 53 (reported 51 [110, 229]). In the case of water clusters, the hydrogen bonding is stronger, and the system can already host two charges in a cluster of only 35 molecules [230]. Mixing water and ammonia clusters results in the critical dication size in between the two pure appearance sizes, as observed in Figure 5.21. The water mixing into ammonia clusters stabilizes the doubly-charged cluster at a smaller size than expected from a linear dependency on the dication water fraction, illustrated by the dashed line.

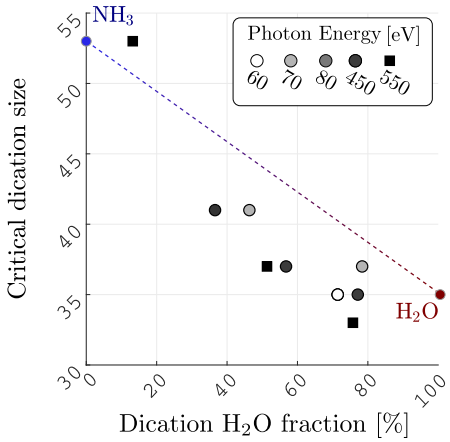

Figure 5.21: The critical dication size as a function of the water content of the dication in mixed ammonia-water clusters. Each marker represents an experiment at different conditions. The critical sizes of pure ammonia and water are indicated as a blue and red dot, respectively, and a linear interpolation between them is drawn as a dashed line.

The effective stabilization by water molecules suggests that the stronger water bonded molecules provide additional strength at a critical location. The ammonia molecules are most likely to collect in the vicinity of the charge host (see Figure 5.20), and an increased water concentration in the space between the charges can thus be expected. In collaboration with the University of Madrid, we are currently performing Molecular Dynamics (MD) simulations studying the geometry evolution upon ionization to provide more insight into the role of water in the dication stabilization. A more detailed study on charge and energy transfer in multi-ionized pure ammonia and ammonia-water clusters can be found in **Paper V** and **Paper VI**, respectively.

Chapter 6

Summary and Outlook

In this thesis, we have presented a twofold contribution to research in photoinduced processes in molecules and molecular clusters: by facilitating future research through the development of an electron-ion imaging spectrometer and data treatments methods, and through the investigation of charge and energy transfer processes in molecules and molecular clusters.

The designed imaging spectrometer is especially suitable for the coincident detection of electron and ion momenta, enabling the powerful coincidence data treatment techniques to uncover correlated ion or electron dependencies in terms of their energy, momentum or mass. The spectrometer allows experiments to be performed in different modes, in which the electron or ion momentum resolution is optimized.

The designed data treatment routines have shown their value in a multitude of experimental setups. The extensive use of data filters in **Papers I, V** and **VI**, has demonstrated its ability to uncover otherwise hidden correlations. Additionally, the momentum correlation has shown to provide an effective tool to obtain information on the *completeness* of the detection of a coincident set of ions.

The charge and energy flow in molecules has been studied in terms of their site- and state-selective dissociation. We have shown by the study of core ionization of ethyl trifluoroacetate (*ESCA*) that the chemical environment does not necessarily influence the site-dependent fragmentation in **Paper I**. We show that the molecule can fragment in multiple steps, and that the general site-dependence on dissociation is small. However, the limited memory of core ionization can be preserved up to a secondary breakup of the molecule.

We have studied the core excitation at different carbon sites in 1,3 *trans*

butadiene in **Paper II**. Correlated mass spectra show that nuclear dynamics before dissociation occurs in the majority of molecules, observed by the production of fragments that can not be produced from plain bond breaking of the neutral ground state molecule. The majority of core-excited butadiene molecules swiflty evaporate hydrogen(s). The increased evaporation from a terminal carbon, as the result of excitation at the terminal site, reduces the amount of centrally evaporated hydrogen, suggesting internal energy (and the loss of it by evaporative cooling) as the determining factor in hydrogen evaporation.

The photoionization induced charge distribution process has been studied in **Paper III**, studied through the investigation of sequential ionization of methyl iodide, both experimentally and theoretically. As the iodine charge state is increased through photoionization and Auger decay, the charge redistributes with the carbons and hydrogens in the methyl group. The carbon-hydrogen bond becomes weaker as more electrons transfer to iodine, causing the methyl group to atomize at higher carbon charge states. A classical model of the dissociation process is employed to provide additional insight in the charging mechanism and charge distribution. The model emphasizes the ionization rate at the onset of breakup to be the determining factor of the final charge state of the methyl group. Further photoionization of iodine at larger internuclear distances rarely results in charge transfer.

Cluster systems have been studied in the form of a single component dimer to a few tens of molecules, from valence single ionization to core ionization leading to multiply charged states. The study of small, singly charged clusters allows us to study the hydrogen and proton motion and their temperature and photon energy dependence in **Paper IV**. A cooler cluster is less likely to pass the energy barrier that requires hydrogen migration to transfer a proton.

The core ionization of ammonia and mixed ammonia-water clusters is investigated in **Paper V** and **VI**, respectively, in which several types of ionic fragment pairs are identified. One of those detected pairs are formed before the exothermic proton transfer has occurred. The fragment pair abundance, relative to the total production of fragments, does not show a strong dependency on the average cluster size and water content. Therefore, this fragment pair is expected to originate from the surface. The majority of the products appear in protonated fragment pairs. Through the use of advanced momentum filtering techniques, the fragment size-dependent kinetic energy release of the protonated fragments can be uncovered. The kinetic energy release of dissociation channels involving two and three charged particles are clearly correlated, and determining its cause in a conclusive manner needs further investigation. The

mixing of two molecular species (ammonia and water) into a cluster provides more insight into the dynamics of breakup, particularly the species-selective formation of charged fragments. Ammonium is recognized as the charge carrier, which forms a core surrounded preferentially by ammonia molecules. Water molecules are found in increasing numbers in fragments above the filling of the first ligand shell. The species-selective fragment formation evidences a complex multi-body inter molecular rearrangement before and during dissociation. The influence of the water-ammonia composition on the dication appearance size shows an effective stabilization by water molecules, at a higher rate than expected from a homogeneously mixed cluster. This suggests the stronger bonding water molecules to occupy a critical stabilization site in the cluster, possibly in a central position between the ammonium charge centers.

Future outlook We aim to extend the research on small-scale quantum systems to complex environments of higher societal or biological importance. In order to establish such a knowledge leap, orders of magnitude in time and length scale differences of the involved processes need to be taken into account. The technological and fundamental challenges are plenty, and below we give a short and probably incomplete list of recent technological and research advancements that might shape the near future of the research field.

The study of photoionization of free quantum systems is often performed in a high vacuum environment, reducing the disturbance by residual particles during the experiment. The supply of biologically relevant molecules into a vacuum environment is often challenging due to their fragility and low volatility. Moreover, a single isolated molecule might not accurately represent the embedded molecule. A film of water molecules around a biomolecule in a cluster can mimick the biological environment, and has recently been produced [231]. The ability to study these biomolecules in vacuum environments could allow the application of many spectroscopic techniques, such as photoelectron spectroscopy, absorption spectroscopy, time-dependent studies and momentum imaging of biomolecules.

In general, the size distribution of a cluster beam produced through adiabatic expansion is broad. The ability to select a neutral particle from a mixture of particles based on its size has recently been demonstrated [232]. The selection of a narrow size distribution from a cluster beam could not only enable us to get rid of the uncondensed part of the molecular beam (often forming the majority in the sample beam), but it would also allow us to answer many research questions, for instance by knowing the total size of neutral fragments produced in a dissociation.

Ammonia and sulfuric acid have been shown to be an important enhancer of water nucleation rates [233, 234], and the study of the trinary mixture (H_2O–NH_3–H_SO_4) upon co-expansion could provide information on the dissociation behavior upon multiply-charging.

Appendices

Appendix A

Detection efficiency

In a coincidence experiment, the quality of the measurement depends on detecting as many particles as possible, with the ultimate aim to be *complete* in the detection of (charged) particles that result from a single *parent* molecule or cluster. The probability to a complete detection increases when the detection efficiency is higher. Several factors can influence the detection efficiency:

- The active area ratio of the detector (the total channel area compared to the total detector area), also called the Open Area Ratio (OAR). In our case, this is around 60 %, but the latest MCPs (with funnelled channels) can reach up to 90% [183].
- The geometric transparency of the meshes the particle has to pass.
- The particle impact velocity; a lower impact velocity leads to a lower probability of detection [235, 236]. Note that a higher ion mass, for a given constant post-acceleration, leads to a lower impact velocity, implying a lower detection efficiency at higher masses.
- A detector is known to *age* through usage, and become less efficient [235], mainly due to a lower average number of electrons from secondary emission. The aging can be position-dependent, resulting in a position-dependent detection efficiency.
- The voltage thresholds that determine whether a peak becomes registered. This threshold can be set in the acquisition electronics, and is used to prevent the misinterpretation of noise as a signal from a genuine particle detection.

A lower detection efficiency increases the chances of registering aborted events (where one or more particles are not detected), and causes the *measured*

intensity ratios of different fragments (*branching ratios*) to be different from the real (physical) ratios. The real branching ratios can be reconstructed by assuming a constant detection efficiency [198], but at higher fragment masses (with lower impact velocity), the detection efficiency decreases and this assumption becomes less valid [235, 236]. We will present here a model that does include the mass dependency of the efficiency, followed by a method to calibrate the detector efficiencies.

The model Consider a general parent system (AB or ABC) as an example, see Figure A.1. We assume that the system can break up into all possible fragments (A, B, C or combinations thereof). Note that we assume these fragments to be charged. The fragment pairs are grouped in different *coincidence groups*, denoted Cn. Aborted events, where one or more particles remain undetected, cause an increase of the measured lower coincidence events, compared to the physical events.

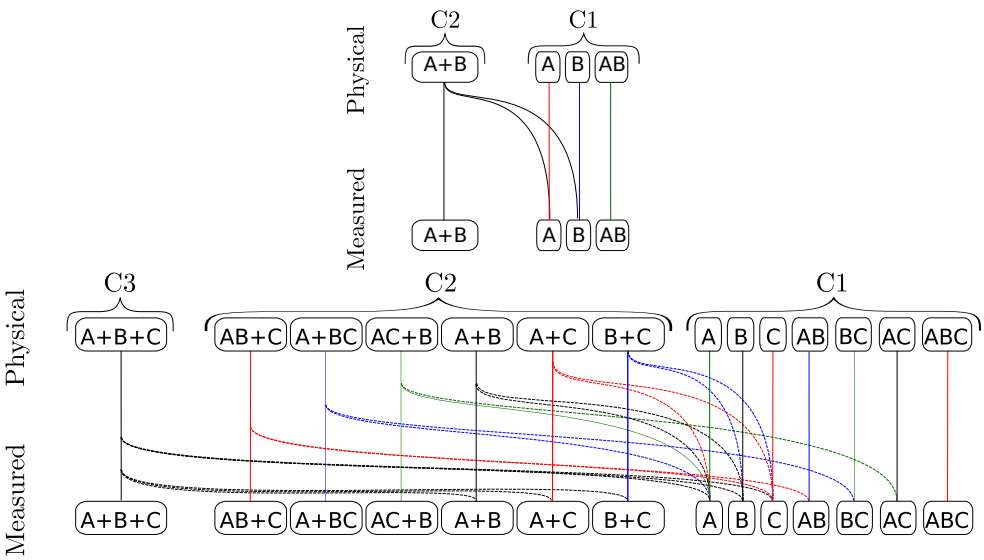

Figure A.1: A list of the possible physical (or real) fragment pairs created in an example system, AB (top) and ABC (bottom), and the possible fragment pairs being measured in complete or aborted events.

The *physical* (subscript p), or *real* probabilities for a certain fragment pair (say, A + B + C) ($P(A+B+C)_p$), and the *measured* probability ($P(A+B+C)_m$) relate to each other in the following way:

$$
\begin{aligned}
P(A+B)_m &= f_{e2}P(A+B)_p \cdot f_i(A) \cdot f_i(B) \qquad \text{(A.1)}\\
P(A)_m &= f_{e2}P(A+B)_p \cdot f_i(A) \cdot \overline{f_i(B)} + f_{e1}P(A)_p \cdot f_i(A)\\
P(B)_m &= f_{e2}P(A+B)_p \cdot \overline{f_i(A)} \cdot f_i(B) + f_{e1}P(B)_p \cdot f_i(B)\\
P(AB)_m &= f_{e1}P(AB)_p \cdot f_i(AB)
\end{aligned}
$$

The ABC parent system:

$$
\begin{aligned}
P(A+B+C)_m &= f_{e3}P(A+B+C)_p \cdot f_i(A) \cdot f_i(B) \cdot f_i(C) \qquad \text{(A.2)}\\
P(AB+C)_m &= f_{e2}P(AB+C)_p \cdot f_i(AB) \cdot f_i(C)\\
P(A+BC)_m &= f_{e2}P(A+BC)_p \cdot f_i(A) \cdot f_i(BC)\\
P(AC+B)_m &= f_{e2}P(AC+B)_p \cdot f_i(AC) \cdot f_i(B)\\
P(A+B)_m &= f_{e3}P(A+B+C)_p \cdot f_i(A) \cdot f_i(B) \cdot \overline{f_i(C)}\\
&\quad + f_{e2}P(A+B)_p \cdot f_i(A) \cdot f_i(B)\\
P(A+C)_m &= f_{e3}P(A+B+C)_p \cdot f_i(A) \cdot \overline{f_i(B)} \cdot f_i(C)\\
&\quad + f_{e2}P(A+C)_p \cdot f_i(A) \cdot f_i(C)\\
P(B+C)_m &= f_{e3}P(A+B+C)_p \cdot \overline{f_i(A)} \cdot f_i(B) \cdot f_i(C)\\
&\quad + f_{e2}P(B+C)_p \cdot f_i(B) \cdot f_i(C)\\
P(A)_m &= f_{e3}P(A+B+C)_p \cdot f_i(A) \cdot \overline{f_i(B)} \cdot \overline{f_i(C)}\\
&\quad + f_{e2}P(A+BC)_p \cdot f_i(A) \cdot \overline{f_i(BC)}\\
&\quad + f_{e2}P(A+B)_p \cdot f_i(A) \cdot \overline{f_i(B)}\\
&\quad + f_{e2}P(A+C)_p \cdot f_i(A) \cdot \overline{f_i(C)}\\
&\quad + f_{e1}P(A)_p \cdot f_i(A) \text{ (substitute B or C)}\\
P(AB)_m &= f_{e2}P(AB+C)_p \cdot f_i(AB) \cdot \overline{f_i(C)}\\
&\quad + f_{e1}P(AB)_p \cdot f_i(AB) \text{ (substitute BC or AC)}\\
P(ABC)_m &= f_{e1}P(ABC)_p \cdot f_i(ABC)
\end{aligned}
$$

where f denotes the detection efficiency (or *Quantum Efficiency*) of the ion (f_i) and electron (f_e) detector. The value (f_{e1}) represents the probability to detect one electron, if only one is created, and (f_{e2}) is the probability to detect one or more electron(s) if two are created. The line above a probability indicates the complement of that value ($\overline{p} = 1 - p$). The above equations give a quantitative picture to the diagrams shown above. In these equations, we assume that the (ion or electron) detection efficiency is a value that does not change during the experiment, or change for different hit positions on the detector.

Calibration We use different methods for the calibration of the electron and ion detector, and for the mass-dependency of the ion detection efficiency.

Electron detection efficiency The efficiency to detect one electron (f_{e_1}) or more electrons ($f_{e_{2,3,4}}$) can be determined from calibration measurements with argon. Using equations A.1 and A.2 above, and using data from a measurement of atomic argon photoionization at 27 eV, the single-electron detection efficiency of the electron detector is calculated to be around 60 percent. We assume a value of $f_{e_2} = 0.66$, calculated by assuming the ratio $\frac{1-f_{e_2}}{1-f_{e_1}}$ similar to reported earlier [198]. We assume similarly for 3 and 4 electrons: $f_{e_3} = 0.71$, $f_{e_4} = 0.75$.

Ion detection efficiency We look at measurements of free molecular CO as a means of calibration, since the branching ratios at several photon energies are well studied [237]. We choose the branching ratios at C 1s $\rightarrow \pi^*$, and use the ratio [198]:

$$f_i = \frac{f_{C^+,O^+,m}}{f_{CO^{2+},m}} \cdot \frac{f_{CO^{2+},p}}{f_{C^+,O^+,p}}$$

This leads to a detection efficiency $f_i \approx 0.28$ (28 percent).

Mass dependency Note that the above calculation determines the detection efficiency at one mass, while the mass dependency can be important for heavier ion detections, such as cluster ion fragments. To include the mass dependency, we make use of the distinct momentum correlation measured as a result of the fragmentation of a tri-atomic heteronuclear molecule. A clear footprint of an aborted coincidence can be found in the mutual angle between fragments. We look at the molecule OCS (carbonyl sulfide), which is comparable to the model ABC system presented previously. In the case of complete atomization of OCS, three different atomic ions are produced: O^+, C^+ and S^+.

Since the mutual angles between a physical double coincidence event (two atomic charged fragments produced, one neutral atom) are different from the mutual angle between physical triple coincidence spectra (three atomic charged fragments), their mutual angle histograms are distinct, and the portion of double coincidences that orginates from aborted triple coincidences is recognized. This can be seen in Figure A.2.

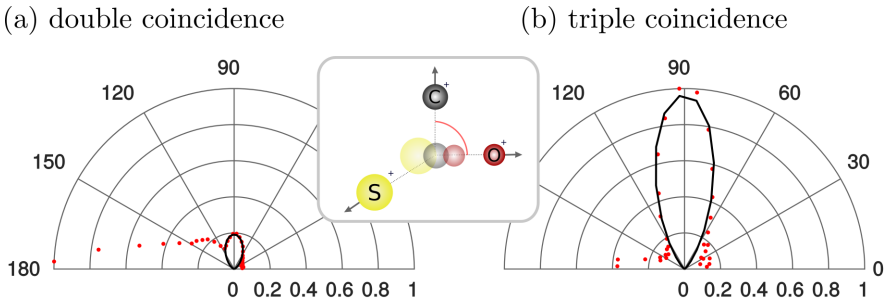

Figure A.2: The mutual angle histogram of the angle between the O^+ and C^+ fragment momenta (red dots). The angle in double coincidence events (a) contains aborted events from a physical triple event, shown in the triple hit events (b). Both histograms display a fit of the physical triple coincidence footprints (black line).

If the signal intensities are calculated by fitting, the calculation of the detection efficiencies is straightforward:

$$f_i(C) = \frac{I(A+B+C)_{C3,m}}{I(A+B+C)_{C2,m} + I(A+B+C)_{C3,m}} \tag{A.3}$$

where $I(A+B+C)_{C2,m}$ is the signal intensity of the aborted triple coincidence in the double coincidence (fitted peaks in Figure A.2, left), and $I(A+B+C)_{C3,m}$ is the signal intensity of the (true) triple coincidence signal.

This leads to the calculation of the detection efficiency at two different masses: at 32 [Da] it is 27 %, and at 16 [Da] it is about 32 %. These values can be used to fit a detection efficiency curve, as suggested in [235], to extrapolate these efficiencies to larger masses, as is done in Figure A.3.

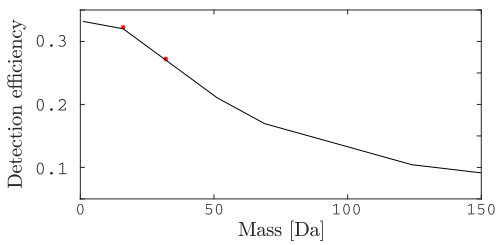

Figure A.3: The predicted mass-dependent detection efficiency curve from [235], adjusted to the calibration values obtained from the OCS calibration. Efficiency at zero mass = 0.33, Age factor: 3.5 (see [235] for definition of parameters and curve).

This only represents an estimate of the mass detection efficiency, and the reliable determination at higher masses requires the measurement of similar types of molecules or clusters at higher mass.

Appendix B

Momentum calibration

The conversion of the measured quantities from the detector (X, Y, T) to momentum space can be performed as suggested in Eq. 4.2 and 4.3. The x, y and z components of the converted momentum vector can be individually tuned by conversion parameters. The conversion parameters of importance in a electrostatic 3D momentum ion imaging spectrometer are the detection translational shift (along X and Y, 2 parameters), the mass-to-charge calibration values (2 parameters) and the molecular beam velocity vector (direction and amplitude, 4 parameters). This sums up to 8 parameters, and the following visualization method is intended to simplify the calibration procedure.

In Figure B.1, the momentum distribution of protons from ammonia molecules and clusters is imaged in a series of projections. Often, the momentum distribution is uniformly distributed in space, making histograms of $p_i - p_j$ momentum components a circularly-symmetric pattern (top row). Moreover, the absolute value of the momentum is not expected to vary considerably as the emission angle changes. Therefore, the momentum norm ($|\vec{p}|$) is expected to be invariant, leading to a straight, horizontal line in histograms of the p_i-component with $|\vec{p}|$ (bottom row).

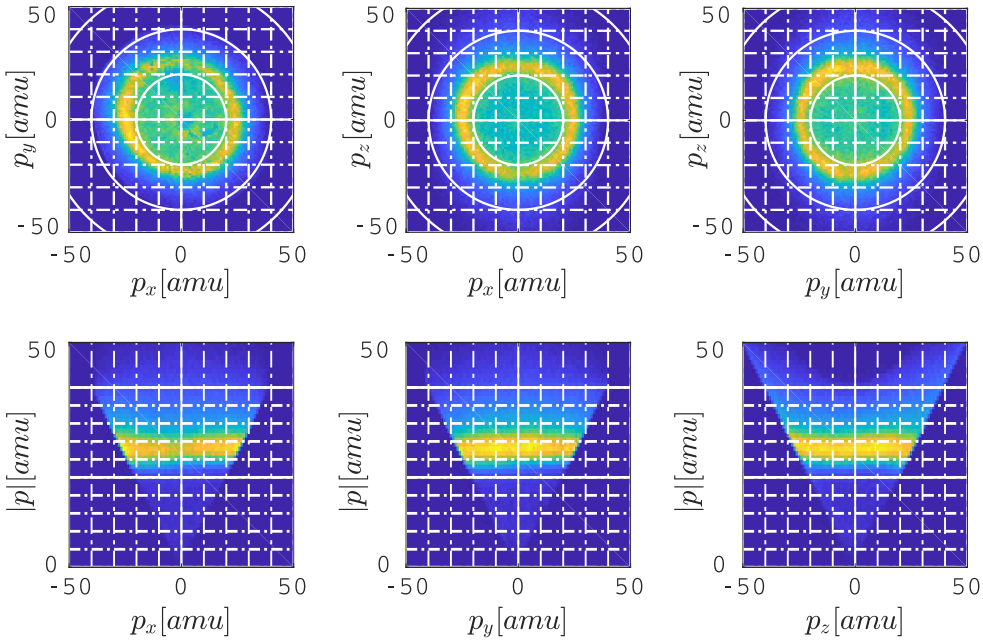

Figure B.1: Projections of the momentum distribution: the $\{p_x, p_y\}$ $\{p_x, p_z\}$ and $\{p_y, p_z\}$ components (top row), and the $p_{x,y,z}$ component versus the momentum norm ($|\vec{p}|$, bottom row). The data shows proton distributions from ammonia molecules and clusters from a molecular beam, from experiments at 360 and 420 eV photon energy, and 200 and 300 mbar nozzle pressure (merged).

Bibliography

[1] A. H. Zewail. Femtochemistry: Atomic-Scale Dynamics of the Chemical Bond. *J. Phys. Chem. A* **104**, 5660 (2000). https://doi.org/10.1021/jp001460h.

[2] P. A. Brühwiler, O. Karis & N. Mårtensson. Charge-transfer dynamics studied using resonant core spectroscopies. *Rev. Mod. Phys.* **74**, 703 (2002).

[3] A. H. Zewail. *Femtochemistry: Ultrafast Dynamics of the Chemical Bond*, vol. I and II (World Scientific: Singapore, 1994).

[4] S. L. Dexheimer. *Terahertz Spectroscopy: Principles and Applications* (CRC Press: Boca Raton, FL, 2007).

[5] J. D. Simon. *Ultrafast Dynamics of Chemical Systems*, vol. 7 (Springer Science & Business Media: New York, 2012).

[6] C. S. Ponseca, P. Chábera, J. Uhlig, P. Persson & V. Sundström. Ultrafast electron dynamics in solar energy conversion. *Chem. Rev.* **117**, 10940 (2017). https://doi.org/10.1021/acs.chemrev.6b00807.

[7] C. A. Schmuttenmaer. Exploring dynamics in the far-infrared with terahertz spectroscopy. *Chem. Rev.* **104**, 1759 (2004). https://doi.org/10.1021/cr020685g.

[8] M. D. Fayer. *Ultrafast Infrared Vibrational Spectroscopy* (CRC Press: New York, 2013).

[9] D. R. Dietze & R. A. Mathies. Femtosecond Stimulated Raman Spectroscopy. *ChemPhysChem* **17**, 1224 (2016). https://onlinelibrary.wiley.com/doi/pdf/10.1002/cphc.201600104.

[10] S. T. Cundiff & S. Mukamel. Optical multidimensional coherent spectroscopy. *Physics Today* (2013).

[11] P. C. Chen. An introduction to coherent multidimensional spectroscopy. *Applied Spectroscopy* **70**, 1937 (2016). https://doi.org/10.1177/0003702816669730.

[12] J. A. van Bokhoven & C. Lamberti. *X-Ray Absorption and X-Ray Emission Spectroscopy: Theory and Applications* (John Wiley & Sons, Ltd, 2016).

[13] S. Calvin. *XAFS for everyone* (CRC Press: Boca Raton, FL, 2013).

[14] C. Bressler & M. Chergui. Molecular Structural Dynamics Probed by Ultrafast X-Ray Absorption Spectroscopy. *Annu. Rev. Phys. Chem.* **61**, 263 (2010). https://doi.org/10.1146/annurev.physchem.012809.103353.

[15] W. Schuelke. *Electron Dynamics by Inelastic X-Ray Scattering* (Oxford Series on Synchrotron Radiation, 2007).

[16] T. Jahnke. Interatomic and intermolecular Coulombic decay: the coming of age story. *J. Phys. B: Atomic, Molecular and Optical Physics* **48**, 082001 (2015).

[17] NASA. The water cycle (2018). Available at https://pmm.nasa.gov/education/water-cycle.

[18] L. A. Alexander *et al. IPCC, Summary for Policymakers*, in *Climate Change 2013*. Tech. Rep., IPCC (2013).

[19] S. Eichkorn, S. Wilhelm, H. Aufmhoff, K. H. Wohlfrom & F. Arnold. Cosmic ray-induced aerosol-formation: First observational evidence from aircraft-based ion mass spectrometer measurements in the upper troposphere. *Geophysical Research Letters* **29**, 43–1–43–4 (2002). https://agupubs.onlinelibrary.wiley.com/doi/pdf/10.1029/2002GL015044.

[20] E. R. Lovejoy, J. Curtius & K. D. Froyd. Atmospheric ion induced nucleation of sulfuric acid and water. *Journal of Geophysical Research: Atmospheres* **109** (2004). https://agupubs.onlinelibrary.wiley.com/doi/pdf/10.1029/2003JD004460.

[21] J. Curtius, E. R. Lovejoy & K. D. Froyd. *Atmospheric Ion-Induced Aerosol Nucleation*, 159 (Springer New York, New York, NY, 2007).

[22] R. Wagner *et al.* The role of ions in new particle formation in the cloud chamber. *Atmospheric Chemistry and Physics* **17**, 15181 (2017).

[23] K. D. Kreuer, S. J. Paddison, E. Spohr & M. Schuster. Transport in proton conductors for fuel cell applications: Simulations, elementary reactions, and phenomenology. *Chem. Rev.* **104**, 4637 (2004).

[24] W. Kühlbrandt. Bacteriorhodopsin – the movie. *Nature* **406**, 569 (2000). http://dx.doi.org/10.1038/35020654.

[25] D. Oesterhelt & W. Stoeckenius. Rhodopsin-like protein from the purple membrane of halobacterium halobium. *Nature New Biology* **233**, 149 (1971). http://dx.doi.org/10.1038/newbio233149a0.

[26] C. Wickstrand, R. Dods, A. Royant & R. Neutze. Bacteriorhodopsin: Would the real structural intermediates please stand up? *Biochimica et Biophysica Acta (BBA) - General Subjects* **1850**, 536 (2015).

[27] W. Eberhardt *et al.* Site-Specific Fragmentation of Small Molecules Following Soft-X-Ray Excitation. *Phys. Rev. Lett.* **50**, 1038 (1983).

[28] W. Eberhardt, J. Stöhr, J. Feldhaus, E. W. Plummer & F. Sette. Correlation between Electron Emission and Fragmentation into Ions following Soft-X-Ray Excitation of the N_2 Molecule. *Phys. Rev. Lett.* **51**, 2370 (1983).

[29] L. S. Cederbaum, J. Zobeley & F. Tarantelli. Giant intermolecular decay and fragmentation of clusters. *Phys. Rev. Lett.* **79**, 4778 (1997).

[30] U. Hergenhahn. Interatomic and intermolecular coulombic decay: The early years. *J. Electron Spectrcop. Relat. Phenom.* **184**, 78 (2011).

[31] J. Zobeley, R. Santra & L. Cederbaum. Electronic decay in weakly bound heteroclusters: Energy transfer versus electron transfer. *J. Chem. Phys.* **115**, 5076 (2001). https://doi.org/10.1063/1.1395555.

[32] K. Sakai *et al.* Electron-Transfer-Mediated Decay and Interatomic Coulombic Decay from the Triply Ionized States in Argon Dimers. *Phys. Rev. Lett.* **106**, 033401 (2011).

[33] M. Förstel, M. Mucke, T. Arion, A. Bradshaw & U. Hergenhahn. Autoionization mediated by electron transfer. *Phys. Rev. Lett.* **106**, 033402 (2011).

[34] A. Furuhama, M. Dupuis & K. Hirao. Reactions associated with ionization in water: A direct ab initio dynamics study of ionization in

$(H_2O)_{17}$. *J. Chem. Phys.* **124**, 164310 (2006). https://doi.org/10.1063/1.2194904.

[35] H. Tachikawa & T. Takada. Proton transfer rates in ionized water clusters $(H_2O)_n$ (n = 2-4). *RSC Advances* **5**, 6945 (2015).

[36] P. Farmanara, W. Radloff, V. Stert, H. H. Ritze & I. V. Hertel. Real time observation of hydrogen transfer: Femtosecond time-resolved photoelectron spectroscopy in the excited ammonia dimer. *J. Chem. Phys.* **111**, 633 (1999). http://dx.doi.org/10.1063/1.479343.

[37] S. Tomoda. Ionization of the ammonia dimer: Proton transfer in the ionic state. *Chemical Physics* **110**, 431 (1986).

[38] O. Vendrell, S. Stoychev & L. Cederbaum. Generation of highly damaging H_2O^+ radicals by inner valence shell ionization of water. *ChemPhysChem* **11**, 1006 (2010).

[39] C. V. Raman & K. S. Krishnan. A new type of secondary radiation. *Nature* **121**, 501 (1928). http://dx.doi.org/10.1038/121501c0.

[40] J. W. Strutt. XXXVI. On the light from the sky, its polarization and colour. *The London, Edinburgh, and Dublin Philosophical Magazine and Journal of Science* **41**, 274 (1871). https://doi.org/10.1080/14786447108640479.

[41] H. Hertz. Über einen Einfluss des ultravioletten Lichtes auf die electrische Entladung. *Annalen der Physik* **267**, 983 (1887).

[42] A. Einstein. Über einen die Erzeugung und Verwandlung des Lichtes betreffenden heuristischen Gesichtspunkt. *Annalen der Physik* **17**, 132 (1905). Translated by D. ter Haar: On a Heuristic Point of View about the Creation and Conversion of Light. In *The Old Quantum Theory*, 91–107 (Pergamon Press, 1967).

[43] D. L. Walters & C. P. Bhalla. Nonrelativistic Auger Rates, X-Ray Rates, and Fluorescence Yields for the K Shell. *Phys. Rev. A* **3**, 1919 (1971).

[44] T. X. Carroll *et al.* Carbon 1s core-hole lifetime in CO_2. *Phys. Rev. A* **61**, 042503 (2000).

[45] L. Meitner. Über die Entstehung der β-Strahl-Spektren radioaktiver Substanzen. *Zeitschrift für Physik* **9**, 131 (1922).

[46] L. Inhester *et al.* Chemical understanding of the limited site-specificity in molecular inner-shell photofragmentation. *The Journal of Physical*

Chemistry Letters **9**, 1156 (2018). https://doi.org/10.1021/acs.jpclett.7b03235.

[47] C. Nicolas & C. Miron. Lifetime broadening of core-excited and -ionized states. *J. Electron Spectrcop. Relat. Phenom.* **185**, 267 (2012).

[48] M. G. Zahl, K. J. Børve & L. J. Sæthre. Carbon 1s photoelectron spectroscopy of the chlorinated methanes: Lifetimes and accurate vibrational lineshape models. *J. Electron Spectrcop. Relat. Phenom.* **185**, 226 (2012).

[49] T. Walsh, T. Meehan & F. Larkins. Prediction of molecular Auger rates using a statistical model. *J. Phys. B.: At., Mol. Opt. Phys.* **27**, 2211 (1994). http://stacks.iop.org/0953-4075/27/i=11/a=015.

[50] S. Zagorodskikh *et al.* Single-photon double and triple ionization of acetaldehyde (ethanal) studied by multi-electron coincidence spectroscopy. *Chemical Physics* **463**, 159 (2015).

[51] R. Beerwerth & S. Fritzsche. MCDF calculations of Auger cascade processes. *The European Physical Journal D* **71**, 253 (2017).

[52] T. A. Carlson & M. O. Krause. Electron Shake-Off Resulting from K-Shell Ionization in Neon Measured as a Function of Photoelectron Velocity. *Phys. Rev.* **140**, A1057 (1965).

[53] M. Born & R. Oppenheimer. Zur Quantentheorie der Molekeln. *Annalen der Physik* **389**, 457 (1927). https://onlinelibrary.wiley.com/doi/pdf/10.1002/andp.19273892002.

[54] B. H. Bransden & C. J. Joachain. *Physics of Atoms and Molecules* (Prentice Hall, 2002).

[55] M. J. Feinberg, K. Ruedenberg & E. L. Mehler. The origin of binding and antibinding in the hydrogen molecule-lon. vol. 5 of *Advances in Quantum Chemistry*, 27 (Academic Press, 1970).

[56] T. Osipov *et al.* Photoelectron-photoion momentum spectroscopy as a clock for chemical rearrangements: Isomerization of the dication of acetylene to the vinylidene configuration. *Phys. Rev. Lett.* **90**, 233002 (2003).

[57] P. Morin & C. Miron. Ultrafast dissociation: An unexpected tool for probing molecular dynamics. *J. Electron Spectrcop. Relat. Phenom.* **185**, 259 (2012).

[58] P. Morin & I. Nenner. Atomic Autoionization Following Very Fast Dissociation of Core-Excited HBr. *Phys. Rev. Lett.* **56**, 1913 (1986).

[59] I. Nenner *et al.* Photodissociation of core excited molecules. *J. Electron Spectrcop. Relat. Phenom.* **52**, 623 (1990).

[60] H. C. Schmelz, C. Reynaud, M. Simon & I. Nenner. Site-selective fragmentation in core-excited bromo-chloro-alkanes [$Br(CH_2)_nCl$]. *J. Chem. Phys.* **101**, 3742 (1994). https://doi.org/10.1063/1.467558.

[61] C. Miron, M. Simon, N. Leclercq, D. L. Hansen & P. Morin. Site-selective photochemistry of core excited molecules: Role of the internal energy. *Phys. Rev. Lett.* **81**, 4104 (1998).

[62] K. Müller-Dethlefs, M. Sander, L. A. Chewter & E. W. Schlag. Site-specific excitation in molecules at very high energies: changes in ionization patterns of 1,1,1-trifluoroethane (CF_3CH_3). *The Journal of Physical Chemistry* **88**, 6098 (1984). https://doi.org/10.1021/j150669a008.

[63] R. Thissen *et al.* Selectivity in the fragmentation of 1-bromo-2-iodoethane following iodine 4d core electron excitation. *Chem. Phys. Lett.* **199**, 102 (1992).

[64] E. Kukk *et al.* Internal energy dependence in X-ray-induced molecular fragmentation: An experimental and theoretical study of thiophene. *Phys. Rev. A* **91**, 043417 (2015).

[65] H. Levola *et al.* Ionization-site effects on the photofragmentation of chloro- and bromo-acetic acid molecules. *Phys. Rev. A* **92**, 063409 (2015).

[66] S. Zagorodskikh *et al.* Mechanisms of site-specific photochemistry following core-shell ionization of chemically inequivalent carbon atoms in acetaldehyde (ethanal). *J. Chem. Phys.* **145**, 124302 (2016). https://doi.org/10.1063/1.4962823.

[67] K. Kooser *et al.* Resonant Auger electron–photoion coincidence study of the fragmentation dynamics of an acrylonitrile molecule. *J. Phys. B.: At., Mol. Opt. Phys.* **43**, 235103 (2010). http://stacks.iop.org/0953-4075/43/i=23/a=235103.

[68] P. Bolognesi *et al.* Site- and state-selected photofragmentation of 2Br-pyrimidine. *Phys. Chem. Chem. Phys.* **17**, 24063 (2015).

[69] E. Kokkonen, T. Löytynoja, L. Hautala, K. Jänkälä & M. Huttula.

Fragmentation of mercury compounds under ultraviolet light irradiation. *J. Chem. Phys.* **143**, 074307 (2015). https://doi.org/10.1063/1.4928651.

[70] E. Itälä *et al.* Molecular fragmentation of pyrimidine derivatives following site-selective carbon core ionization. *J. Electron Spectrcop. Relat. Phenom.* **184**, 119 (2011).

[71] T. A. Carlson & R. M. White. Measurement of the Relative Abundances and Recoil Energy Spectra of Fragment Ions Produced as the Initial Consequences of X-Ray Interaction with CH_3I, HI, and DI. *J. Chem. Phys.* **44**, 4510 (1966). https://doi.org/10.1063/1.1726667.

[72] H. Le Rouzo. Double photoionization of molecular hydrogen: A theoretical study including the nuclear dissociation. *Phys. Rev. A* **37**, 1512 (1988).

[73] T. Weber *et al.* Complete photo-fragmentation of the deuterium molecule. *Nature* **431**, 437 (2004). http://dx.doi.org/10.1038/nature02839.

[74] P. R. Bunker. The effect of the breakdown of the Born-Oppenheimer approximation on the determination of B_e and ω_e for a diatomic molecule. *Journal of Molecular Spectroscopy* **35**, 306 (1970).

[75] Z. Zhang, W. Jiang, B. Wang & Z. Wang. Quantitative contribution of molecular orbitals to hydrogen bonding in a water dimer: Electron density projected integral (EDPI) analysis. *Chem. Phys. Lett.* **678**, 98 – 101 (2017).

[76] G. A. Jeffrey. *An Introduction to Hydrogen bonding* (Oxford Press, 1997).

[77] R. W. Shaw, J. S. Jen & T. D. Thomas. Auger spectrum of ammonia. *J. Electron Spectrcop. Relat. Phenom.* **11**, 91 (1977).

[78] D. Winkoun & G. Dujardin. Fragmentation of Doubly Charged Ammonia Cations NH_3^{++} Studied by the Photoion-Photoion Coincidence (PIPICO) Method. *Zeitschrift für Fysik D - Atoms, Molecules and Clusters* **4**, 57 (1986).

[79] N. V. Kryzhevoi & L. S. Cederbaum. Nonlocal Effects in the Core Ionization and Auger Spectra of Small Ammonia Clusters. *The Journal of Physical Chemistry B* **115**, 5441 (2011). http://dx.doi.org/10.1021/jp109920p.

[80] S. Marburger, O. Kugeler, U. Hergenhahn & T. Möller. Experimental Evidence for Interatomic Coulombic Decay in Ne Clusters. *Phys. Rev. Lett.* **90**, 203401 (2003).

[81] T. Jahnke *et al.* Experimental observation of interatomic coulombic decay in neon dimers. *Phys. Rev. Lett.* **93**, 163401 (2004).

[82] T. Jahnke *et al.* Ultrafast energy transfer between water molecules. *Nature Physics* **6**, 139 (2010).

[83] B. Brena *et al.* Ultrafast Molecular Dissociation of Water in Ice. *Phys. Rev. Lett.* **93**, 148302 (2004).

[84] O. Fuchs *et al.* Isotope and Temperature Effects in Liquid Water Probed by X-Ray Absorption and Resonant X-Ray Emission Spectroscopy. *Phys. Rev. Lett.* **100**, 027801 (2008).

[85] S. Thürmer *et al.* On the nature and origin of dicationic, charge-separated species formed in liquid water on X-ray irradiation. *Nature Chemistry* **5**, 590 (2013). `http://dx.doi.org/10.1038/nchem.1680`.

[86] P. Slavíček, B. Winter, L. S. Cederbaum & N. V. Kryzhevoi. Proton-transfer mediated enhancement of nonlocal electronic relaxation processes in X-ray irradiated liquid water. *J. Am. Chem. Soc.* **136**, 18170 (2014). `https://doi.org/10.1021/ja5117588`.

[87] G. Öhrwall *et al.* The electronic structure of free water clusters probed by Auger electron spectroscopy. *J. of Chem. Phys.* **123**, 054310 (2005). `http://dx.doi.org/10.1063/1.1989319`.

[88] H. Nakai *et al.* Theoretical study on ammonia cluster ions: nature of thermodynamic magic number. *Chemical Physics* **262**, 201 (2000).

[89] J. D. Payzant, A. J. Cunningham & P. Kebarle. Gas phase solvation of the ammonium ion by NH_3 and H_2O and stabilities of mixed clusters NH_4^+ $(NH_3)_n(H_2O)_w$. *Can. J. Chem.* **51**, 3242 (1973). `https://doi.org/10.1139/v73-485`.

[90] H. Shinohara, U. Nagashima & N. Nishi. Mass spectroscopic observation of an enhanced structural stability of water-ammonia binary clusters at n = 20 in the series $(H_2O)_n$ $(NH_3)_m H^+$ $(0 \leq n+m \leq 32)$. *Chem. Phys. Lett.* **111**, 511 (1984).

[91] W. R. Peifer, M. T. Coolbaugh & J. F. Garvey. Observation of 'magic numbers' in the population distributions of the $(NH_3)_{n-1}NH^{2+}$ and

$(NH_3)_nH^{2+}$ cluster ions: Implications for cluster ion structures. *J. Chem. Phys.* **91**, 6684 (1989).

[92] E. Wicke, M. Eigen & T. Ackermann. Über den Zustand des Protons (Hydroniumions) in wässriger Lösung. *Zeitschrift für physikalische Chemie* **1**, 340 (1954).

[93] M. Eigen. Protonenübertragung, Säure-Base-Katalyse und enzymatische Hydrolyse. Teil I: Elementarvorgänge. *Angewandte Chemie* **75**, 489 (1963). https://onlinelibrary.wiley.com/doi/pdf/10.1002/ange.19630751202.

[94] C. J. T. de Grotthuss. Sur la décomposition de l'eau et des corps q'uelle tient en dissolution à l'aide de l'électricité galvanique. *Annales de Chimie* **LVIII**, 54 (1806).

[95] D. Marx. Proton transfer 200 years after Von Grotthuss: Insights from ab initio simulations. *ChemPhysChem* **7**, 1848 (2006).

[96] G. Zundel & H. Metzger. Energiebänder der tunnelnden überschußprotonen in flüssigen säuren. Eine IR-spektroskopische untersuchung der natur der gruppierungen $H_5O_2^+$. *Zeitschrift für Physikalische Chemie* **58**, 225 (1968).

[97] S. Meiboom. Nuclear magnetic resonance study of the proton transfer in water. *J. Chem. Phys.* **34**, 375 (1961). http://dx.doi.org/10.1063/1.1700960.

[98] C. J. Montrose, J. A. Bucaro, J. Marshall-Coakley & T. A. Litovitz. Depolarized Rayleigh scattering and hydrogen bonding in liquid water. *J. Chem. Phys.* **60**, 5025 (1974). https://doi.org/10.1063/1.1681017.

[99] M. C. Bellissent-Funel & J. Teixeira. Dynamics of water studied by coherent and incoherent inelastic neutron scattering. *Journal of Molecular Structure* **250**, 213 (1991).

[100] Z. Cao, R. Kumar, Y. Peng & G. A. Voth. Proton transport under external applied voltage. *The Journal of Physical Chemistry B* **118**, 8090 (2014). http://dx.doi.org/10.1021/jp501130m.

[101] S. Wei, W. B. Tzeng & A. W. Castleman. Kinetic energy release measurements of ammonia cluster ions during metastable decomposition and determination of cluster ion binding energies. *J. Chem. Phys.* **92**, 332 (1990). http://dx.doi.org/10.1063/1.458434.

[102] L. Belau, K. R. Wilson, S. R. Leone & M. Ahmed. Vacuum ultraviolet

(VUV) photoionization of small water clusters. *J. Phys. Chem. A* **111**, 10075 (2007). http://dx.doi.org/10.1021/jp075263v.

[103] C. Bobbert, S. Schütte, C. Steinbach & U. Buck. Fragmentation and reliable size distributions of large ammonia and water clusters. *The European Physical Journal D* **19**, 183 (2002).

[104] C. Caleman & D. van der Spoel. Temperature and structural changes of water clusters in vacuum due to evaporation. *J. Chem. Phys.* **125**, 154508 (2006). https://doi.org/10.1063/1.2357591.

[105] T. D. Märk, P. Scheier, M. Lezius, G. Walder & A. Stamatovic. Multiply charged cluster ions of Ar, Kr, Xe, N_2, O_2, CO_2, SO_2 and NH_3: Production mechanism, appearance size and appearance energy. *Zeitschrift für Physik D Atoms, Molecules and Clusters* **12**, 279 (1989).

[106] F. R. S. Rayleigh. On the equilibrium of liquid conducting masses charged with electricity. *Philosophical Magazine Series 5* **14**, 184 (1882). http://dx.doi.org/10.1080/14786448208628425.

[107] I. Last, Y. Levy & J. Jortner. Beyond the Rayleigh instability limit for multicharged finite systems: From fission to Coulomb explosion. *Proceedings of the National Academy of Sciences of the United States of America* **99**, 9107 (2002).

[108] O. Echt *et al.* Dissociation channels of multiply charged van der waals clusters. *Phys. Rev. A* **38**, 3236 (1988).

[109] P. J. D. Lange, B. R. Veenstra & J. Kommandeur. Triply charged water clusters. *Chem. Phys. Lett.* **150**, 227 (1988).

[110] A. K. Shukla, C. Moore & A. J. Stace. Doubly charged ion clusters. *Chem. Phys. Lett.* **109**, 324 (1984).

[111] A. Zecca, G. P. Karwasz & R. S. Brusa. Total-cross-section measurements for electron scattering by NH_3, SiH_4, and H_2S in the intermediate-energy range. *Phys. Rev. A* **45**, 2777 (1992).

[112] A. Jain. Theoretical study of the total (elastic+inelastic) cross sections for electron -H_2O (NH_3) scattering at 10-3000 eV. *J. Phys. B.: At., Mol. Opt. Phys.* **21**, 905 (1988). http://stacks.iop.org/0953-4075/21/i=5/a=018.

[113] N. Schwentner, M. Skibowski & W. Steinmann. Photoemission from the valence bands of solid rare gases. *Phys. Rev. B* **8**, 2965 (1973).

[114] N. Schwentner *et al.* Photoemission from rare-gas solids: Electron energy distributions from the valence bands. *Phys. Rev. Lett.* **34**, 528–531 (1975).

[115] N. Schwentner. Mean-free path of electrons in rare-gas solids derived from vacuum-UV photoemission data. *Phys. Rev. B* **14**, 5490 (1976).

[116] N. Schwenter & E. E. Koch. Competition between electronic energy transfer and relaxation in Xe-doped Ar and Ne matrices studied by photoelectron spectroscopy. *Phys. Rev. B* **14**, 4687 (1976).

[117] J. Orloff (ed.) *Handbook of charged particle optics* (CRC Press, 1997).

[118] H. Liebl. *Applied Charged Particle Optics* (Springer-Verlag GmbH, 2007).

[119] W. C. Wiley & I. H. McLaren. Time-of-flight mass spectrometer with improved resolution. *Rev. Sci. Instrum.* **26**, 1150 (1955).

[120] A. T. J. B. Eppink & D. H. Parker. Velocity map imaging of ions and electrons using electrostatic lenses: Application in photoelectron and photofragment ion imaging of molecular oxygen. *Rev. Sci. Instrum.* **68**, 3477 (1997).

[121] F. Hadjarab & J. L. Erskine. Image properties of the hemispherical analyzer applied to multichannel energy detection. *J. Electron Spectrcop. Relat. Phenom.* **36**, 227 (1985).

[122] C. Miron, M. Simon, N. Leclercq, & P. Morin. New high luminosity "double toroidal" electron spectrometer. *Rev. Sci. Instrum.* **68**, 3728–3737 (1997).

[123] K. L. Guen *et al.* Development of a four-element conical electron lens dedicated to high resolution Auger electron–ion(s) coincidence experiments. *Rev. Sci. Instrum.* **73**, 3885 (2002). `http://dx.doi.org/10.1063/1.1511799`.

[124] D. Céolin, C. Miron, M. Simon, & P. Morin. Auger Electron–ion Coincidence Studies to probe Molecular Dynamics. *J. Electron Spectrosc. Relat. Phenom.* **141**, 171 (2004).

[125] A. Paulus *et al.* Novel time-of-flight electron spectrometer optimized for time-resolved soft-x-ray photoelectron spectroscopy. *Rev. Sci. Instrum.* **77**, 043105 (2006). `https://doi.org/10.1063/1.2194475`.

[126] G. Prümper & K. Ueda. Electron–ion–ion coincidence experiments for

photofragmentation of polyatomic molecules using pulsed electric fields: Treatment of random coincidences. *Nucl. Instr. Meth. Phys. Res., Sect. A* **574**, 350 (2007).

[127] M. Takahashi, J. P. Cave & J. H. D. Eland. Velocity imaging photoionization coincidence apparatus for the study of angular correlations between electrons and fragment ions. *Rev. Sci. Instrum.* **71**, 1337 (2000). https://doi.org/10.1063/1.1150460.

[128] G. A. Garcia, L. Nahon, C. J. Harding, E. A. Mikajlo & I. Powis. A refocusing modified velocity map imaging electron/ion spectrometer adapted to synchrotron radiation studies. *Rev. Sci. Instrum.* **76**, 053302 (2005).

[129] K. Hosaka *et al.* Coincidence velocity imaging apparatus for study of angular correlations between photoelectrons and photofragments. *Japanese Journal of Applied Physics* **45**, 1841 (2006). http://stacks.iop.org/1347-4065/45/i=3R/a=1841.

[130] D. Rolles *et al.* A velocity map imaging spectrometer for electron–ion and ion–ion coincidence experiments with synchrotron radiation. *Nucl. Instr. Meth. Phys. Res., Sect. B* **261**, 170 (2007).

[131] G. A. Garcia, H. Soldi-Lose & L. Nahon. A versatile electron-ion coincidence spectrometer for photoelectron momentum imaging and threshold spectroscopy on mass selected ions using synchrotron radiation. *Rev. Sci. Instrum.* **80**, 023102 (2009). https://doi.org/10.1063/1.3079331.

[132] C. S. Lehmann, N. B. Ram & M. H. M. Janssen. Velocity map photoelectron-photoion coincidence imaging on a single detector. *Rev. Sci. Instrum.* **83**, 093103 (2012). https://doi.org/10.1063/1.4749843.

[133] D. M. P. Holland & D. A. Shaw. The design and performance of a velocity map imaging spectrometer for the study of molecular photoionisation dynamics. *Chemical Physics* **409**, 11 (2012).

[134] G. A. Garcia, B. K. C. de Miranda, M. Tia, S. Daly & L. Nahon. Delicious iii: A multipurpose double imaging particle coincidence spectrometer for gas phase vacuum ultraviolet photodynamics studies. *Rev. Sci. Instrum.* **84**, 053112 (2013). https://doi.org/10.1063/1.4807751.

[135] M. D. Fraia *et al.* Photoionization and velocity map imaging spectroscopy of atoms, molecules and clusters with synchrotron and free

electron laser radiation at elettra. *Nucl. Instr. Meth. Phys. Res., Sect. B* **364**, 16 (2015).

[136] J. Ullrich *et al.* Recoil-ion and electron momentum spectroscopy: reaction-microscopes. *Rep. Prog. Phys.* **66**, 1463 (2003). `http://stacks.iop.org/0034-4885/66/i=9/a=203`.

[137] J. Laksman, D. Céolin, E. P. Månsson, S. L. Sorensen & M. Gisselbrecht. Development and characterization of a multiple-coincidence ion-momentum imaging spectrometer. *Rev. Sci. Instrum.* **84**, 123113 (2013).

[138] M. J. Riedl (ed.) *Optical design fundamentals for infrared Systems* (SPIE press, 2001), 2 edn.

[139] M. J. J. Vrakking. An iterative procedure for the inversion of two-dimensional ion/photoelectron imaging experiments. *Rev. Sci. Instrum.* **72**, 4084 (2001). `https://doi.org/10.1063/1.1406923`.

[140] R. Dörner *et al.* Fully Differential Cross Sections for Double Photoionization of He Measured by Recoil Ion Momentum Spectroscopy. *Phys. Rev. Lett.* **77**, 1024 (1996).

[141] H. Bräuning *et al.* Recoil ion and electronic angular asymmetry parameters for photo double ionization of helium at 99 ev. *J. Phys. B.: At., Mol. Opt. Phys.* **30**, L649 (1997). `http://stacks.iop.org/0953-4075/30/i=19/a=004`.

[142] A. Knapp *et al.* Energy sharing and asymmetry parameters for photo double ionization of helium 100 eV above threshold in single-particle and Jacobi coordinates. *J. Phys. B.: At., Mol. Opt. Phys.* **35**, L521 (2002). `http://stacks.iop.org/0953-4075/35/i=23/a=103`.

[143] R. Wehlitz, O. Hemmers, B. Langer, A. Menzel & U. Becker. Annual report. Tech. Rep., HASYLAB (1990).

[144] R. N. Zare. Photoejection dynamics. *Mol. Photochem.* **4**, 1 (1972). `http://www.stanford.edu/group/Zarelab/publinks/zarepub60.pdf`.

[145] S. Yang & R. Bersohn. Theory of the angular distribution of molecular photofragments. *J. Chem. Phys.* **61**, 4400 (1974).

[146] J. A. R. Samson. Simultaneous photoexcitation and photoionization of helium. *Phys. Rev. Lett.* **22**, 693 (1969).

[147] S. Skruszewicz *et al.* A new design for imaging of fast energetic electrons. *International Journal of Mass Spectrometry* **365-366**, 338 (2014).

[148] M. Gisselbrecht, A. Huetz, M. Lavollée, T. J. Reddish & D. P. Seccombe. Optimization of momentum imaging systems using electric and magnetic fields. *Rev. Sci. Instrum.* **76**, 013105 (2005). https://doi.org/10.1063/1.1832411.

[149] C. Stråhlman, T. Olsson, S. Leemann, R. Sankari & S. L. Sörensen. Preparing the MAX IV storage rings for timing-based experiments. In Q. Shen & C. Nelson (eds.) *AIP conference proceedings*, vol. 1741 (American Institute of Physics, 2016). http://dx.doi.org/10.1063/1.4952822.

[150] M. Lebech, J. C. Houver & D. Dowek. Ion–electron velocity vector correlations in dissociative photoionization of simple molecules using electrostatic lenses. *Rev. Sci. Instrum.* **73**, 1866 (2002). https://doi.org/10.1063/1.1458063.

[151] Y. Tang, Y.-I. Suzuki, T. Horio & T. Suzuki. Molecular frame image restoration and partial wave analysis of photoionization dynamics of no by time-energy mapping of photoelectron angular distribution. *Phys. Rev. Lett.* **104**, 073002 (2010).

[152] J. H. D. Eland, P. Linusson, M. Mucke & R. Feifel. Homonuclear site-specific photochemistry by an ion–electron multi-coincidence spectroscopy technique. *Chem. Phys. Lett.* **548**, 90 (2012).

[153] S. Nagaoka *et al.* Electron-ion-ion triple-coincidence spectroscopic study of site-specific fragmentation caused by Si : $2p$ core-level photoionization of $F_3SiCH_2CH_2Si(CH_3)_3$ vapor. *Phys. Rev. A* **75**, 020502 (2007).

[154] S. Nagaoka *et al.* A Study To Control Chemical Reactions Using Si:2p Core Ionization: Site-Specific Fragmentation. *The Journal of Physical Chemistry A* **115**, 8822 (2011). http://dx.doi.org/10.1021/jp203664r.

[155] V. Ayvazyan *et al.* First operation of a free-electron laser generating GW power radiation at 32 nm wavelength. *The European Physical Journal D - Atomic, Molecular, Optical and Plasma Physics* **37**, 297 (2006).

[156] Bartels, R. A. and Paul, A. and Green, H. and Kapteyn, H. C. and Murnane, M. M. and Backus, S. and Christov, I. P. and Liu, Y. and Attwood, D. and Jacobsen, C. Generation of Spatially Coherent Light

at Extreme Ultraviolet Wavelengths. *Science* **297**, 376 (2002). http://science.sciencemag.org/content/297/5580/376.full.pdf.

[157] W. Röntgen. Über eine neue Art von Strahlen. *Sitzungsberichten der Würzburger Physik.-medic. Gesellschaft Würzburg* 137 (1896).

[158] D. Iwanenko & I. Pomeranchuk. On the Maximal Energy Attainable in a Betatron. *Phys. Rev.* **65**, 343 (1944).

[159] V. L. Ginzburg & S. I. Syrovatskii. Cosmic Magnetobremsstrahlung (synchrotron Radiation). *Annual Reviews* **3**, 297 (1965).

[160] D. H. Tomboulian & P. L. Hartman. Spectral and Angular Distribution of Ultraviolet Radiation from the 300-MeV Cornell Synchrotron. *Phys. Rev.* **102**, 1423 (1956).

[161] S. Werin. *Accelerator techniques*, vol. 2 (MAX-lab, Lund, 2006).

[162] MAXIV. MAX IV synchrotron (2017). Available at https://www.maxiv.lu.se/.

[163] P. Willmott. *An Introduction to Synchrotron Radiation* (John Wiley and Sons Ltd, 2011).

[164] P. Schmüser, M. Dohlus & J. Rossbach. *Ultraviolet and Soft X-Ray Free-Electron Lasers: Introduction to Physical Principles, Experimental Results, Technological Challenges (Springer Tracts in Modern Physics)* (Springer, 2008).

[165] G. Margaritondo & P. Rebernik Ribic. A simplified description of X-ray free-electron lasers. *Journal of Synchrotron Radiation* **18**, 101 (2011).

[166] I. Robinson, G. Gruebel & S. Mochrie. Focus on X-ray Beams with High Coherence. *New Journal of Physics* **12**, 035002 (2010). http://stacks.iop.org/1367-2630/12/i=3/a=035002.

[167] Soleil (2017). Available at https://www.synchrotron-soleil.fr/.

[168] PLEIADES. Pleiades beamline (2017). Available at https://www.synchrotron-soleil.fr/fr/lignes-de-lumiere/pleiades.

[169] F. Desy (2017). http://flash.desy.de/. Available at http://flash.desy.de/.

[170] M. Bässler *et al.* Soft X-ray undulator beam line I411 at MAX-II for gases, liquids and solid samples. *J. Electron Spectrcop. Relat. Phenom.* **101**, 953 (1999).

[171] G. Scoles. *Atomic and Molecular Beam Methods, Chapter 4 (H. Pauly)* (Oxford University Press, Oxford, UK, 1989-1992).

[172] D. R. Miller. *"Free Jet Sources" in Atomic and Molecular Beam Methods* (Oxford University Press, Oxford/New- York, (1988), 1988).

[173] G. Sanna & G. Tomassetti. *Introduction to Molecular Beams Gas Dynamics* (Imperial college press, 2015).

[174] H. Ashkenas & C. K. Sherman. The structure and utilization of supersonic free jets in low density wind tunnels,. *Rarefied gas Dynamics, Fourth International symposium supplement 3* **3**, 84 (1966).

[175] S. K. Karthick, J. Gopalan & K. P. J. Reddy. Visualization of Supersonic Free and Confined Jet using Planar Laser Mie Scattering Technique. *Journal of the Indian Institute of Science* **96**, 29 (2016).

[176] E. W. Becker, K. Bier & W. Henkes. Strahlen aus kondensierten Atomen und Molekeln im Hochvakuum. *Zeitschrift für Physik* **146**, 333 (1956).

[177] D. L. Bunker. Mechanics of Atomic Recombination Reactions. *J. Chem. Phys.* **32**, 1001 (1960). `http://dx.doi.org/10.1063/1.1730840`.

[178] R. Karnbach, M. Joppien, J. Stapelfeldt, J. Wörmer & T. Möller. CLULU: An experimental setup for luminescence measurements on van der Waals clusters with synchrotron radiation. *Rev. Sci. Instrum.* **64**, 2838 (1993).

[179] U. Buck & R. Krohne. Cluster size determination from diffractive He atom scattering. *J. Chem. Phys.* **105**, 5408 (1996). `https://doi.org/10.1063/1.472406`.

[180] S. De Dea, D. R. Miller & R. E. Continetti. Cluster and Solute Velocity Distributions in Free-Jet Expansions of Supercritical CO_2. *The Journal of Physical Chemistry A* **113**, 388 (2009). `http://dx.doi.org/10.1021/jp805618z`.

[181] C. W. S. Conover, Y. J. Twu, Y. A. Yang & L. A. Bloomfield. A time of flight mass spectrometer for large molecular clusters produced in supersonic expansions. *Rev. Sci. Instrum.* **60**, 1065 (1989). `http://dx.doi.org/10.1063/1.1140318`.

[182] J. L. Wiza. Microchannel plate detectors. *Nuclear Instruments and Methods* **162**, 587 (1979).

[183] Hamamatsu Photonics K.K. Manuals (2016). https://www.hamamatsu.com/resources/pdf/etd/MCP_TMCP0002E.pdf.

[184] S. E. Sobottka & M. B. Williams. Delay line readout of microchannel plates. *IEEE Transactions on Nuclear Science* **35**, 348 (1988).

[185] O. Jagutzki *et al.* A broad-application microchannel-plate detector system for advanced particle or photon detection tasks: large area imaging, precise multi-hit timing information and high detection rate. *Nucl. Instr. Meth. Phys. Res., Sect. A* **477**, 244 (2002).

[186] Roentdek. Delay line detectors (2018). Available at roentdek.com/detectors/.

[187] Surface concept. Delay line detectors (2018). Available at surface-concept.com/products_dld.html.

[188] Roentdek. Hexagonal delay line detectors (2018). Available at roentdek.de/info/Delay_Line/.

[189] Surface concept. Four-quadrant delay line detectors (2018). Available at surface-concept.com/downloads/info/DLD-4Q.pdf.

[190] J. Laksman. *Nuclear motion in molecular ions studied with synchrotron raidation and multicoincidence momentum imaging spectrometry.* Ph.D. thesis, Lund University (2012).

[191] D. A. Dahl. *Simion 3D version 7.0 User's manual* (2000).

[192] B. Oostenrijk & B. Bolling (2017). https://github.com/gasfas/ANACONDA_2. Available at https://github.com/gasfas/ANACONDA_2.

[193] X. J. Liu, C. Nicolas, E. Robert & C. Miron. EPICEA: Probing High-Energy Electron Emission In The Molecular Frame. *Journal of Physics: Conference Series* **488**, 142005 (2014). http://stacks.iop.org/1742-6596/488/i=14/a=142005.

[194] T. Arion & U. Hergenhahn. Coincidence spectroscopy: Past, present and perspectives. *J. Electron Spectrcop. Relat. Phenom.* **200**, 222 (2015).

[195] L. J. Frasinski, K. Codling & P. A. Hatherly. Covariance mapping: A correlation method applied to multiphoton multiple ionization. *Science* **246**, 1029 (1989). http://science.sciencemag.org/content/246/4933/1029.full.pdf.

[196] L. J. Frasinski. Covariance mapping techniques. *J. Phys. B.: At., Mol.*

Opt. Phys. **49**, 152004 (2016). http://stacks.iop.org/0953-4075/49/i=15/a=152004.

[197] O. Kornilov *et al.* Coulomb explosion of diatomic molecules in intense XUV fields mapped by partial covariance. *J. Phys. B.: At., Mol. Opt. Phys.* **46**, 164028 (2013). http://stacks.iop.org/0953-4075/46/i=16/a=164028.

[198] M. Simon, T. LeBrun, P. Morin, M. Lavollee & J. L. Marechal. A photoelectron-ion multiple coincidence technique applied to core ionization of molecules. *Nuclear Instruments and Methods in Physics Research* **62**, 167 (1991).

[199] J. Zhu & W. T. Hill. Momentum and correlation spectra following intense-field dissociative ionization of h2. *J. Opt. Soc. Am. B* **14**, 2212 (1997).

[200] M. E. D. Lestard *et al.* Experimental and theoretical structure and vibrational analysis of ethyl trifluoroacetate, $CF_3CO_2CH_2CH_3$. *J. Raman Spectrosc.* **41**, 1357 (2010).

[201] K. Siegbahn. Electron spectroscopy for atoms, molecules, and condensed matter. *Rev. Mod. Phys.* **54**, 709 (1982).

[202] O. Travnikova *et al.* The ESCA Molecule—Historical Remarks and New Results. *J. Electron Spectrosc. Relat. Phenom.* **185**, 191 (2012).

[203] R. H. Dalitz. Decay of τ mesons of known charge. *Phys. Rev.* **94**, 1046 (1954).

[204] A. Alnaser *et al.* Momentum-imaging investigations of the dissociation of D_2^+ and the isomerization of acetylene to vinylidene by intense short laser pulses. *J. Phys. B.: At., Mol. Opt. Phys.* **39**, S485 (2006). http://stacks.iop.org/0953-4075/39/i=13/a=S21.

[205] S. Oghbaiee *et al.* Site-selective dissociation upon core-electronic excitation in butadiene. In manuscript.

[206] M. P. de Miranda *et al.* Fine vibrational structure in core-to-bound spectra of polyatomic molecules. *J. Chem. Phys.* **101**, 5500 (1994). https://doi.org/10.1063/1.467339.

[207] S. Oghbaie *et al.* Dissociative double-photoionization of butadiene in the 25-45 eV energy range using 3-D multi-coincidence ion momentum imaging spectrometry. *J. Chem. Phys.* **143**, 114309 (2015). https://doi.org/10.1063/1.4931104.

[208] H. Kjeldsen *et al.* Absolute photoionization cross sections of I+ and I 2+ in the 4 d ionization region. *Phys. Rev. A* **62**, 020702 (2000).

[209] J. J. Yeh & I. Lindau. Atomic subshell photoionization cross sections and asymmetry parameters: $1 \leq Z \leq 103$. *Atomic data and nuclear data tables* **32**, 1 (1985).

[210] J. L. Duncan & P. D. Mallinson. The infrared spectrum of CHD_2I and the ground state geometry of methyl iodide. *Journal of Molecular Spectroscopy* **39**, 471 (1971).

[211] G. Dujardin, L. Hellner, D. Winkoun & M. Besnard. Valence and inner shell electronic processes in dissociative double photoionization of CH_3I. *Chemical Physics* **105**, 291 – 299 (1986).

[212] A. T. Domondon & X. M. Tong. Photoabsorption spectra of I and its ions in the 4 d region. *Phys. Rev. A* **65**, 032718 (2002).

[213] J. M. Bizau *et al.* Absolute photoionization cross sections along the Xe isonuclear sequence: Xe^{3+} to Xe^{6+}. *Phys. Rev. A* **73**, 022718 (2006).

[214] N. Watanabe *et al.* Photoion-yield spectra of Xe^{2+} in the 4d-threshold energy region. *Journal of Physics B: Atomic, Molecular and Optical Physics* **31**, 4137 (1998). `http://stacks.iop.org/0953-4075/31/i=18/a=011`.

[215] J. N. Cutler, G. M. Bancroft & K. H. Tan. Ligand-field splittings and core-level linewidths in I 4 d photoelectron spectra of iodine molecules. *J. Chem. Phys.* **97**, 7932 (1992).

[216] A. Niehaus. A classical model for multiple-electron capture in slow collisions of highly charged ions with atoms. *Journal of Physics B: Atomic and Molecular Physics* **19**, 2925 (1986).

[217] K. Schnorr. *XUV Pump-Probe Experiments on Diatomic Molecules: Tracing the Dynamics of Electron Rearrangement and Interatomic Coulombic Decay.* Ph.D. thesis, University of Heidelberg, Germany (2014).

[218] M. Berholts *et al.* Photofragmentation of gas-phase acetic acid and acetamide clusters in the vacuum ultraviolet region. *J. Chem. Phys.* **147**, 194302 (2017). `https://doi.org/10.1063/1.4999686`.

[219] L. Åsbrink, A. Svensson, W. Niessen & G. Bieri. 30.4-nm He(II) photoelectron spectra of organic molecules: Part V. Hetero-compounds con-

taining first-row elements (C, H, B, N, O, F). *J. Electron Spectrcop. Relat. Phenom.* **24**, 293 (1981).

[220] J. C. Traeger, R. G. McLoughlin & A. J. C. Nicholson. Heat of formation for acetyl cation in the gas phase. *J. Am. Chem. Soc.* **104**, 5318 (1982). https://doi.org/10.1021/ja00384a010.

[221] S. T. Ceyer, P. W. Tiedemann, C. Y. Ng, B. H. Mahan & Y. T. Lee. Energetics of gas phase proton solvation by NH_3. *J. Chem. Phys.* **70**, 14 (1979). http://aip.scitation.org/doi/pdf/10.1063/1.437233.

[222] O. Echt, P. D. Dao, S. Morgan & A. W. Castleman. Multiphoton ionization of ammonia clusters and the dissociation dynamics of protonated cluster ions. *J. Chem. Phys.* **82**, 4076 (1985). http://dx.doi.org/10.1063/1.448849.

[223] S. Tomoda & K. Kimura. Proton-transfer potential-energy surfaces of the water dimer cation $(H_2O)_2{}^+$ in the 12A" and 12A' states. *Chemical Physics* **82**, 215 (1983).

[224] D. Barreiro Lage & S. Diaz-Tendero. Neutral ammonia-water cluster geometries, private communication (2018).

[225] P. Hvelplund *et al.* Stability and structure of protonated clusters of ammonia and water, $H^+(NH_3)_m\ (H_2O)_n$. *The Journal of Physical Chemistry A* **114**, 7301 (2010). http://dx.doi.org/10.1021/jp104162k.

[226] H. P. Cheng. The motion of protons in water–ammonia clusters. *J. Chem. Phys.* **105**, 6844 (1996). https://doi.org/10.1063/1.471979.

[227] G. Santambrogio. *Infrared Spectroscopy of Gas Phase Cluster Ions.* Ph.D. thesis, Freien Universität Berlin (2007).

[228] A. M. Hogg & P. Kebarle. Mass-Spectrometric Study of Ions at Near-Atmospheric Pressure. II. Ammonium Ions Produced by the Alpha Radiolysis of Ammonia and Their Solvation in the Gas Phase by Ammonia and Water Molecules. *J. Chem. Phys.* **43**, 449 (1965).

[229] M. T. Coolbaugh, W. R. Peifer & J. F. Garvey. Ion-molecule chemistry within doubly charged ammonia clusters. *Chem. Phys. Lett.* **156**, 19 (1989).

[230] A. J. Stace. Evidence of two stable forms of doubly and triply charged water cluster. *Phys. Rev. Lett.* **61**, 306 (1988).

[231] P. Geyer *et al.* Perspectives for quantum interference with biomolecules

and biomolecular clusters. *Physica Scripta* **91**, 063007 (2016). http://stacks.iop.org/1402-4896/91/i=6/a=063007.

[232] Y. P. Chang, D. Horke, S. Trippel & J. Küpper. Spatially-controlled complex molecules and their applications. *International Reviews in Physical Chemistry* **34**, 557 (2015). https://doi.org/10.1080/0144235X.2015.1077838.

[233] S. M. Ball, D. R. Hanson, F. L. Eisele & P. H. McMurry. Laboratory studies of particle nucleation: Initial results for H_2SO_4, H_2O, and NH_3 vapors. *Journal of Geophysical Research: Atmospheres* **104**, 23709. https://agupubs.onlinelibrary.wiley.com/doi/pdf/10.1029/1999JD900411.

[234] T. Kurtén *et al.* Investigating the role of ammonia in atmospheric nucleation. In *Nucleation and Atmospheric Aerosols*, 52 (Springer Netherlands, Dordrecht, 2007).

[235] I. S. Gilmore & M. P. Seah. Ion detection efficiency in sims: dependencies on energy, mass and composition for microchannel plates used in mass spectrometry. *International Journal of Mass Spectrometry* **202**, 217 (2000).

[236] G. W. Fraser. The ion detection efficiency of microchannel plates (MCPs). *International Journal of Mass Spectrometry* **215**, 13 (2002).

[237] A. P. Hitchcock *et al.* Ionic fragmentation of K-shell excited and ionized CO. *Phys. Rev. A* **37**, 2448 (1988).